Probing the QCD Critical Point by higher moments of the net-charge distribution at RHIC energies

By

Nihar Ranjan Sahoo

Enrollment No. PHYS04200904002

Variable Energy Cyclotron Centre, Kolkata

A thesis submitted to

The Board of Studies in Physical Sciences

In partial fulfillment of requirements for the Degree of

DOCTOR OF PHILOSOPHY

of

HOMI BHABHA NATIONAL INSTITUTE

December 2013

Homi Bhabha National Institute

Recommendation of the Viva Voce Board

As members of the Viva Voce Board, we certify that we have read the dissertation prepared by **Nihar Ranjan Sahoo** entitled **Probing the QCD Critical Point by higher moments of the net-charge distribution at RHIC energies** and recommend that it may be accepted as fulfilling the dissertation requirement for the degree of Doctor of Philosophy.

.....**Date:**

Chairman- Prof. S. Bhattacharya

.....**Date:**

Convener- Prof. T. K. Nayak

.....**Date:**

Member 1- Prof. J. Alam

.....**Date:**

Member 2- Prof. S. Chattopadhyay

.....**Date:**

Member 3 (External Examiner)- Prof. Raghava Varma

Finally approval and acceptance of this dissertation is contingent upon the candidate's submission of the final copies of the dissertation to HBNI.

I hereby certify that I have read this dissertation prepared under my direction and recommend that it may be accepted as fulfilling the dissertation requirement.

Date:

Place:

STATEMENT BY AUTHOR

This dissertation has been submitted in partial fulfillment of requirements for an advanced degree at Homi Bhabha National Institute (HBNI) and is deposited in the Library to be made available to borrowers under rules of the HBNI.

Brief quotations from this dissertation are allowable without special permission, provided that accurate acknowledgement of source is made. Requests for permission for extended quotation from or reproduction of this manuscript in whole or in part may be granted by the Competent Authority of HBNI when in his or her judgment the proposed use of the material is in the interests of scholarship. In all other instances, however, permission must be obtained from the author.

Signature

Nihar Ranjan Sahoo

DECLARATION

I, hereby declare that the investigation presented in the thesis has been carried out by me. The work is original and has not been submitted earlier as a whole or in part for a degree/diploma at this or any other Institution/University.

Signature

Nihar Ranjan Sahoo

Dedicated to my *parents*

ACKNOWLEDGEMENTS

I would like to thank my supervisor, Prof. Tapan K. Nayak, for his constant guidance, support, inspiration, supervision and encouragement for accomplishing my thesis. It is my privilege to work with you, Sir, for four years.

I would also like to thank Prof. Subhasish Chattopadhyay for his advice, discussion, and support for my understanding on experimental higher energy physics, data analysis and detector systems. I would like to thank Prof. Bedangdas Mohanty for his advice, and discussion for my understanding on experimental higher energy physics and data analysis. I would thank Prof. Dinesh K. Shrivastava for his constant support and encouragements during my stay at VECC. I thank Prof. Jan-e Alam and Prof. Sourav Sarkar for their support and useful discussion. I would like to thank Prithwish Tribedy for discussion on various part of physics, his support on analysis and plenty of discussion on physics. It is really a very nice experience working and spending time at VECC and discussing wide area of physics. My especially thank to Prof. Frithjof Karsch, Prof. Krzysztof Redlich, Prof. Nu Xu and Dr. Swagota Mukherjee for useful discussion with them during my BNL visit. I would thank Prof. Sourendu Gupta for helpful discussion. Thank you Dr. Xiaofeng Luo, Dr. Lizhu Chen, Dr. Hiroshi Masui, Prof. W.J. Llope and Dr. Daniel McDonald for your support and discussion during data analysis.

I would like to thank VECC grid peer for providing me enormous support for huge computational work. Thanks to STAR Collaboration and bulk correlation group for providing very good scientific environment for analyzing the data and understanding the advanced physics in heavy ion collision.

I also take this opportunity to thank my colleagues, Sudipan De and Somnath

De with whom i have enjoyed working together and spent lots of funny moments over the years. I would like to thanks also Md. Younus, Arnab, and Manish for spending friendly time during Ph.D years. My special thanks to my seniors, Dr. Sidharth Prashad, Dr. Mriganka Mondol, Dr. Santosh K Das, Dr. Payal Mohanty, Dr. Sabyasachi Ghosh, Dr. Victor Roy and Dr. Haridas Pai with whom i have discussed and enjoyed over the years. I would like to thank my juniors, numerous names to list, for their cooperation and friendly discussion. I received help and support, at VECC, from administrative to scientific level during my stay, thank you all very much.

Finally, I express my deep gratitude to my parents, my younger brother and sisters for supporting me in all respects, without complaining anything. I am grateful to you. Thank you very very much for standing aside as my strength. Especially, I thank my wife, Bhanu sharma. Her continuous and unwavering support, and encouragement helped me a lot in the completion of the thesis.

Nihar Ranjan Sahoo

SYNOPSIS

According to the theory of Quantum Chromodynamics, the interaction between its fundamental constituents, quarks and gluons, can lead to the different state of matter under extreme conditions of high baryon density and/or high temperature. This new form of strongly interacting matter is known as Quark-Gluon-Plasma (QGP). At very high temperature and low baryon chemical potential, the transition between normal to QCD matter is believed to be a smooth crossover, whereas at high baryon density it is expected to be a first order phase transition. The QCD Critical Point is located at the junction of the first order transition and crossover. The Critical Point thus occupies a significant location in the QCD phase diagram. The Relativistic Heavy Ion Collider (RHIC) has undertaken its Beam Energy Scan program to search for the Critical Point as well as to study the hadronic to QCD phase transition in more detail. With the variation of the beam energy, both temperature and baryon chemical potential can be simultaneously controlled, and hence the major part of the QCD phase diagram can be accessed experimentally. The STAR experiment, at RHIC has collected a large amount of data for Au+Au collisions at center of mass energies from 7.7 GeV to 200 GeV, which correspond to baryon chemical potentials from 450 MeV to 20 MeV, respectively.

One of the most plausible signatures of the critical point has been predicted to be the large event-by-event fluctuations of thermodynamic quantities measured in high-energy heavy-ion collisions. This is because of the fact that the thermodynamic susceptibilities and the correlation lengths of the produced systems diverge at the critical point. Various QCD inspired models and lattice calculations predict

that higher moments of conserved quantities, such as distributions of net-charge, net-baryon and the net-strangeness are associated with the higher order thermodynamic susceptibilities and exhibit strong dependence on the correlation strength. This makes the moments, such as, mean (M), standard deviation (σ), skewness (S), and kurtosis (κ), etc., of the conserved quantities and their products to be sensitive probes in the location of the critical point. These moments are related to the correlation length. The higher order moments are related to higher power of the correlation length and hence the signal of the critical point can be amplified by the higher moments of the conserved charged distribution. In order to cancel the volume term in the susceptibilities, different combinations of the moments are constructed, such as $\frac{\sigma^2}{M}$, $S\sigma$, and $\kappa\sigma^2$, which can provide direct comparison of experimental results to lattice calculations. Thus at the critical point, one would expect large non-monotonic behavior of these products of moments as a function of beam energy. In addition, recent lattice QCD model estimations have proposed the extraction of freeze-out parameters of the collision from the analysis of higher moments of net-charge distribution. Among all conserved quantities, experimentally it is advantageous to study net-charge distributions. The fluctuations of net-charge include effects from net-baryon and net-strangeness. The much-awaited data from the RHIC Beam Energy Scan program have been successfully analyzed for Au+Au collisions at 7.7, 11.5, 19.6, 27, 39, 62.4 and 200 GeV. Various moments of the net charge distribution and also their products have been estimated as a function of centrality. The net-charge distributions have been corrected for centrality bin width correction and auto-correlations have been taken care of. Various methods have been used for estimating proper statistical errors. The procedures that correct the finite detection

efficiency of charged particles have been developed and implemented in this analysis. The centrality dependence of the moments has been understood by using the central limit theorem, which assumes that each of the collisions is a collection of a finite number of identical, independent emission sources. The statistical baseline for this analysis has been estimated by using Poisson and Negative Binomial expectations for the net-charge distributions. Various model simulations have also been done to understand the baseline for the critical point. The final results of the beam-energy dependence of the moments, mean, variance, skewness and kurtosis of net-charge distributions are presented as a function of collision centrality for Au+Au collisions at seven colliding energies from 7.7 GeV to 200 GeV. Event-by-event measurements of the net-charge distribution are made within the pseudorapidity range from -0.5 to 0.5 with full azimuth, and within the transverse momentum window of 0.2 to 2.0 GeV/c. The $\frac{\sigma^2}{M}$ increases with increasing beam energy. The centrality dependence of $S\sigma$ shows that the values are close to Poisson expectations for higher colliding energies, but deviations are observed at lower energies. The $\kappa\sigma^2$ values for peripheral collisions show no energy dependence. For the most central collisions, $\kappa\sigma^2$ show no significant variation as a function of beam energy. Freeze-out parameters have also been estimated from the products of the moments. A definite value for the Critical Point could not be established from the results. Higher statistics data at all energies as well as data for some more intermediate beam energy points will be needed to come to definite conclusion regarding the existence of the Critical Point.

Contents

List of Figures

List of Tables

Chapter 1

Introduction

It is believed that the Universe was created just after the hot Big Bang which was followed by rapid cosmological inflation under which the matter underwent several types of phase transitions. Within few microseconds of the birth of the Universe, matter consisted of mostly quarks and gluons, in a condition called the quark-gluon plasma (QGP). The deconfinement transition from QGP to hadronic matter took place around the same time, after which bare quarks were not to be found. This transition was governed by the theory of Quantum Chromodynamics (QCD). Dedicated experimental programs have been going on for the last few decades to search for the QGP matter in the laboratory and to understand the nature of the primordial matter in detail. At extreme temperature and/or pressure, normal matter undergoes a phase transition and QGP is formed. One of the major experimental program is to map the QCD phase diagram and to locate the Critical Point of the phase transition.

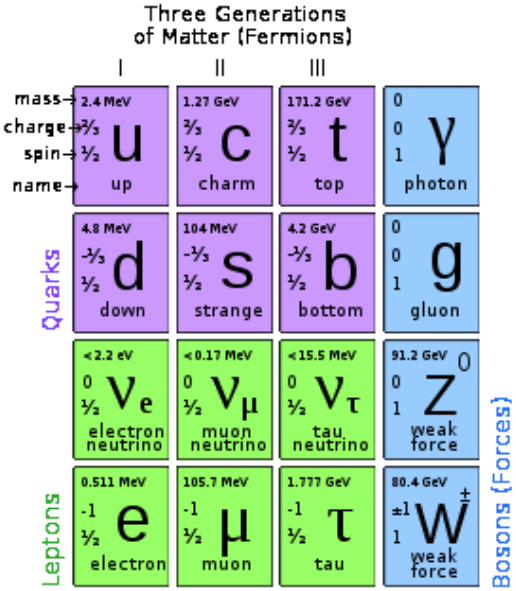

Figure 1.1: The standard model, constitute the building blocks of the universe.

1.1 Quantum Chromodynamics

Quantum Chromodynamics is the theory of the strong interactions between quarks and gluons. The quarks and gluons have three *color* charges, Red, Blue and Green analogous to electric positive and negative charges in Quantum Electrodynamics (QED). The different types of quarks, called *flavor*— u (up) , d (down), s (strange), c (charm), t (top) and b (bottom) — are divided into three generations as shown in Fig. 1.1. According to the quark model, the mesons and baryons — together known as hadron — are made up of two and three quarks, respectively. The mesons are made up of one quark and anti-quark, $(q\bar{q})$. whereas baryons consist of three quarks (qqq) and their anti-baryons are made up of their respective anti-quarks $(\bar{q}\bar{q}\bar{q})$.

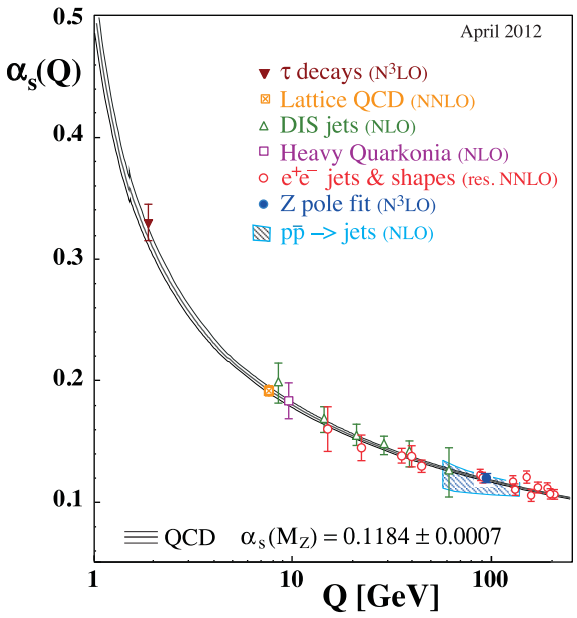

Figure 1.2: The running coupling α_s as a function of energy scale Q, measured in different experiments and from theoretical calculations [2].

1.1.1 Deconfinement and Asymptotic freedom

The two important properties of QCD are *Asymptotic freedom* and *Confinement*. According to the asymptotic freedom, the coupling between quarks and gluons decreases with the increase in momentum transfer. In other words, coupling between quarks and gluons becomes stronger with increase of the distance between them and weaker at short distances. Hence, the QCD is an asymptotically free theory. This was first discovered by Frank Wilczek, David Gross and David Politzer. This coupling strength as a function of energy scale is shown in Fig 1.2. The running coupling strength [1] is defined as

$$\alpha(Q^2) = \frac{12\pi}{(33 - 2N_f)log(Q^2/\Lambda_{QCD})}. \tag{1.1}$$

Here, N_f is the number of flavor and Λ_{QCD} is the QCD scale. This Λ_{QCD} makes the boundary between the quasi-free quarks and gluons, and hadrons (like, pions, protons, etc). The exact value of Λ_{QCD} is not known, but in theoretical calculations it is taken approximately to be Λ_{QCD} $\sim$200 MeV. Both the experimental data and theoretical results show the asymptotic variation of QCD coupling strength as a function of energy scale. Other aspect of QCD is confinement of color charged particles (quarks and gluons). This is the phenomenon that quarks and gluons cannot be isolated singularly. therefore quarks and gluons are not observed as free particles in nature. They are always confined inside hadrons.

After the discovery of asymptotic freedom, J.C. Collins and M.J. Perry suggested also that the hadronic matter, under high nuclear density or baryonic density, transit to QCD matter [3]. At extreme high temperatures, implying large momentum transfer, the quarks and gluons are asymptotically free. The phase where hadronic degrees of freedom transit to the phase of QCD matter, where color degrees of freedom plays significant role, is known as the QCD phase transition. And, this de-confined state of matter is coined as the Quark Gluon Plasma (QGP). Therefore, under extreme high temperature and/or baryon density, the new form of matter, QGP, can be created which was formed 10^{-6}s after the Big Bang during the creation of the universe. These two extreme limits motivate the experimentalists to perform heavy-ion-collision experiments in laboratory.

1.1.2 Quark Gluon Plasma and Heavy ion collisions

By colliding heavy-ions at ultra-relativistic energies, one can create a condition similar the one that existed within a few micro seconds after a Big Bang. Collision

of two Lorentz-contracted nuclei (pancakes), moving with almost the velocity of light, deposit a large amount of kinetic energy in a short space-time interval. This initial energy density results in particle production. At this time, mean free path of the particles becomes of the order of the size of the system created. The system tries to supercool and gets equilibrated through interaction among the partons. One assumes local thermodynamical equilibrium, where the energy, pressure, and temperature can be defined locally. After hadronisation, the hadron gas is produced which expands until feeze-out. The particles then stream in to the detectors. The multiplicity density at mid rapidity can be used to calculate energy density by Bjorken's energy density expression [28].

In heavy ion collisions, under extreme condition of temperature and/or baryonic density (or chemical potential), a transition of hadronic matter to QGP take place, where average kinetic energy of the partons is much larger than the potential energy between the partons. In the hadronic matter, isospin degrees of freedom dominate. On the other hand, isospin, color and flavor degrees of freedom plays significant role in the QGP state. For example, in ideal massless pion gas the degrees of freedom are 3 (three charge or isospin states) whereas in the QGP state the degrees of freedom are 37 ($= 2 \times 8 + \frac{7}{8}(3 \times 2 \times 2 \times 2)$). It includes two spin and eight color degrees of freedom of the gluons, three colors, two flavors, two spin and two particle-anti-particle degrees of freedom of quarks. The factor with 7/8 comes from the correct statistics consideration. The strong increase in pressure and energy density imply increase in degrees of freedom of QGP state. This type of transition is observed in lattice QCD simulation, where the energy density and pressure of QCD matter

abruptly increases at certain temperature as shown in Fig 1.3 [29].

1.2 Phase transition

In thermodynamics, phase transition are governed by the thermodynamical potential (or the Free energy) and its derivatives at the transition. As we know that first derivative of free energy with respect to the temperature, or external magnetic filed, gives the internal energy, the entropy, or the magnetization in magnetic material. The second order derivative is related with specific heat and susceptibilities or compressibility in fluid. Generally, phase transitions can be described by an order parameter that is zero in one phase (usually called the disordered phase), non-zero in the other phase (ordered phase). The order parameter plays a significant role in characterizing the phase transition, like magnetization plays as order parameter in the magnet, volume density in liquid-vapor transition, etc. In other words, in the presence of external field the symmetry in the matter is explicitly broken and the relevant order parameter then characterizes the phase transition [5].

In the infinite volume limit, if there is finite discontinuity in one of the first derivative of the thermodynamical potential then the transition is *first order* phase transition. The discontinuity is observed in the internal energy and entropy as a function of temperature at the transition point. The gap or plateau in entropy with respect to external field, for example temperature, is associated with the latent heat required during the first order phase transition. But there may be latent required heat without gap in the order parameter at the transition point. According to Ehrenfest classification of phase transition, the *nth-order transition* are defined by

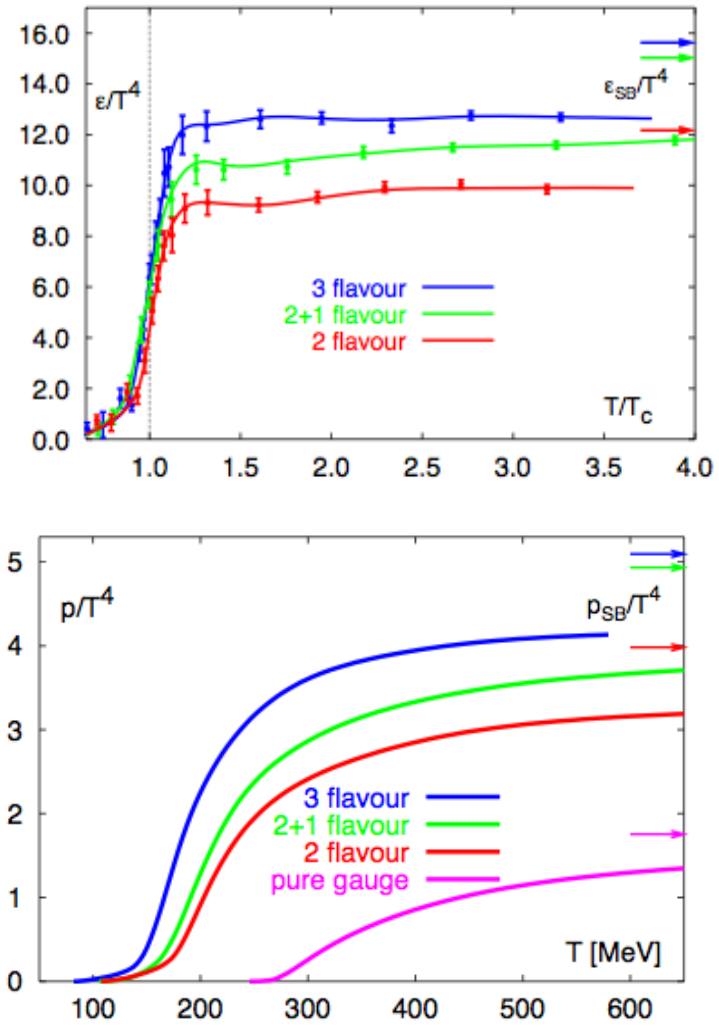

Figure 1.3: The energy density (upper panel) and pressure (bottom panel), normalized by temperature, in QCD with different number of degrees of freedom as a function of temperature [29].

the presence of the discontinuity in the *nth-order derivative* of the thermodynamical potential. According to M. E. Fisher, in *continuos* (or *crossover*) transition, the first derivative of the thermodynamical potential is continuos, whereas *second derivative* is either discontinuous or divergent. In *second order* transition, one of the second derivative of the thermodynamical potential is divergent, hence susceptibilities and specific heat diverge at the *second order* phase transition. The end point of the first order phase transition, where *second order* transition starts, is known as *critical point*.

1.2.1 QCD Phase Diagram

The first QCD phase diagram was proposed in 1975 by Cabibbo and Parisi [6]. They proposed that the exponential increasing of mass spectrum (by Hagedron) may lead to a second order phase transition for hadronic matter. The quarks lead to the confined state in the low temperature region and starts deconfine at high temperature limit. At that time no idea of chiral symmetry or non-perturbative polyakov loop were familiar to the QCD phase transition. Figure 1.4 shows the prevalent conjecture of the QCD phase diagram in $T - \mu_B$ plane. The transition from hadronic matter to QCD matter, Quark-Gluon Plasma, can be envisaged by the deconfinement and chiral symmetry restoration. For the QCD phase transition, mass of the quark, number of flavor and color of quarks play significant role in determining the order of phase transition. In the limit of infinite quark mass, $m_q \to \infty$, for all quark flavor, at $\mu_B = 0$, the transition from hadronic to deconfinement is a *1st order*. In the chiral limit, $m_q \to 0$, the phase transition corresponds to the chiral symmetry restoration and it is also a 1st order phase transition for *u, d* and *s*

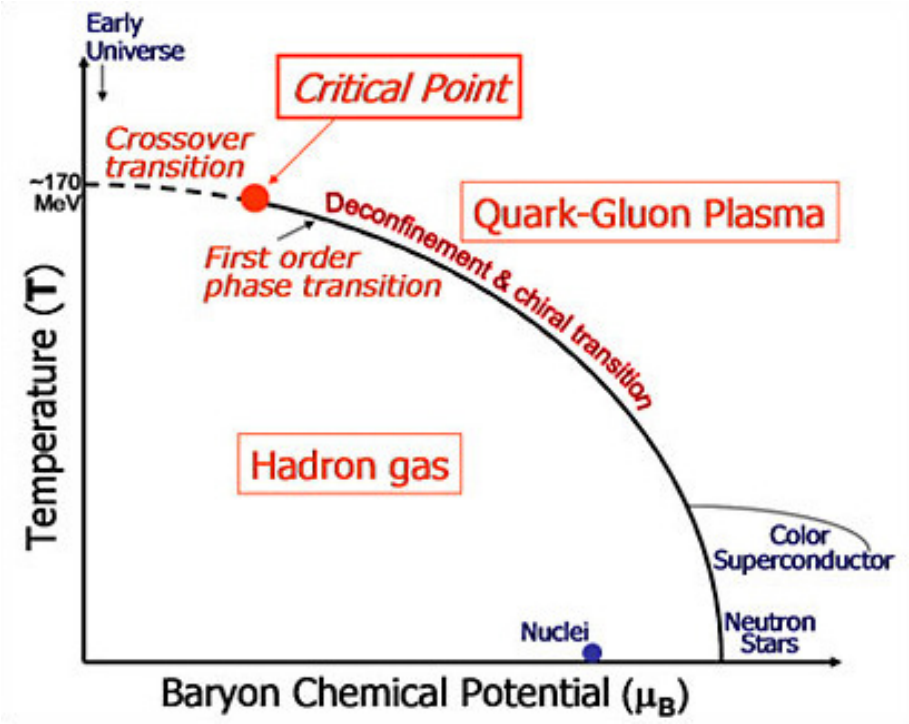

Figure 1.4: The conjecture of the QCD phase digram in terms of the temperature (T) and chemical potential (μ_B) [7].

quark flavor [9]. The chiral transition is of *2nd Order* for $m_{u,d} = 0$ and mass of the strange quark, $m_s > m_s^{tri}$. This limiting point of the strange quark mass, $m_s = m_s^{tri}$ is known as *tri-critical point* [10]. While going from $m_q = 0$ to $m_q = \infty$, there is a smooth *cross-over* from confinement to deconfinement transition. Whereas in the real world non of the quark is the massless and nor infinitely large. Therefore for the current quark mass, the existence of the true *critical point* is still questionable. Therefore, the quark mass plays a key role for the understanding of the QCD phase transition and the schematic representation using quark mass (known as Columbia plot) is shown in Fig 1.5. In this plot, the first order transition for the deconfinement and chiral symmetry are shown at the two corners (bottom-left and top-right) of the diagram. In the QCD phase transition, there should be an order parameter which behaves differently for the two-phase. In the case of chiral symmetry, it is chiral condensate, $< q\bar{q} >$ and the Polyakov loop, L, for the deconfinement transition Ref [29]. The behavior of these order parameters responding two phase are listed below.

chiral symmetric phase:	$< q\bar{q} > \neq 0$
chiral broken phase:	$< q\bar{q} > = 0$
quark confinement phase:	$L = 0$
quark deconfinement phase:	$L \neq 0$

In Fig 1.4, at $\mu_B = 0$, there is a non-analytic *cross-over* from hadronic to QGP phase. whereas at large μ_B, the *1st Order* transition is speculated between two these phases [11, 12, 13]. It is expected that there is an end-point of the *1st Order* phase transition line, which is known as QCD *Critical Point* . At extremely large baryon

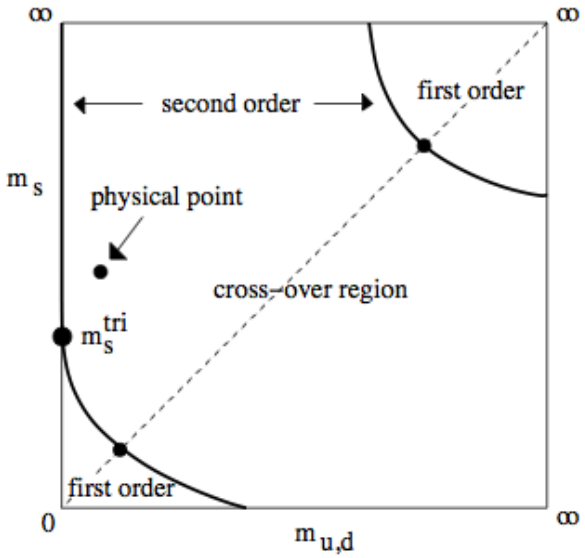

Figure 1.5: Columbia plot for the QCD phase transition for 3-flavor QCD at $\mu_B = 0$ [10].

density, $\mu_B >> \Lambda_{QCD}$, the coupling between QCD matter becomes asymptotically free. Analogy to condense matter, like electron makes Cooper pair in m etal (superconductor), quarks in the quark matter, at low T, form Cooper pair and leading to *Color superconductor* [14].

1.2.2 QCD Critical Point and its signatures

Lattice QCD calculations [15, 16], at vanishing chemical potential, reveals that the fluctuations of the net-charge, net-baryon number and net-strangeness are very sensitivities to the critical fluctuation. In (2+1)-flavor lattice QCD calculations, at zero chemical potential, the quadratic fluctuations rise rapidly and quartic fluctuations show a maximum values for net-charge (Q), net-baryon (B) and net-strangeness (S) at the transition region, going from hadronic to partonic regime. The higher order

moments such as variance (σ^2), skewness (S) and kurtosis (κ), discussed in Section 4.1, of the conserved charges (X = Q, B, and S) are related to respective higher order susceptibilities.

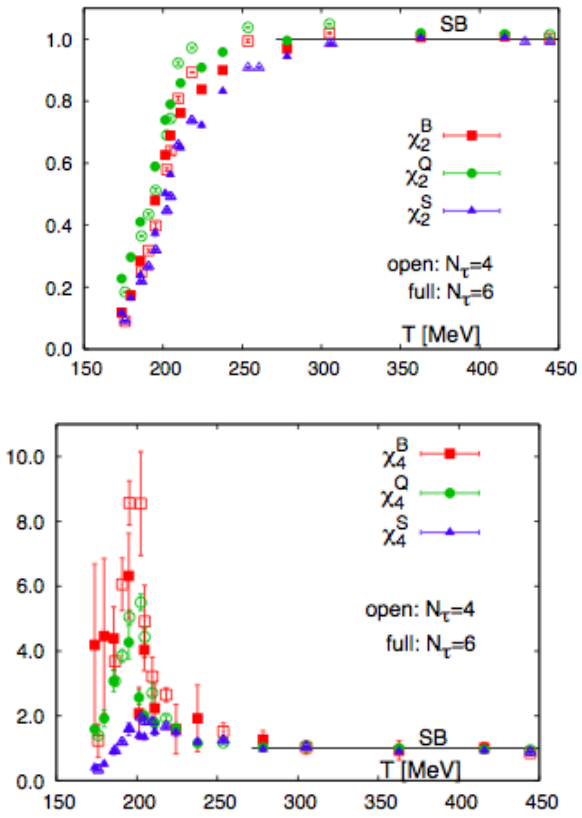

Figure 1.6: The quadratic (top panel) and quartic (bottom panel) susceptibilities for for net-charge (Q), net-baryon (B) and net-strangeness (S)[15].

In Fig. 1.6, the quadratic susceptibilities ($\chi_2^{B,Q,S}$) of the net-baryon number, net-charge and net-strangeness show rising trend up to transition temperature, whereas at this temperature the quartic susceptibilities ($\chi_4^{B,Q,S}$) show large jump. It is observed that in quadratic susceptibilities the net-charge sector shows large deviation

than net-baryon number and net-strangeness whereas for quartic net-baryon sector shows larger jump than net-charge and net-strangeness. Above transition temperature all the susceptibilities become same and equal to Stefan-Boltzmann limit (ideal, massless quark gas). In Fig. 1.7, the ratio of the quartic to quadratic susceptibilities of net-charge shows a large jump at transition temperature at zero chemical potential. The HRG model prediction also shows rising trend above unity. The $6th$ order to $2nd$ order susceptibilities of net-charge shows large fluctuation at transition temperature at vanishing chemical potential.

Beside this, other QCD based model calculations [17](like σ-model) shows that the correlation length, ζ, of the system are related to the various moments of the conserved charges as follows,

$$\sigma^2 \sim \zeta^2; \quad S \sim \zeta^{4.5}; \; \kappa \sim \zeta^8. \tag{1.2}$$

In the thermodynamical limit, the correlation length diverges at the critical point [18]. The higher order moments such as skewness and kurtosis grow faster as compared to variance of the conserved charge distribution.

Other QCD based estimations [19], in the mean-field approximation, the third moments (skewness) of the net-charge, net-baryon and energy distributions carry information about the phase boundary in QCD phase transition. The sign change of skewness, at the phase transition line, reveal the existence of the divergence of susceptibilities. The QCD based Ising model calculation [20] reveals the negative kurtosis in the phase transition line manifest the presence of critical point approaching from the crossover line.

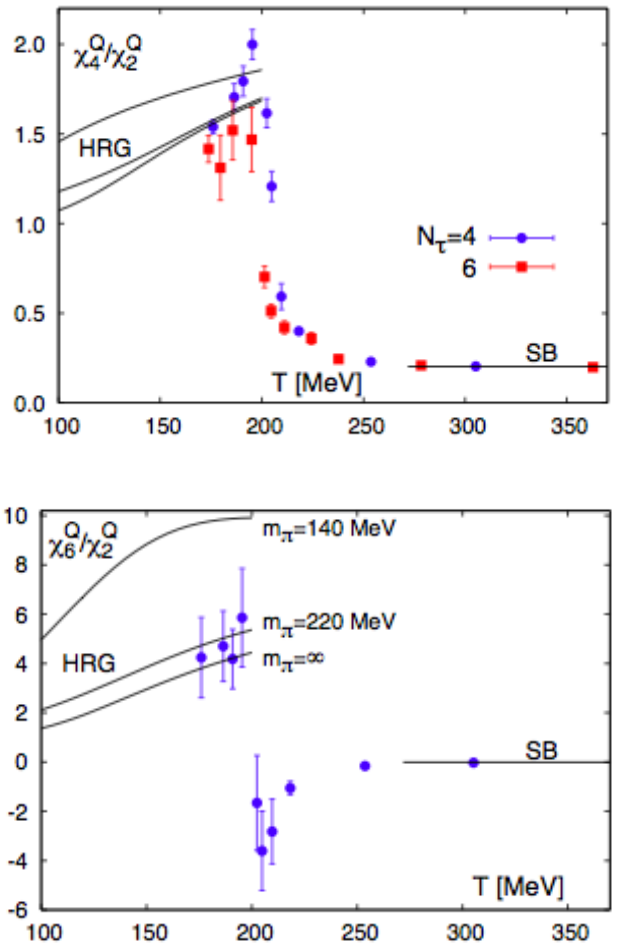

Figure 1.7: The ratio of quartic to quadratic (top panel) and $6th$ order to $2nd$ (bottom panel) order susceptibilities of net-charge distribution [15].

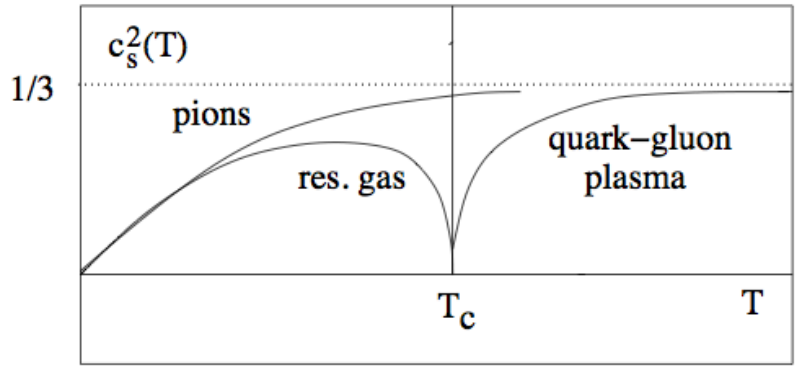

Figure 1.8: The speed of sound with respect to T in QCD matter and ideal pion gas [10].

Various other theoretical calculations which include interactions of quarks with effective gluon fields such as the Polyakov loop extended Nambu-Jona-Lasinio (PNJL) [22] and the quarkmeson (PQM) [23] models also show that ratios of χ_Q^4/χ_Q^2 and χ_Q^6/χ_Q^2 for the net-charge exhibit large peaks at the critical temperature in the chiral limit [24].

In addition, the speed of sound, c_s^2, which is defined as the change in pressure with respect to that of energy density at constant volume $(\frac{\partial P}{\partial \epsilon})_V$, vanishes at T_c as shown in Fig 1.8. This decrease in speed of sound is because of the production of resonances where there is no increase in kinetic energy in the system. This behavior is observed in lattice QCD calculations [25].

Various QCD based model calculations and Lattice simulation predict different points in the QCD phase diagram to be the critical point as shown in Fig. 1.9. The exact location of the critical point may be accessed through the Heavy-Ion-Collisions

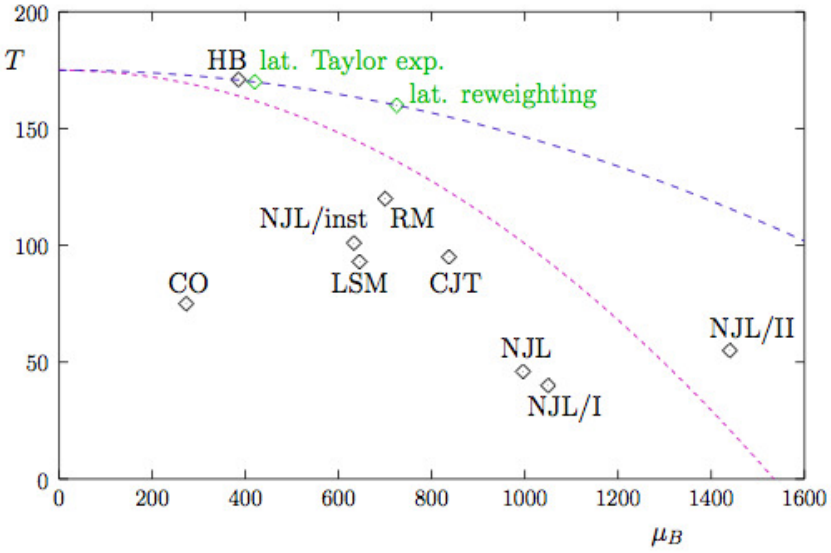

Source	(T, μ_B), MeV	Comments	Label
MIT Bag/QGP	none	*only 1st order, no chiral symmetry*	—
Asakawa,Yazaki '89	(40, 1050)	NJL, CASE I	NJL/I
"	(55, 1440)	NJL, CASE II	NJL/II
Barducci, *et al* '89-94	$(75, 273)_{\rm TCP}$	composite operator	CO
Berges, Rajagopal '98	$(101, 633)_{\rm TCP}$	instanton NJL	NJL/inst
Halasz, *et al* '98	$(120, 700)_{\rm TCP}$	random matrix	RM
Scavenius, *et al* '01	(93,645)	linear σ-model	LSM
"	(46,996)	NJL	NJL
Fodor, Katz '01	(160, 725)	lattice reweighting	
Hatta, Ikeda, '02	(95, 837)	effective potential (CJT)	CJT
Antoniou, Kapoyannis '02	(171, 385)	hadronic bootstrap	HB
Ejiri, *et al* '03	(?,420)	lattice Taylor expansion	

Figure 1.9: The theoretical predictions for the QCD critical point in $T - \mu_B$ plane (upper plot) and the table (lower panel) for the list of the theoretical prediction [21].

at energies close to the predictions.

The main challenges, to probe the critical point, are the finite size and time effects in heavy-ion-collisions. Due to the finite size of the fireball created during heavy-ion-collision, the system survives for a finite time. It restricts the correlation length, ζ, to grow. It has been shown that the finite size effect restrict ζ to be 6 fm [26]. In addition to this, if the system had infinite size, then ζ grows infinitely large at critical point and hence it takes infinite time to grow. This is known as *critical slowing down*. It has been shown that finite size effect affects critical slowing down. The combined effect of the finite size and critical slowing down makes the correlation length 3 fm at most [27]. This makes the heavy-ion-collision experiment viable to access the signal of the critical point by event-by-event fluctuation analysis. To achieve this goal Relativistic Heavy Ion Collision at BNL proposed Beam Energy Scan program. The details are discussed in next section.

1.3 A glimpse of experimental signature of QGP

Some of the signatures of QGP have been observed in heavy-ion collisions at RHIC [4]. The high-p_T hadron measurement in relativistic collisions reveals strong suppression for inclusive charged particles [30] as shown in Fig.1.10. In addition, while no suppression in the two particle azimuthal distribution of back-to-back jets is observed in d+Au and p+p collisions, there is a strong suppression in Au+Au collisions indicating the formation of the dense medium during the initial stage of the collisions [30] as shown in Fig 1.10. On the contrary, Fig 1.11 shows the nuclear modification factor for direct photons which shows no suppression while other neutral particles

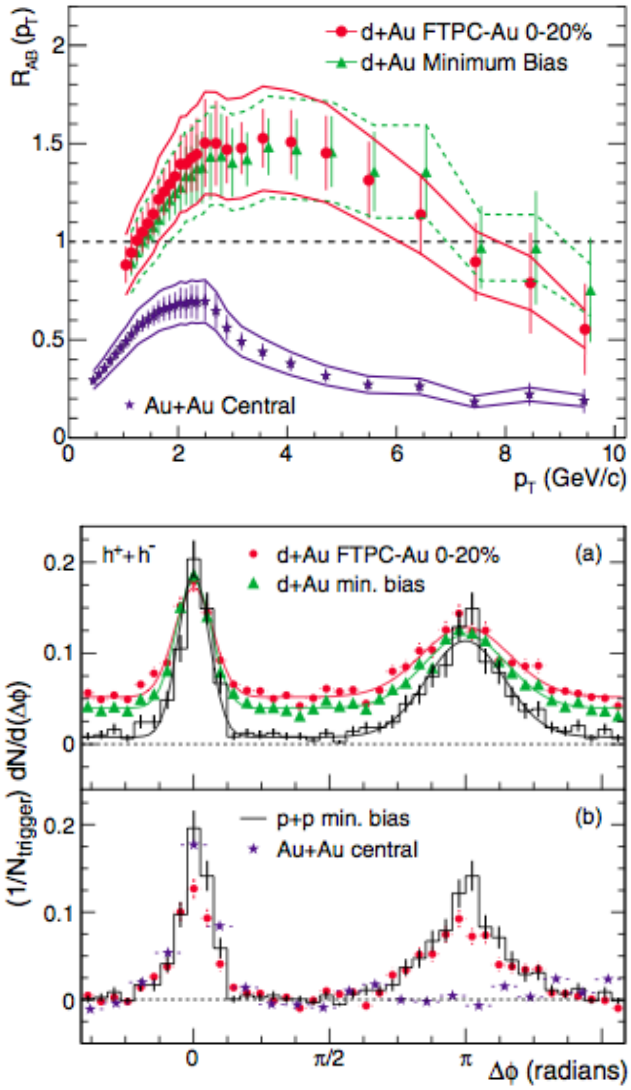

Figure 1.10: The nuclear modication factor ($R_{AB}(p_T)$)for minimum bias and central d+Au collisions, and central Au+Au collisions (upper panel) and the two particles azimuthal distributions (bottom panel) for d+Au, p+p and Au+Au collisions at 200 GeV center of mass energy [30].

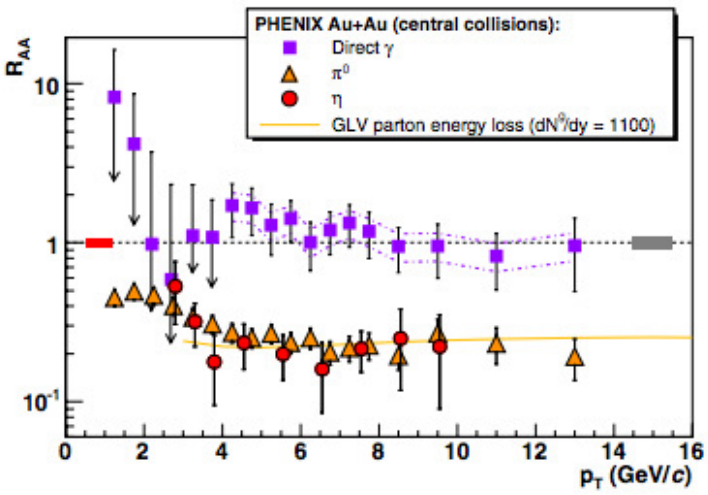

Figure 1.11: The nuclear modication factor ($R_{AA}(p_T)$) measured in central Au+Au at colliding energy 200 GeV for π^0, η and direct photon [31].

such as π^0 and η are suppressed [31]. This is because the photon interacts through electromagnetic interaction while mesons interact through strong interactions. The soft part, mainly $p_T < 2$ GeV, of the transverse momentum carry the bulk properties of the system. Bulk properties of the system, like particles yield, flow, particles correlation, multiplicity etc. carry information about the dense medium. In heavy-ion-collisions, once the hot and dense matter created gets thermalized the inelastic collisions ceases, which is called chemical freeze-out, (T_{ch}) , After this there is no further particles production. After chemical freeze-out, the kinetic freeze-out occurs, where no further change in kinetic energy occurs. In Fig 1.12, the statistical thermal (assuming thermalization of the system) fit with the data shows the chemical freeze-out temperature, $T_{ch} = 160\pm4$ MeV and chemical potential $\mu_B = 24\pm4$ MeV [34] for Au+Au collisions at $\sqrt{s}_{\rm NN}$= 200 GeV. Similarly the kinetic freeze-out information can also be estimated from the hadronic spectra at given collision energy. With the

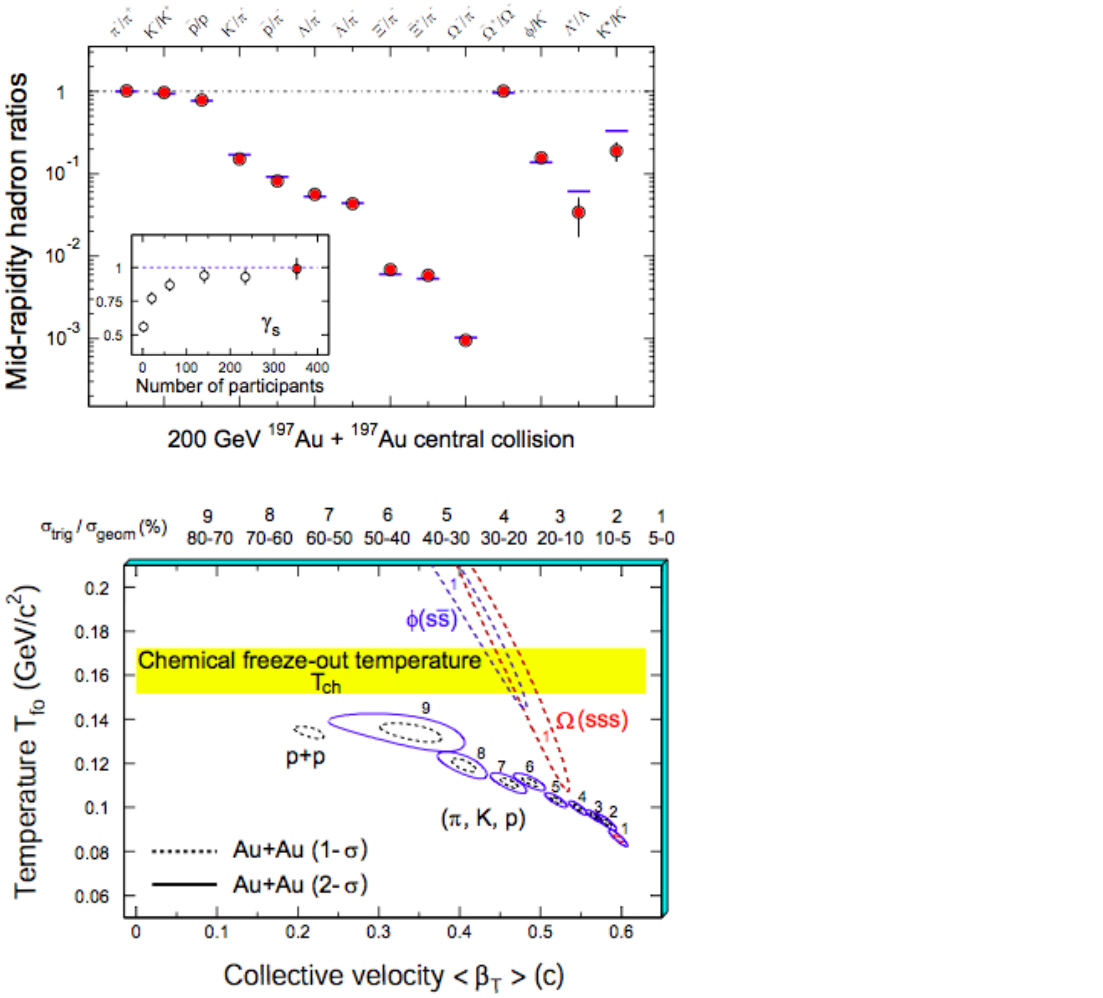

Figure 1.12: (Upper panel) Transverse momentum integrated hadron ratio at mid rapidity for Au+Au collisions. The horizon bars represent statistical model fits to the measured yield ratios for stable and long-lived hadrons. (Bottom panel) The T_{fo} as a function of average radial flow, $< \beta_T >$, are plotted for different centrality [34].

help of hydrodynamical motivated model and comparing with the experimentally measured different particles spectra, the kinetic freeze-out temperature, T_{fo} and the collective component have been estimated as shown in right panel of Fig. 1.12.

Besides these, the collective component arises due to the gradient of matter density from center to periphery of the collision geometry. This matter gradient creates a outward push to the inside matter and hence a collective flow develops. The types of flow depend on the initial collision geometry like, radial (central collisions), elliptic (peripheral collisions), etc. In Fig. 1.13, v_2, the measure of elliptic flow is shown as a function of p_T for mesons and baryons. It is observed v_2 scales with the number of valence quarks implying that partonic degrees of freedom develop at an early stage of collisions. This partonic stage could be one of the possible signatures of QGP.

In Ref. [32], it is argued that the plateau region in mean transverse momentum as a function of multiplicity density (proxy of colliding energy) will indicate the possible signature of the onset of the QGP formation and hadronic mixed phase. It is analogous to latent heat required for the 1st order phase transition. In Fig. 1.14 shows the energy dependance of mean transverse mass, $< m_T >$, $m_T = \sqrt{m^2 + p_T^2}$ where m rest mass, of π, K, p and $\bar{p}$ [33]. It is observed, above $\sim$ 10 GeV energy the mean transverse mass remains flat as function of energy. It could be signature of the 1st order phase transition for the QGP formation. Beside this, ratio of positive charged kaon to pion, K^+/π^+, shows a peak around 7 GeV colliding energy [33], which also could be signature of onset of de-confinement. There are ample of evidence for the formation of QGP. The detail properties of QGP and the transition of normal hadronic matter to QGP matter is under study both theoretically and ex-

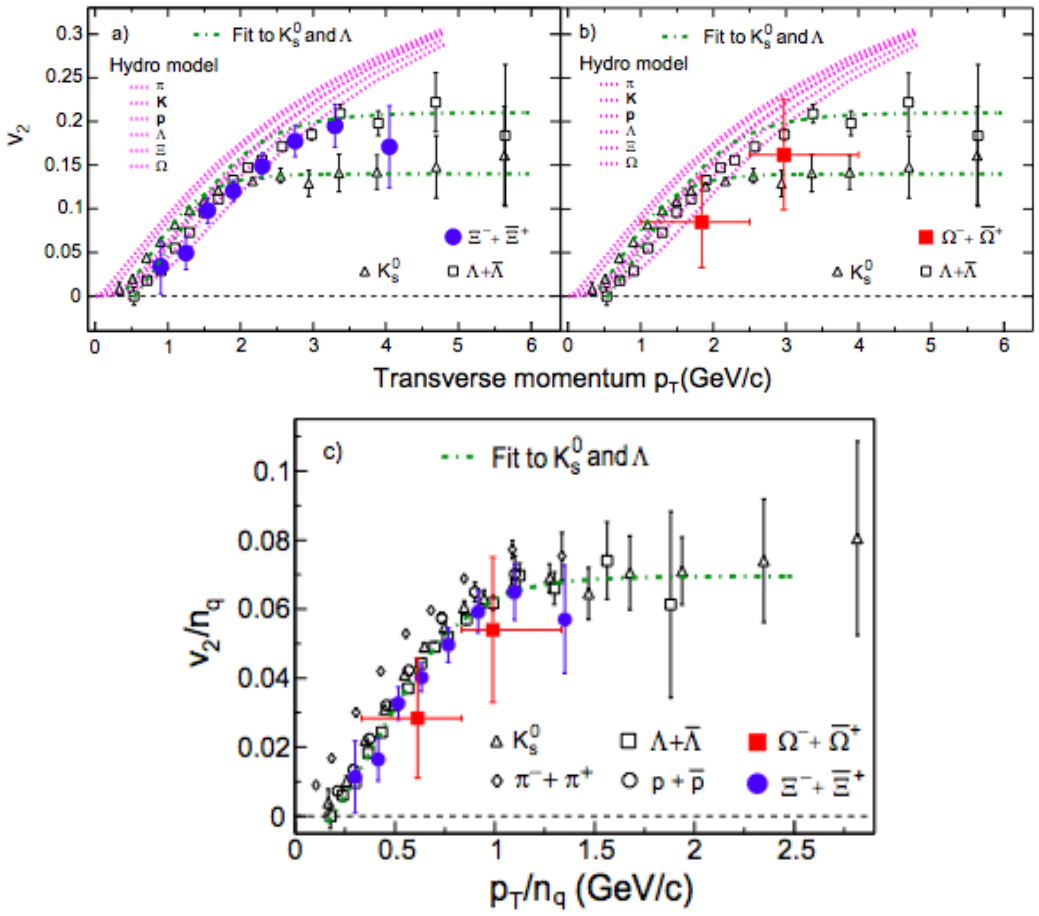

Figure 1.13: (a) The transverse momentum dependance of v_2, measure of elliptic flow, for various hadrons species in minimum bias Au+Au collisions at $\sqrt{s}_{\rm NN}$= 200 GeV. (b) The number of valence quark scaling of the v_2 for baryons and mesons in minimum bias Au+Au collisions at $\sqrt{s}_{\rm NN}$= 200 GeV [34].

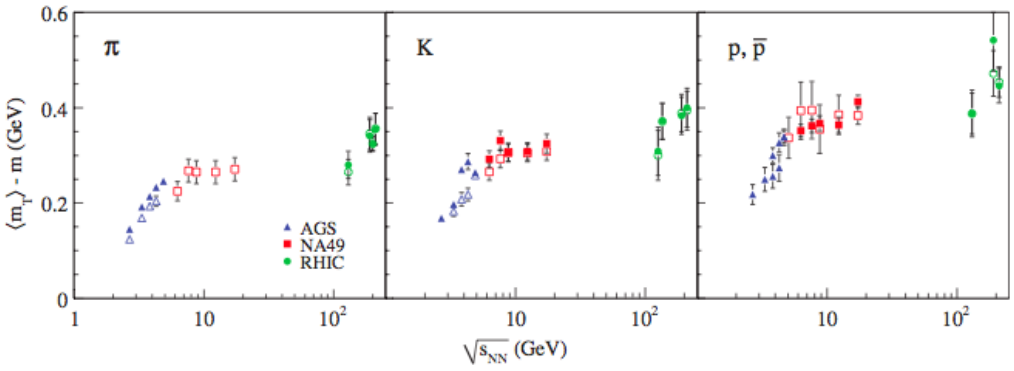

Figure 1.14: Mean transverse mass as a function of colliding energy for π, K and p for Pb+Pb and Au+Au Collisions [33].

perimentally. The RHIC and LHC are the dedicated ongoing heavy-ion-experiment for the understanding of this new form of matter.

1.4 Experimental overview on the search of QCD Critical point

In spite of experimental challenges, as discussed previously , the intense search for the QCD critical point and its signatures have been undertaken from SPS to RHIC experiments. In NA49 experiment, transverse momentum fluctuation, Φ_{p_T}, [35, 36] and the particle multiplicity fluctuation (the scaled variance) [37], ω, are used. In this experiment, central Pb+Pb collisions are studied at 20A, 30A, 40A, 80A, and 158A GeV collision energy. Both Φ_{p_T} and ω, measure of transverse and particle multiplicity fluctuation, show no increase or non-monotonic behavior [36, 37] as a function of colliding energies. The system size dependance of the above fluctuations are also studied for intermediate system C+C and Si+Si interaction at 158A GeV. The higher moments of p_T fluctuation, $\Phi^{(n)}{}_{p_T}$ have also been studied to amplify the

signal of the critical point in the above colliding system. No critical point signature has been found in these results. Besides, it was suggested also that particle ratio fluctuation might also provide the signature of critical point because hadron production at freeze-out carry the of the nature of the deconfinement phase transition. The NA49 [40] and STAR [39] experiments have also analyzed the data for dynamical fluctuation, σ_{dyn}, for the particle ratio like K/π, p/π, and K/p. In this case, the difference of the width of the particle ratio fluctuation for data and that of the mixed events are considered the dynamical fluctuation of particle ratio. These results show no non-monotonic behavior as a function of the beam energies.

The NA49 intermittency result shows some clue for the presence of QCD critical point. In this analysis, second factorial moments, F_2, of low-mass $\pi^+\pi^-$ pair in central Si+Si interaction at 158A GeV (which is $\sqrt{s}_{\rm NN}$= 17.8 GeV) are studied. The magnitude of the net-proton and σ field are characterized by the order parameter for the second order phase transition associated with QCD critical point. In this case, difference of F_2 between data and mixed events, $\Delta F_2(M)$, as a function of transverse momentum space of bin, M, shows intermittency signal in the data. The intermittency results for the Si+Si system approaches the QCD critical point prediction [38]. These results provides strong evidence for existence of the critical point in the proximity of the Si+Si and Pb+Pb freeze-out state.

Future experiments like NA61/SHINE at the CERN SPS, which is the successor of the NA49 experiment, is dedicated experiment for the search of the critical point. Whereas RHIC beam energy scan program aims to probe the QCD critical point in

wide range of the temperature and baryon chemical point. Detail about the RHIC beam energy scan ($5 < \sqrt{s}_{\rm NN} < 39$ GeV) program has been discussed in the chapter 2. Besides this future collider JINR NICA ($3 < \sqrt{s}_{\rm NN} < 9$ GeV) and GSI FAIR ($2.3 < \sqrt{s}_{\rm NN} < 8.5$ GeV) have also planned of the search for QCD critical point.

1.5 Extraction of Freeze-out parameter

In heavy-ion-collision, statistical thermal model explains the hadronization process where particles are believed to be produced from the thermal equilibrium at freeze-out surface. This is to some extent understood by the HRG models. This freeze-out surface is described by the freeze-out parameters such as, Temperature, T_f and baryon chemical potential, μ_f. These freeze-out parameters are very useful to understand the phase boundary in QCD phase diagram. These freeze-out information can be accessed by comparing lattice QCD based calculation of higher order susceptibilities of conserved quantities with experimentally estimated higher order moments of the conserved charge distribution. The detail theoretical work can be found in the Ref. [41][42]. In this recent work, it has been seen that $R^Q{}_{12}$ and $R^Q{}_{31}$ shows strong dependance on μ_B and T, respectively, as shown in Fig 1.15. These are related to the experimentally estimated $\frac{M}{\sigma^2}$ ($= R^Q{}_{12}$) and $\frac{S\sigma^3}{M}$ ($=R^Q{}_{31}$) of net-charge distribution.

Therefore, using $\frac{M}{\sigma^2}$ and $\frac{S\sigma^3}{M}$, freeze-out temperature and baryon-chemical potential can be estimated by direct comparison of data to Lattice QCD simulation. The beam energy scan data from RHIC can also give information about the freeze-out surface in the QCD phase diagram.

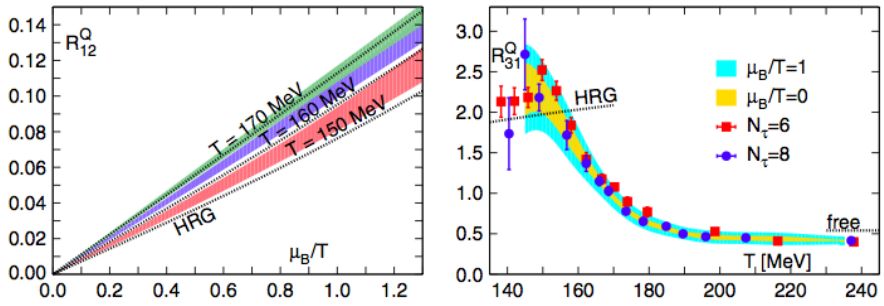

Figure 1.15: Diagrammatic representation of two limiting cases of Binomial distribution [41].

1.6 Organization of the thesis

The thesis is organized as follows. In Chapter 2, the details about the Relativistic-Heavy-Ion-collider (RHIC) are mentioned. The goals of beam energy scan program and data taken in the years 2010 and 2011 are discussed. In Chapter 3, the STAR detector and trigger system are discussed. The higher moments of the multiplicity distributions, moments generating function and the relation between higher moments and thermodynamical quantities have been introduced in Chapter 4. Besides these, various baseline measurements like, Hadron Resonance Gas, results from various event-generators, Poisson and Negative Binomial expectations have been discussed. In addition to these, extraction of freeze-out parameters from the higher moments of net-charge distribution has been introduced in this chapter. Details of the analysis for higher moments of the net-charge distribution has been discussed in Chapter 6. In this chapter, data sets, events and charged particles selection procedure are discussed. Beside these, centrality bin width correction, new centrality determination, central limit theorem, both statistical and systematic uncertainty, and finally efficiency correction for the higher moments have been discussed in details. In Chapter 7, the results for the higher moments of the net-charge distribution

and their products such as, $\frac{\sigma^2}{M}$, $S\sigma$ and $\kappa\sigma^2$, have been discussed. Finally, the $\frac{M}{\sigma^2}$ and $\frac{S\sigma^3}{M}$ have been compared with that of Lattice results to extract freeze-out parameters. In Chapter 8 and 9, the summary and outlook of the thesis have been discussed, respectively.

Chapter 2

RHIC Beam Energy Scan Program

2.1 Relativistic Heavy Ion Collider

The Relativistically Heavy Ion Collider (RHIC), located at the Brookhaven National Laboratory in Upton, New York, is a dedicated collider to study QCD. It began operation in 2000 after 10 years of the development, construction and commissioning. RHIC has two independent storage rings particle accelerators (arbitrarily assigned as "Blue" and "Yellow" rings) as seen in Fig. 2.1. These double storage rings are hexagonal shaped and 3.8 km long in circumference. The six interaction points (between the particles circulating in the two rings) are in the middle of the six relatively straight sections, where the two rings cross, allowing the particles to collide. The interaction points are enumerated by clock positions, with the injection near six. Two large experiments, STAR and PHENIX, are located at six and eight respectively.

RHIC drives two intersections beam of gold (Au) ions collisions. In the acceleration of heavy-ions, the journey of ions starts from Tandem to RHIC with various stages. At the first stage, the electrons are stripped out from the Au ions by the

Tandem van de Graaff accelerator with 2 MeV per nucleon of the kinetic energy and a charge state of +32. The beam or bunch of ions enters from the Tandem to the Booster, with a speed which is at about 5% the speed of light. The particles are transferred to a the small circular Booster — known as Booster Synchrotron. The ions are accelerated to higher energy — at this stage, each ion has a charge state of +77. These highly-energetic-ions are injected into the Alternating Gradient Synchrotron (AGS) at about 37% the speed of light. As they whirl around the AGS and get accelerated, the ions get more energetic at about 99.7% the speed of light and with charge of +79 state (with no electrons left). The beam is injected then into the two rings of RHIC via a beam-line, known as AGS-To-RHIC (ATR) transfer line. At the end of this line, there is a "fork in the road," where a switching magnet bifurcates the ion bunches into one of two (red and blue) beam line.

In Fig. 2.2, the colliding energy w.r.t luminosity (left y-axis) and collision rate (right y-axis) are plotted for different collision geometries, like p, S, I and Au, in RHIC and AGS regime [53]. The luminosity and collisions rate decrease with decreasing colliding energy in RHIC system.

2.2 Beam Energy Scan Program at RHIC

The RHIC experiments have claimed the formation of new form of matter — known as QGP. It draws many attentions, both from the experimentalists and theorists, to understand properties of QGP. To explore the wisdom about this new form of matter, RHIC started its beam energy scan program in 2010.

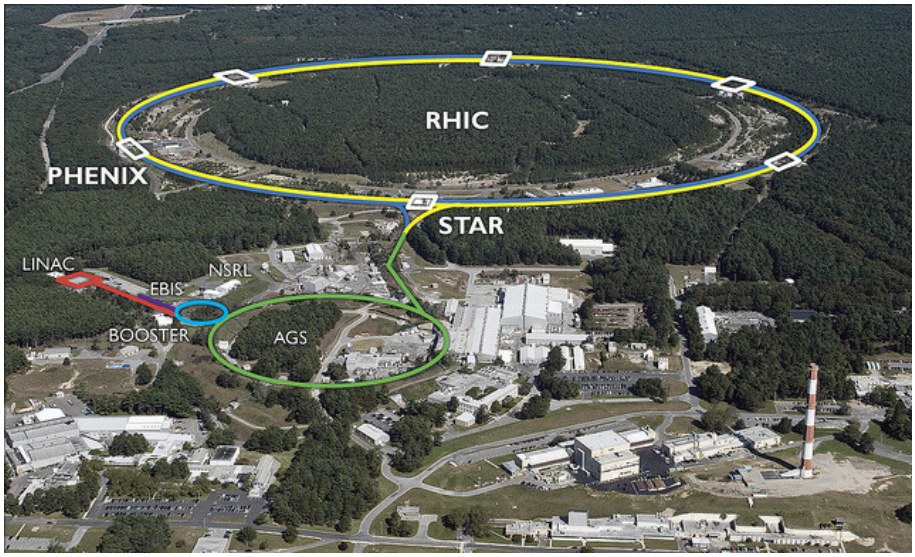

Figure 2.1: RHIC's 2.4 mile ring has six intersection points where its two rings of accelerating magnets cross, allowing the particle beams to collide.

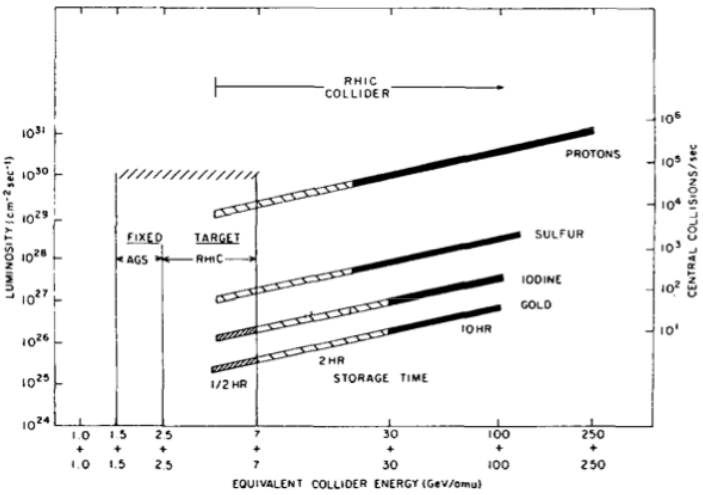

Figure 2.2: RHIC collider capabilities in comparison with AGS. For various colliding species from p+p to Au+Au collisions for its wide range of collision energies. The left y-axis represents luminosity and that of right side represents collision rate (sec^{-1}) Ref. [53].

2.3 Physics goal

The main goals of the beam energy scan program at RHIC are

- to locate the existence of Critical Point in the QCD Phase diagram,
- to find the evidence of the first order phase transition in the QCD Phase diagram, and,
- to understand the properties of the QGP as a function of baryon chemical potential.

Many theoretical developments have been made both in QCD as well as in statistical thermodynamic fields to understand the complex nature of the QGP matter. The intriguing phenomena in QGP matter such as, constituent-quark-number scaling of v_2, hadronic suppression in central collisions, local parity violation in strong interaction, etc, manifest the potential signature of the partonic plasma. The statistical thermal model approach has been made to understand the temperature and chemical potential at the time of freeze-out of QGP. Figure 2.3 (left side) shows the variation of temperature and chemical potential by controlling the colliding energy. Therefore, in the heavy ion collision, varying colliding energy the QCD phase diagram can be mapped in temperature and chemical potential plane. The variation of the RHIC colliding energy from $\sqrt{s}_{\rm NN}$= 7.7 to 39 GeV along with 62.4 and 200 GeV covers the baryonic chemical potential from 410 to 20 MeV [67]. This program provides a access to suitable and most interesting region in QCD phase diagram to understand the bulk properties of the QGP.

Why RHIC is suitable for beam energy scan?

Experimentally, RHIC's running collider experiments, STAR and PHENIX, provides unique facilities for the beam energy scan program. The variation of particle density (occupancy) in collider and fixed target experiments is shown in Fig. 2.4. It shows that occupancy increases linearly with increasing center of mass energy in the fixed target experiments whereas that in the colliding experiments varies negligibly. This helps in better track reconstruction efficiency and particle identification in colliding experiments as compared to fixed target experiments. Much larger center of mass energy can be produced by collider experiment than the fixed target experiment. The phase space variation in colliding experiment is less in the fixed target experiment, that helps to understand the underlying physics from the wider colliding energy range. Besides, RHIC is able to collide with a wide range of collision energy for Au+Au collisions at nearly constant collision rate and luminosity. On the other-hand, from the physics point of view, the initial temperature can be expected to increase by a factor of 2-4 in going from fixed target to collider experiment [70]. The initial temperature (T) changes with the initial energy density, ϵ, (for ideal gas $\epsilon \propto T^4$). For fixed heavy ion collision geometry, Au+Au, RHIC can vary its initial temperature and energy density of the system formed during *little bang* by varying only collision energy.

2.4 Beam energy scan program details

RHIC is able to run from varied energy range from $\sqrt{s}_{\rm NN}$= 5 GeV to 200 GeV for Au+Au collisions. The recent PID upgrade of the Time of Flight detector in STAR experiment has strengthened the particles identification capabilities which would

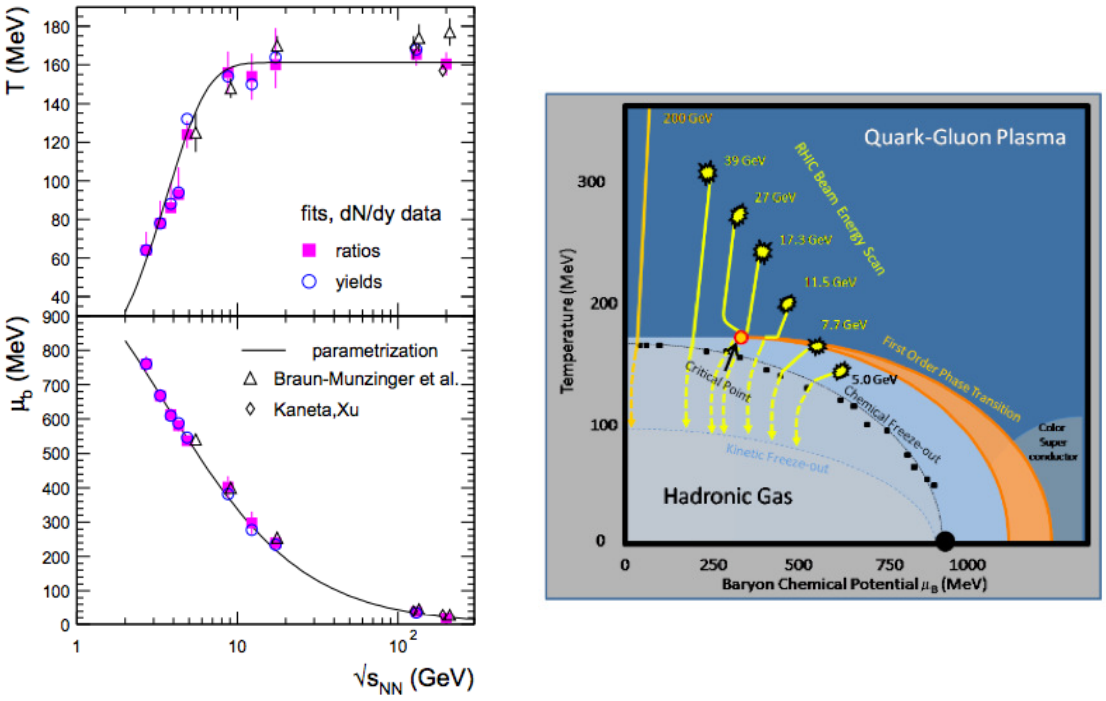

Figure 2.3: (Left side)Relation between freeze-out temperature and chemical potential with respect to colliding energy [65]. (Right side) RHIC Beam Energy Scan program and schematic QCD phase diagram [66].

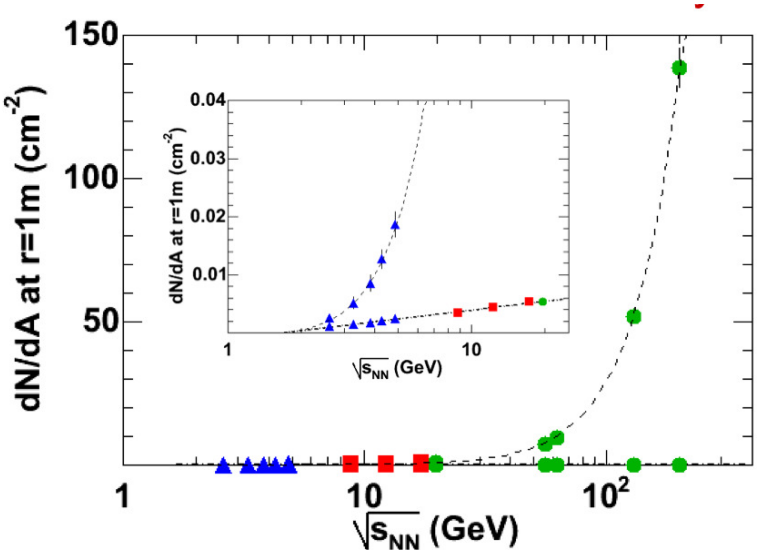

Figure 2.4: Particles density (occupancy) for fixed target and collider experiment for different collision energy. [69].

help in the search of the critical point. RHIC's upgrade on electron cooling system increases the luminosity at low energies.

The RHIC beam energy scan program had started in the year 2010 (RUN 10) and first phase of the beam energy scan has been finished in 2011 (RUN 11). In the table 2.1, the details about the RUN 10 and 11 have been listed. The integrated nucleon-nucleon pair luminosity (pb^{-1}) as function of the physics running time (weeks) are shown in the Fig. 2.5.

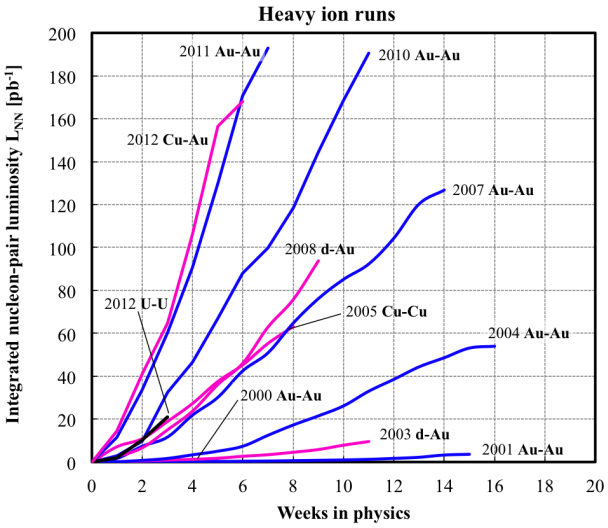

Figure 2.5: The nucleon-pair luminosity is defined as $L_{NN} = A_1 A_2 L$, where L is the luminosity, and A_1 and A_2 are the number of nucleons of the ions in the two beam respectively [68].

Run	**Species**	**Energy** $[\sqrt{s}_{\rm NN}$(GeV)]	**Duration** (in weeks)	**Luminosity** (nb^{-1})	**ions/bunch** $[10^9]$
	Au+Au	200	10.9	10.3	1.1
	Au+Au	62.4	2.9	544	1.2
RUN 10	Au+Au	39	1.8	206	1.3
FY2010	Au+Au	11.5	4.6	4.23	1.1
	Au+Au	7.7	1.4	7.8	0.5
	Au+Au	200	6.4	9.79	1.30
RUN 11	Au+Au	19.6	1.4	10.3	0.9
FY 2011	Au+Au	27	1.1	63.1	1.45

Table 2.1: RHIC operating modes for Beam Energy Scan Program, Fiscal years (FY) start on October 1^{st} [68]. The duration of the physics runs are listed in 4th column. Luminosity is the integrated luminosity on the running time. The number of bunches during above runs are 111 and the ions per bunch is listed in column 6th of the table.

Chapter 3

STAR experiment at RHIC

[*Experimenters are the shock troops of science.* —Max Planck]

STAR collaboration is composed of 58 institutions from 12 countries, with a total of 586 collaborators. It includs students, university faculty and staff, national laboratory staff, and engineers.

3.1 The STAR detector system

The Solenoidal Tracker at RHIC (STAR) detector aims to study the strongly interacting matter — known as the Quark Gluon Plasma — produced during the heavy-ion collisions. STAR is able to measure many observables simultaneously to study signatures of a possible QGP phase transition and to understand the space-time evolution of the collision process in ultra-relativistic heavy ion collisions. The large uniform acceptance of STAR provides a suitable environment for event-by-event characterizations of heavy ion collisions and other hadronic physics study.

The STAR detector system is specialized in the tracking of thousands of particles produced by each ion collision at RHIC. The STAR magnet weighing 1,200 tons provides suitable magnetic environment for the bending of highly energetic charged particles during collisions. Below we give details of the detectors in the experiment.

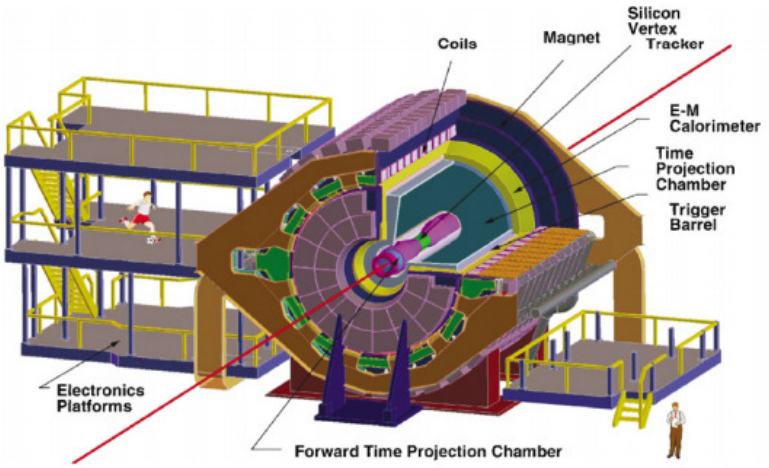

Figure 3.1: STAR detector system front veiw.

3.2 STAR Detector overview

A picture of the STAR detector system and a sketch of detector components are shown in Fig. 3.1 and 3.2, respectively.

Time Projection Chamber

When a charged particle traverses the TPC volume, it ionizes gas atoms every few tenths of a millimeter along its path and leaves behind a cluster of electrons. The

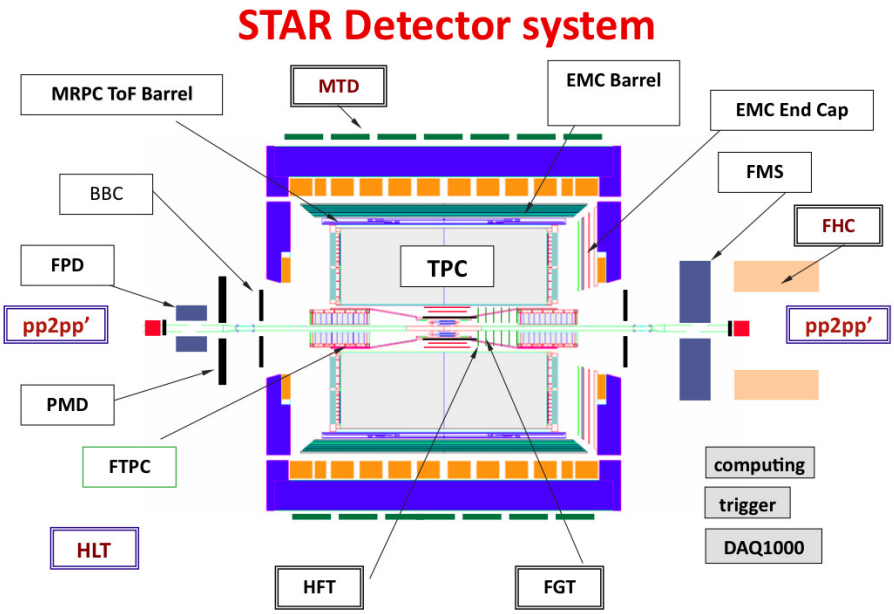

Figure 3.2: STAR detector system layout.

electron clusters then drift to the anode plane under the influence of an externally applied electric field where their time of arrival and location is recorded. In the STAR TPC, the electric field is provided by the outer field cage (OFC), the inner field cage (IFC), and the high voltage central membrane (CM). The purpose of the OFC and IFC are to provide a nearly perfect electric field in which the electrons drift to the anode plane. It avoids the distortions of the recorded tracks. The OFC and the IFC also serve to define the active gas volume and are designed to contain the TPC gas and prevent it from being contaminated with outside air. The central membrane is located in the middle of the TPC and is held at high voltage. The anode and pad planes are organized into sectors on each end of the TPC and the pads are held at ground potential. The OFC and IFC include a series of gradient rings that divide the space between the central membrane and the anode planes.

The total distance from the CM to either anode plane is slightly greater than 2 meters. There is approximately one ring per centimeter and the rings are biased by a chain of resistors that connect to the CM, the anode plane ground, and each of the gradient rings in-between. The rings are separated by two mega-ohm resistors and there are 182 rings and 183 resistors in each chain.

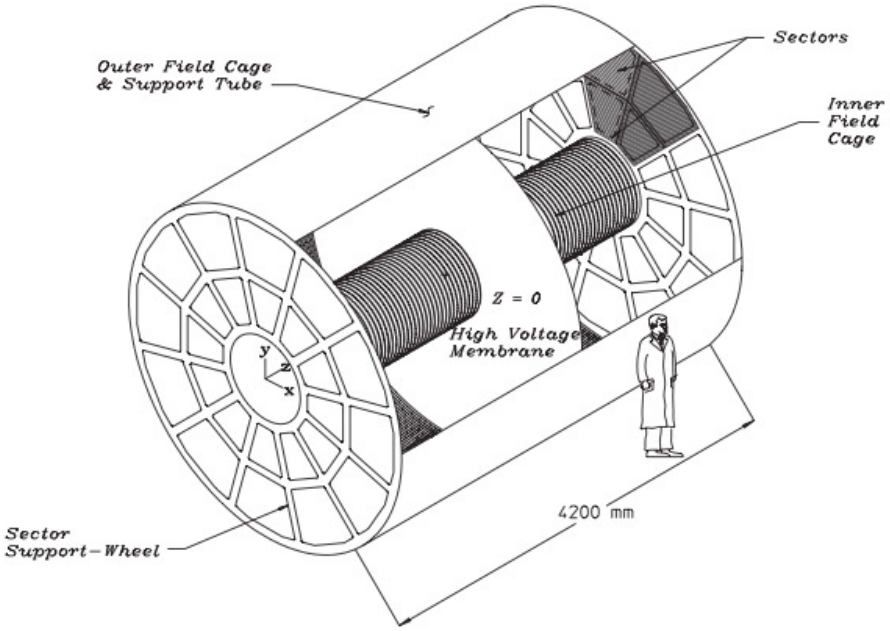

Figure 3.3: The STAR TPC surrounds a beam-beam interaction region at RHIC. The collisions take place near the center of the TPC.

Structure of the Field Cages :- The field cages are designed to be low mass and "thin" for particles to pass through them with very little energy loss but at the same time strong enough to be self supporting. So the field cages were built using two sheets of metal coated Kapton separated by a honeycomb of Nomex. The

whole assembly was rolled into a tube and the sheets of Kapton were epoxied to the honeycomb to form a strong sandwich of material. The Kapton in the outer field cage (OFC) is laminated with a 35 micron layer of copper and the metal layer is etched into stripes so that, after rolling the tube, the stripes become rings around the tube. The inner field cage (IFC) is similar to the outer field cage, but the Kapton is laminated with a thinner layer of Aluminum (9 micron) and the Nomex layer is thicker (1.27 cm).

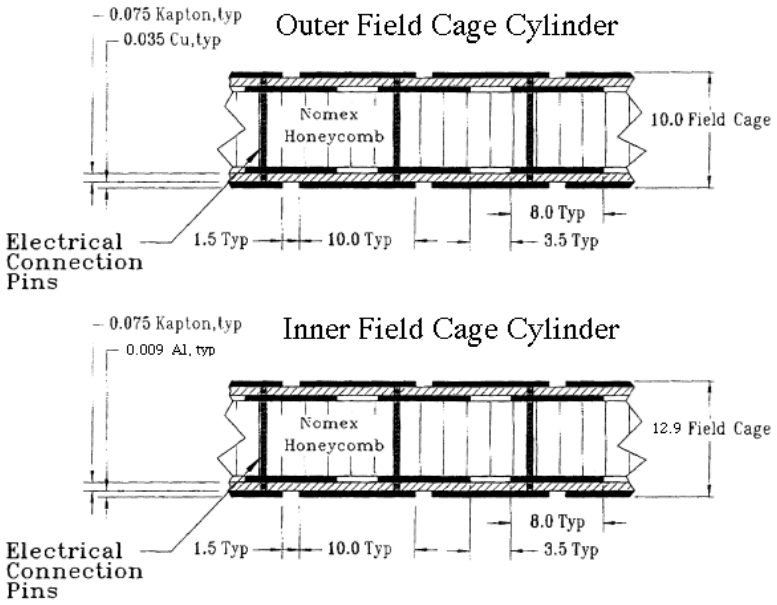

Figure 3.4: A cutaway view of the Outer and Inner field cage (OFC and IFC, respectively) showing the construction and composition of the cylinder wall. Dimensions (Typ) are in mm.

Choosing the Gas:- Gas purity, multiple scattering, drift velocity, cost, and safety are few of the important issues while choosing appropriate gas mixture for the TPC volume. STAR has chosen to run with gas mixtures: Ar (90%)-Methane (10%) — known as P10 gas. The noble gas component has a very low affinity for free

electrons while the organic gases quench the propagation of UV photons throughout the TPC volume. The TPC operates with P10 gas and a drift field of about 145 V/cm.

Performance of the TPC:- The acceptance of the STAR TPC covers 1.8 units of pseudorapidity through the full azimuth. The transverse momentum, p_T , of a track is determined by fitting a circle through the x, y coordinates of the vertex and the points along the track. The total momentum is calculated using this radius of curvature and the angle that the track makes with respect to the z axis of the TPC. The charge state of the particle is identified by using the Helix of the reconstructed charged tracks in TPC. The identification of the charged particles like, $\pi^+(\pi^-)$, $K^+(K^-)$ and $p(\bar{p})$, is done by measuring their ionization energy loss (dE/dx) in the TPC gas. The large range of charged particles can be identified by TPC ranging from $0.15 < p_T < 30$ GeV/c. The relative momentum resolution, $\Delta p/p$, for pions is about 3% at $p_T = 1$ GeV/c. For the detection of weakly-decaying particles, like Λ and Ξ, the invariant mass technique and topological reconstruction methods are used. For a minimum ionizing particle, MIP, the dE/dx resolution in the STAR TPC is 6-8% for a track with the maximum of 45 sampled dE/dx points. A maximum of 45 hit points per track can be reconstructed within the TPC radius limits of $0.5 < \mathrm{r} < 2$ m.

The electron drift velocity in P10 is about 5.45 cm/μs at 130 V/cm electric filed. Details of the charged particle detection efficiency will be discussed later in the thesis.

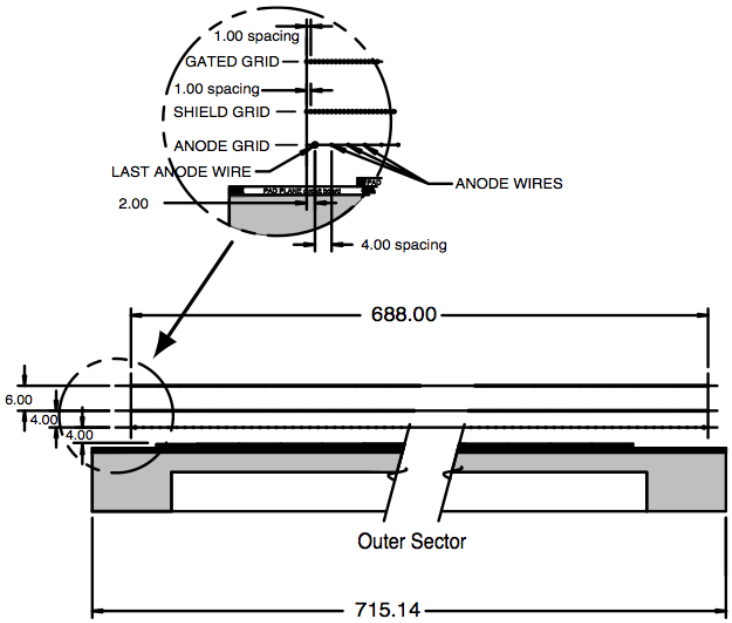

Figure 3.5: A cutaway view of an outer sub-sector pad plane. The cut is taken along a radial line from the center of the TPC to the outer field cage so the center of the detector is towards the right hand side of the figure. The figures show the spacing of the anode wires relative to the pad plane, the ground shield grid, and the gated grid. The bubble diagram shows additional detail about the wire spacing. The inner sub-sector pad plane has the same layout except the spacing around the anode plane is 2 mm instead of the 4 mm shown here. All dimensions are in millimeters.

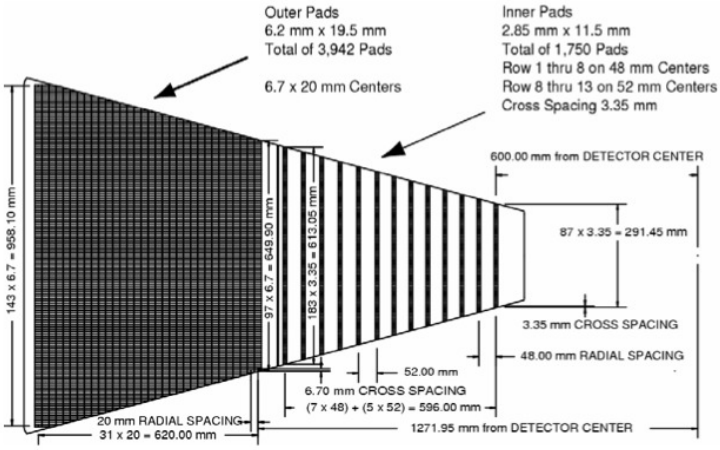

Figure 3.6: The anode pad plane with one full sector shown. The inner sub-sector is on the right and it has small pads arranged in widely spaced rows. The outer sub-sector is on the left and it is densely packed with larger pads.

Time Of Flight, TOF

To enrich the identification of the charged particles over wider range of momentum, TOF detector system was introduced. It consists of two detectors subsystems, one called the pVPD, the Pseudo Vertex Position Detector, (the start detector) and the other called the TOFp, Time-Of-Flight Patch, tray (the stop detector). Each of these detector subsystems is based on conventional scintillator or phototube technology. It includes custom high-performance front end electronics and common digitization in CAMAC. The Fig. 3.6 shows the diagrammatic representation of the STAR TOF subsystems in association with TPC and beam pipe. The time resolution of the TOF is about 100ps. The time interval, Δt, is estimated from the reconstructed tracks in the STAR TPC by the track extrapolation to the TOFp. Hence, the STAR TPC provides the momentum, p, and total path length, s, using STAR geometry that helps estimate the inverse velocity, $1/\beta$ for the TOF matched track

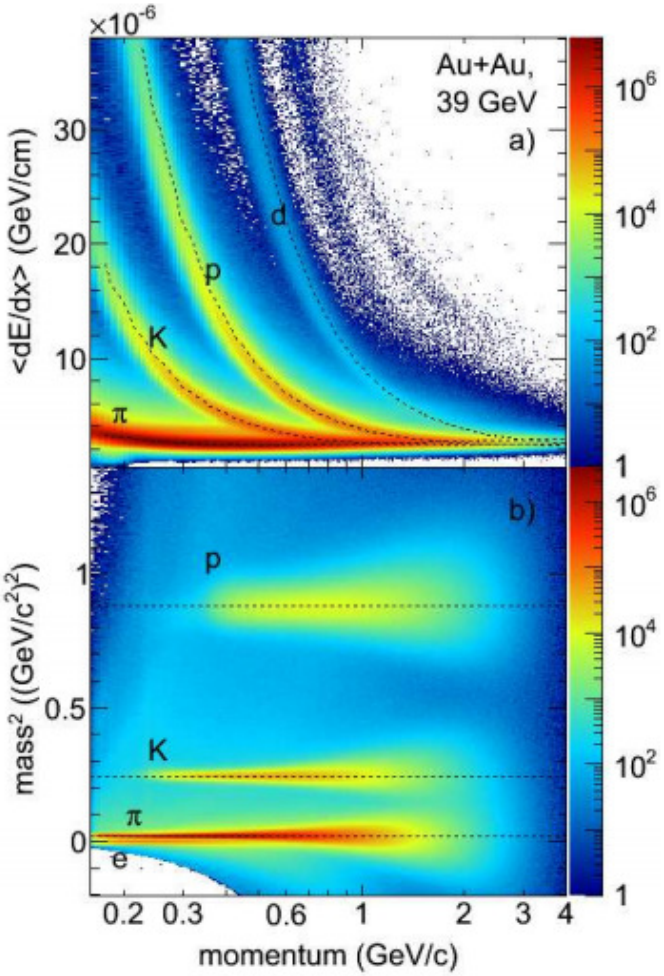

Figure 3.7: The Particle identification by dE/dx vs momentum of particles using TPC (top panel) and together with TOF detector (bottom panel) by square of mass vs momentum of the particles in STAR detector system [47].

by $1/\beta = c\Delta t/s$. where c is the speed of the light. The inverse velocity and momentum for a given particles are used for the estimation of the associated mass, M, as $M = p\sqrt{(1/\beta)^2 - 1}$. It improves the PID identification capabilities up-to $\sim 0.3 < p < 1.7 - 1.9$ GeV/c for direct $\pi/K/p$, whereas for $(\pi + K)$/p the upper range of momentum is extended up-to 2.8-3.0 GeV/c. The details about the STAR TOF detector system can be found in Ref. [48].

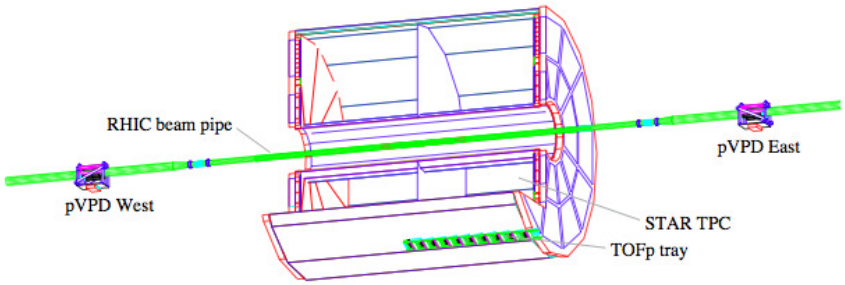

Figure 3.8: The schematic diagram for the STAR TOF subsystems with the association of STAR TPC and beam pipes.

Barrel Electromagnetic Calorimeter, BEMC

In STAR detector system, BEMC plays a significant role for the detection of photons, electrons, π^0 and η mesons with large STAR acceptance both for the pp and AuAu collisions. It also contributes to trigger system in STAR, capable of triggering on high-p_T physics. It is situated inside the STAR solenoidal magnet coil and covers $|\eta| \leq 1.0$ in full azimuth. The details of the BEMC can be found in Ref. [45].

Endcap Electromagnetic Calorimeter, EEMC

Supplementing the BEMC in the forward region $1 < |\eta| \leq 2$, the EEMC covers the full azimuth of STAR detector system. Like BEMC, it plays an important role in the detection of the photon, electromagnetic decaying mesons like, π^0 and η in the energy region 10-40 GeV. It also helps in high p_T triggering system in STAR and discriminating pre-shower and post-shower layers intended to discriminate hadrons from electrons. The details of the EEMC can be found in Ref.[46].

Photon Multiplicity Detector, PMD

The PMD is one of the gas ionization detector with high granularity within the pseudorapidity range 2.3 to 3.5 in full azimuth, located at 550 cm from the vertex and outside the STAR magnet. It is designed to measure the photon multiplicity at forward region of the STAR detector system. It comprises two plane — charged particle veto and pre-shower plane. These two planes are used to discriminate charged hadrons from the photon cluster produced during shower formation in the lead plane placed in between these two planes. Each plane consists of 24 super-module. Each super-module consists of 4 to 9 unit module. A honeycomb of 24×24 cells forms a unit module. This is a rhombus of side approx. 254 mm having identical boundaries on all the four sides. Cell walls at the boundary are kept half as thick as those inside so that adjacent unit modules join seamlessly.

The detail about the PMD can be found in Ref. [49].

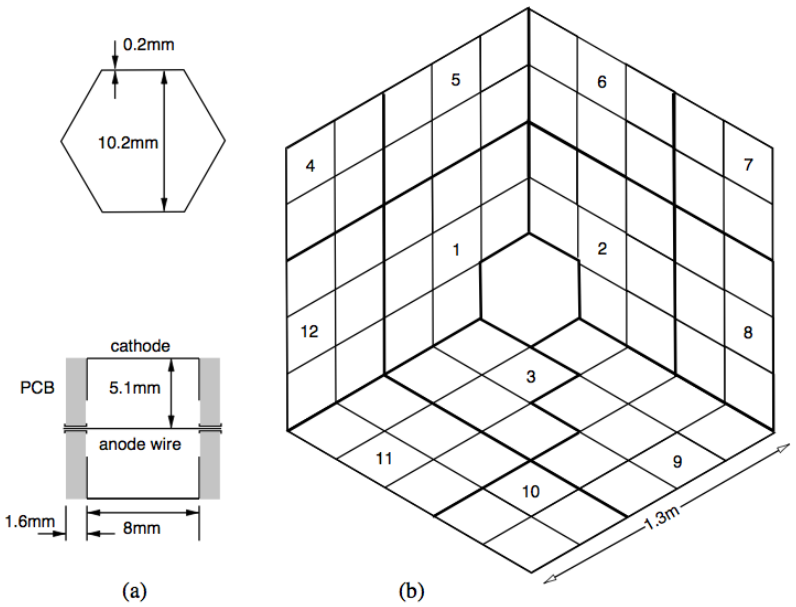

Figure 3.9: (a) Cross-sectional view of unit cell and the cathode extension in it and (b) layout of the STAR PMD. Thick lines indicate super-module boundaries. There are 12 super-modules each in the pre-shower plane and the veto plane. Divisions within a super-module denote unit modules [49].

3.3 STAR Trigger and DAQ system

The STAR trigger system plays a significant role for the event selection at the RHIC interaction point with beam crossing rate ∼10 MHz. In the STAR detector system, for Run 10 (year 2010) and Run 11 (year 11), the fast detectors like, ZDC, EMC, BBC, VPD, etc., were used to start the amplification-digitization-acquisition cycle for the slower detector systems. The slower detector systems like, TPC, FTPC, TOF, PMD, are operated at the rates of ∼100 Hz. These slow detectors are fed with the Trigger Control Unit (TCU) which is then connected with the Data Acquisition (DAQ) system through various level like, Level-0/-1/-2/-3 triggering system. The jobs done by these level triggers are: (i) selecting central and peripheral Au+Au events based upon multiplicity of that event, (ii) rejecting beam-gas events comparing vertex position from the interaction point and finally (iii) event selection based upon the online reconstruction of tracks of each particles. The details about the STAR trigger system can be found in the Ref. [50, 51]. The STAR DAQ system is controlled by RHIC Computing Facility (RCF). The RCF plays the important role for the storage of the STAR data at the raw level by using a High Processing Storage System (HPSS). Details about the STAR DAQ system is discussed in Ref. [52].

Chapter 4

Moments of the multiplicity distributions

The main goal of the heavy-ion-collisions at ultra-relativistic energies is to study the QGP matter. The event-by-event fluctuation of the multiplicity, transverse momentum, particles ratios, temperature, etc. are some of the observables which help in exploring QGP as also in the search for the Critical Point in the QCD phase diagram. To probe to the QCD Critical Point, various observables have been proposed. Among them transverse momentum, p_T, multiplicity fluctuation, particle ratio fluctuation [54, 55, 56], etc. have been studied by the experiments, CERES, NA49, STAR.

Lattice and other QCD based models have proposed higher moments of conserved charges (such as net-charge, net-baryon and net-strangeness) to be novel probe in the search the QCD critical point in phase diagram. In the next section, the details about the higher moments have been discussed.

4.1 Higher moments of event-by-event multiplicity distribution

4.1.1 Introduction to higher moments

In the mathematical statistics, a random variables X are characterized by certain probability density functions (*pdf*), $f(x)$. All characteristic properties of these *pdf* are conveyed in terms of the expectation values, E[g(X)], as follow

$$E[g(X)] = \int g(x)f(x)dx \tag{4.1}$$

$$\tag{4.2}$$

where g(x) represents any function of the random variable X and integration is over all values of X provided the function is integrable under certain limit. The n^{th} order moment of the *pdf* , which is defined as

$$\mu_n = E[X^n] = \int x^n f(x)dx \tag{4.3}$$

The 1^{st} order moment is commonly known as mean, μ_1 or only μ. The n^{th} order central moment is defined as

$$\nu_n = E[(X-\mu)^n] = \int (x-\mu)^n f(x)dx \tag{4.4}$$

Here the term central is due to the integration of function g(X) around its mean

value μ. This implies 1st order central moment is simply zero as $\int (x-\mu)f(x)dx = \int xf(x)dx - \mu \int f(x)dx = \mu - (\mu \times 1) = 0$. The 2^{nd}, 3^{rd} and 4^{th} order central moments are defined as,

$$\nu_2 = \int (x-\mu)^2 f(x)dx, \tag{4.5}$$

$$\nu_3 = \int (x-\mu)^3 f(x)dx, \tag{4.6}$$

$$\nu_4 = \int (x-\mu)^4 f(x)dx \tag{4.7}$$

The 2^{nd} order central moments is known as variance, σ^2. it is expressed as follows

$$\sigma^2 = \nu_2 = \mu_2 - \mu^2. \tag{4.8}$$

Similarly, 3^{rd} central moments can be derived in terms of nth order moments as follows,

$$\begin{aligned} \nu_3 &= E[(X-\mu)^3], \\ &= E[X^3 - 3\mu X^2 + 3\mu^2 X - \mu^3], \\ &= \mu_3 - 3\mu\mu_2 + 3\mu^3 - \mu^3, \\ &= \mu_3 - 3\mu\mu_2 + 2\mu^3 \end{aligned} \tag{4.9}$$

The general expression of the nth order central moments can be expressed in terms of nth order moments as follows

$$\begin{aligned}\nu_k &= \mu_k - \binom{k}{1}\mu_{k-1}\mu_1 + ... + (-1)^r\binom{k}{r}\mu_{k-r}\mu_1^r \\ &\quad + ... + (-1)^{k-1}(\binom{k}{k-1} - 1)\mu_1^k \end{aligned} \tag{4.10}$$

Now, these central moments play a significant role in understanding the shape of a *pdf*. The skewness, S, of a *pdf* is defined as,

$$S = \frac{\nu_3}{\nu_2^{3/2}} = \frac{\nu_3}{\sigma^{3/2}}. \tag{4.11}$$

The positive and negative values of the skewness qualitatively show the distribution of the random variable X skewed towards right and left side of the mean of the distribution as shown in the Fig. 4.1. More generally skewness represents the asymmetry of the distribution. Similarly, the kurtosis, κ, is associated with the 4^{th} and 2^{nd} order central moments of a *pdf* as follows,

$$\kappa = \frac{\nu_4}{\nu_2^2} = \frac{\nu_4}{\sigma^4}. \tag{4.12}$$

The kurtosis of the normal distribution is equal to 3. So to normalize the kurtosis with respect to normal or Gaussian distribution, 3 is subtracted and final expression for the kurtosis is used as

$$\kappa = \frac{\nu_4}{\sigma^4} - 3. \tag{4.13}$$

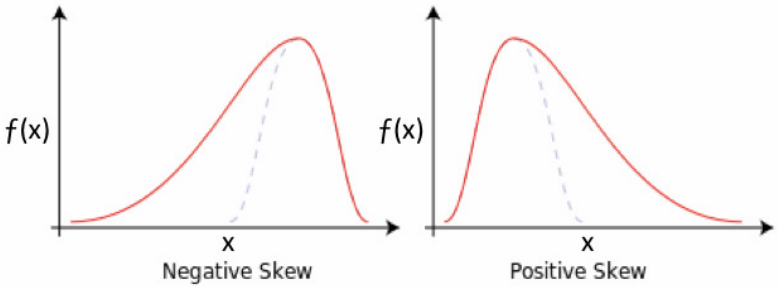

Figure 4.1: Skewness of the distributions.

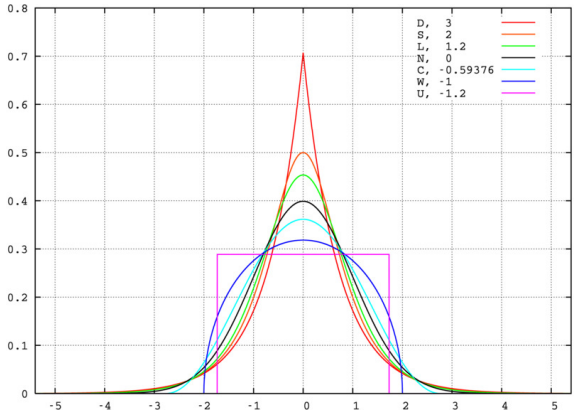

Figure 4.2: Kurtosis of Various distributions.

The kurtosis represents the peakedness and tailed-ness of the distribution as shown in the Fig. 4.2. In this figure, each distribution represents different kurtosis values. Similarly, higher order moments can be constructed like 5^{th}, 6^{th} order, etc. which carry more information about the *pdf*.

4.1.2 Moments generating function

"*A generating function is a clothesline on which we hang up a sequence of numbers for display.*" —Herbert Wilf

The moments can also be hung up through its generating function known as, *Moment generating functions*, *mgf* . For a random variable X, and a real dummy number t, the *mgf* can be defined as

$$M_X(t) = E[e^{tX}] = \int e^{tx} f(x)\,dx. \tag{4.14}$$

The necessary condition for the existence of the *mgf* : $\forall\ t \longrightarrow X$ is bound and $\exists\ t = 0 : M(0) = E(1) = 1$. Expanding e^{tx} in the above equation

$$\begin{aligned} E[e^{tX}] &= E[1 + tX + \frac{t^2X^2}{2!} + ...] \\ &= 1 + E[X]t + E[X^2]\frac{t^2X^2}{2!} + E[X^3]\frac{t^3X^3}{3!} + ... \end{aligned} \tag{4.15}$$

The various moments can be constructed at using dummy variable, $t = 0$ by

$$\mu_n = E[X^n] = \frac{d^n M_X(t)}{dt^n}|_{t=0} \tag{4.16}$$

The central moments can also be constructed by $X \longrightarrow Y$, where $Y = X - \mu$. For

example,

$$E[Y^n] = E[(X-\mu)^n] = (\frac{d^n}{dt^n}[e^{-\mu t}M_X(t)])_{t=0}. \tag{4.17}$$

Relation between Moments and Cumulants

The quantities cumulants of a *pdf* can be expressed in terms of the moments by invoking *cumulant generating function, cgf.* The *cgf* , C_X for dummy variable t, is defined by

$$\begin{aligned} C_X(t) &= lnM_x(t) \\ &\equiv c_1 t + c_2\frac{t^2}{2!} + c_3\frac{t^3}{3!} + \cdots. \end{aligned} \tag{4.18}$$

Here like *mgf* , there is no constant term in *cgf* and c_n represents the nth order cumulants. The relation between cumulants and moments can be constructed as follows

$$\frac{dC_X(t)}{dt} = \frac{1}{M_X}\frac{dM_x(t)}{dt} \tag{4.19}$$

$$\begin{aligned} \Rightarrow M_X(t)\frac{dC_X(t)}{dt} &= \frac{dM_x(t)}{dt} \\ \Rightarrow (1+\mu_1 t+\mu_2\frac{t^2}{2!}+\mu_3\frac{t^3}{3!}+\cdots) & \\ \times (c_1+c_2 t+c_3\frac{t^2}{2!}+\cdots) & \\ = (\mu_1+\mu_2 t+\mu_3\frac{t^2}{2!}+\cdots). & \end{aligned} \tag{4.20}$$

Now, comparing coefficients of like powers of t from both sides, it can be found

$$\begin{aligned}
\mu_1 &= c_1, \\
\mu_2 &= c_2 + c_1\mu_1, \\
\mu_3 &= c_3 + 2c_2\mu_1 + c_1\mu_2, \\
\mu_4 &= c_4 + 3c_3\mu_1 + 3c_2\mu_2 + c_1\mu_3, \\
&\cdots \\
\mu_k &= c_k + \binom{k-1}{1}c_{k-1}\mu_1 + \cdots + \binom{k-1}{r}c_{k-r}\mu_r + c_1\mu_{k-1}. \quad (4.21)
\end{aligned}$$

Using above expressions, cumulants can also be expressed only in terms of moments as follows

$$\begin{aligned}
c_1 &= \mu_1, \\
c_2 &= \mu_2 - \mu_1^2 = \nu_2, \\
c_3 &= \mu_3 - 3\mu_2\mu_1 + 2\mu_1^3 = \nu_3, \\
c_4 &= \mu_4 - 4\mu_3\mu_1 + 12\mu_2\mu_1^2 - 3\mu_2^2 - 6\mu_1^4 = \nu_4 - 3\nu_2^2.
\end{aligned} \quad (4.22)$$

So, it can be easily understood that mean(M), standard deviation(σ), skewness(S) and kurtosis(κ) are related with cumulant as follows

$$\boxed{M = c_1, \qquad \sigma = c_2^{1/2}, \qquad S = \frac{c_3}{c_2^{3/2}}, \qquad \kappa = \frac{c_4}{c_2^2}} \quad (4.23)$$

These observables are mainly used in this thesis work.

Properties of the cumulants

1. Additivity:-

   if $X_1, X_2, ..., X(n)$ are independent random variable, and $C_{X_i}(t)$ for i=1, 2, 3,...,n is the *cgf* for X_i the *cgf* of $S_n = c_1X_1 + c_2X_2 + ... + c_nX_n$ is given by

$$C_{S_n}(t) = \sum_i C_{X_i}(c_i t). \tag{4.24}$$

2. Shifting of origin:-

   For $X \to X + a, \qquad c_1 \to c_1 + a.$

   Where all other higher cumulant remains invariant.

3. Changing scale:-

   For $X \to aX, \qquad c_r \to a^r c_r$

4.1.3 Relation between moments and thermodynamic quantities

Thermodynamical quantity, like pressure, entropy, etc., can be derived from the partition function, Z of the system and pressure, P, can be expressed, in the thermodynamic limit, as follows

$$P(T, \mu_B, \mu_Q, \mu_S) = \lim_{V \to \infty} \frac{T}{V}\, lnZ(T, V, \mu_B, \mu_Q, \mu_S) \tag{4.25}$$

Here T, V are the temperature and volume of the system. The baryonic, charge and strangeness chemical potential can be represented by μ_B, μ_Q and μ_S respectively. The nth derivatives of thermodynamic susceptibilities of conserved quantities q, can

be defined as

$$\chi_q^{(n)} = \frac{\partial^n[p/T^4]}{\partial(\mu_q/T)^n}, \qquad q = B, Q, S \tag{4.26}$$

The conserved charge fluctuation can be expressed as $\delta N_q = N_q - \langle N_q \rangle$. The mean and variance of the conserved charge distribution can be expressed in terms of the derivatives of thermodynamic susceptibilities as follows

$$M_q \equiv \langle N_q \rangle = VT^3\chi_q^{(1)}, \tag{4.27}$$

$$\sigma_q^2 \equiv \langle (\delta N_q)^2 \rangle = VT^3\chi_q^{(2)}, \tag{4.28}$$

$$\tag{4.29}$$

The skewness and kurtosis can be expressed in terms of the 3^{rd} and 4^{th} order thermodynamic susceptibilities as follows

$$S_q \equiv \frac{\langle (\delta N_q)^3 \rangle}{\sigma_q^3}, \tag{4.30}$$

$$\kappa_q \equiv \frac{\langle (\delta N_q)^4 \rangle}{\sigma_q^4} - 3, \tag{4.31}$$

where

$$\langle (\delta N_q)^3 \rangle = VT^3\chi_q^{(3)}, \tag{4.32}$$

$$\langle (\delta N_q)^4 \rangle - 3\langle (\delta N_q)^2 \rangle^2 = VT^3\chi_q^{(3)}, \tag{4.33}$$

Similarly even higher derivatives of susceptibilities, $\chi_q^{(6)}, \chi_q^{(8)}$, etc., are related with higher order of the moments,$\langle (\delta N_q)^6 \rangle$ and $\langle (\delta N_q)^8 \rangle$ etc., of the conserved charge dis-

tribution. Various suitable moments products are constructed to cancel the volume term for the above expressions.

$$\frac{\sigma_q^2}{M_q} = \frac{\chi_q^{(2)}}{\chi_q^{(1)}}, \quad S_q\sigma_q^2 = \frac{\chi_q^{(3)}}{\chi_q^{(2)}}, \qquad \kappa_q\sigma_q^2 = \frac{\chi_q^{(4)}}{\chi_q^{(2)}}, \tag{4.34}$$

Chapter 5

Baseline for higher moments of net-charge multiplicity distribution

To understand the experimental signature of the QCD Critical Point, one has to understand the sources of background fluctuation originating from different sources like, statistical fluctuation, fluctuations related to non-critical phenomena, etc. To understand statistical fluctuation, Poisson and Negative Binomial distribution are assumed for positive and negative charged multiplicity distribution. Background fluctuations in the heavy-ion-collision like, jet-interaction, jet-quenching, baryon stoping, hadronic re-scattering, resonance production and thermal equilibrium assumption have been studied by using various event generators like HIJING, UrQMD and THERMINATOR-2 . These event generators are based on non-critical phenomena, and thus provide suitable baseline for the critical point search in heavy-ion-collision. The details about these models have been discussed in the following sections.

5.1 Hadron Resonance Gas Model

In this model, Ref. [58], the system is assumed to be consisting of all the hadrons and resonance gas with interactions among themselves at the thermal and chemical equilibrium. Figure 5.1 shows the ratio of susceptibilities, $\chi_Q^{(4)}/\chi_Q^{(2)}$, $\chi_Q^{(3)}/\chi_Q^{(2)}$, and $\chi_Q^{(2)}/\chi_Q^{(1)}$ are plotted as a function of beam energy. The corresponding values for $\sqrt{s}_{\rm NN}$= 200, 62.4, 39, 11.5 and 7.7 GeV have been listed in Table 5.1. The HRG models predicts that $\frac{\sigma^2}{M}$= $\chi_Q^{(2)}/\chi_Q^{(1)}$ increases and $S\sigma$= $\chi_Q^{(3)}/\chi_Q^{(2)}$ decreases with increasing beam energy. The $\kappa\sigma^2$= $\chi_Q^{(4)}/\chi_Q^{(2)}$ shows no energy dependence at high energy and negligible energy dependence at low energy. The expression for the susceptibilities, for even n, of the net-conserved charge is expressed as

$$\chi_Q^{(n)} = \frac{1}{T^3V}(ln\ Z_{|Q|=1}\ (T,\mu_X) + 2^n\ ln\ Z_{|Q|=2}\ (T,\mu_X)). \tag{5.1}$$

Due to the contribution of the second term in the above expression, $\kappa\sigma^2$=$\chi_Q^{(4)}/\chi_Q^{(2)}$ shows above unity for the net-charge distribution. This is because of the contribution of double charged baryons, like Δ^{++}, in the net-charge distribution. This model sets the baseline for the QCD critical point search. Any deviation from this baseline may indicate the signature of the dynamical fluctuation at freeze-out transition. If the QCD critical point exist in the phase diagram and the hadronization happens at the freeze-out line, then higher moments of the conserved charge distribution could show large deviation from the HRG model prediction.

$\sqrt{s_{\rm NN}}$(GeV)	$\kappa\sigma^2$	$S\sigma$	$\frac{\sigma^2}{M}$
200	1.75	0.0309	0.6779e+02
62.4	1.76	0.0959	0.2197e+02
39	1.77	0.1483	0.1425e+02
11.5	1.85	0.3921	0.5394e+01
7.7	1.86	0.4948	0.4176e+01

Table 5.1: The HRG model predictions for $\kappa\sigma^2$, $S\sigma$, and $\frac{\sigma^2}{M}$ at different beam energy for the net-charge distributions.

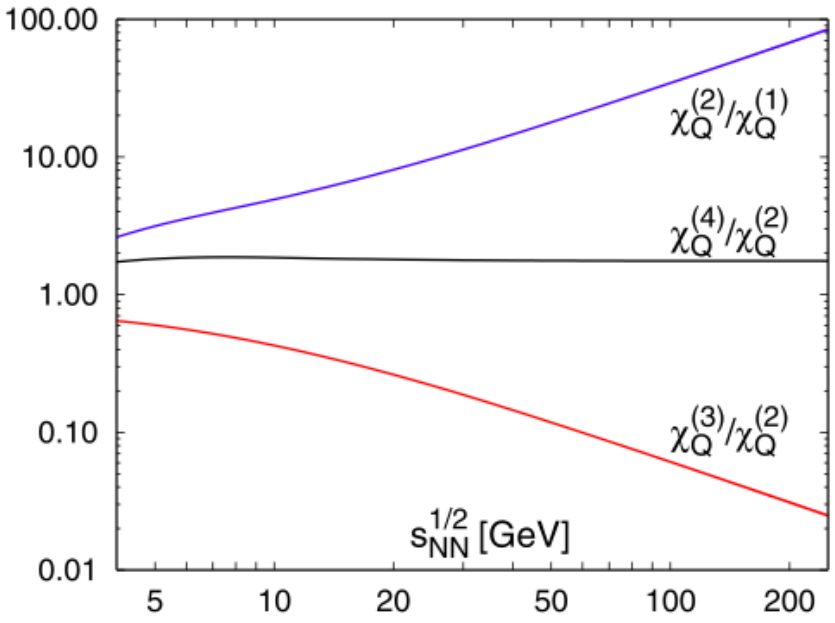

Figure 5.1: The HRG model predictions for $\kappa\sigma^2 = \chi_Q^{(4)}/\chi_Q^{(2)}$, $S\sigma = \chi_Q^{(3)}/\chi_Q^{(2)}$, and $\frac{\sigma^2}{M} = \chi_Q^{(2)}/\chi_Q^{(1)}$ at different beam energy for the net-charge distributions [58].

5.2 Results from event generators

To understand various physics processes which contribute to the moments of net–charge distributions, three different models have been used, such as, a QCD based model (HIJING [59]), a transport model (UrQMD [60]) and a thermal model, THERMINATOR-2 [61].

Figure 5.2(a) shows the net-charge distributions for top central (0-5 % of total cross section) collisions for four center-of-mass energies. It has been observed that the mean of the distributions is close to zero for high energy collisions and shifts towards positive values for lower energies. The distributions are seen to be wider for higher energy collisions compared to those of the lower energies. Figure 5.2(b) shows net-charge distributions for three different centrality classes for Au + Au collisions at $\sqrt{s}_{\rm NN}$= 39 GeV. It is seen that from peripheral to central collisions, the mean as well as the width of the distributions increase.

The results of the above event generators are compared to those of the Hadron Resonance Gas (HRG) [58] model predictions. Because of the absence of any critical phenomenon in these models, they set a baseline for the measurements at the Relativistic Heavy-Ion Collider (RHIC). The effect of particles species, resonance decay and all above models comparison have been discussed. Although our concern is mainly with moments of inclusive charged particles, it is important to obtain the effect of each particle species on the total net–charge distributions. These species mostly comprise of π^+, π^-, K^+, K^-, p, and $\bar{p}$, so the effect of net–pion, net–kaon and net–proton distributions on the net–charge distributions needs to be studied. At the generator level, the knowledge of the identity of each particle makes it possible to perform this study.

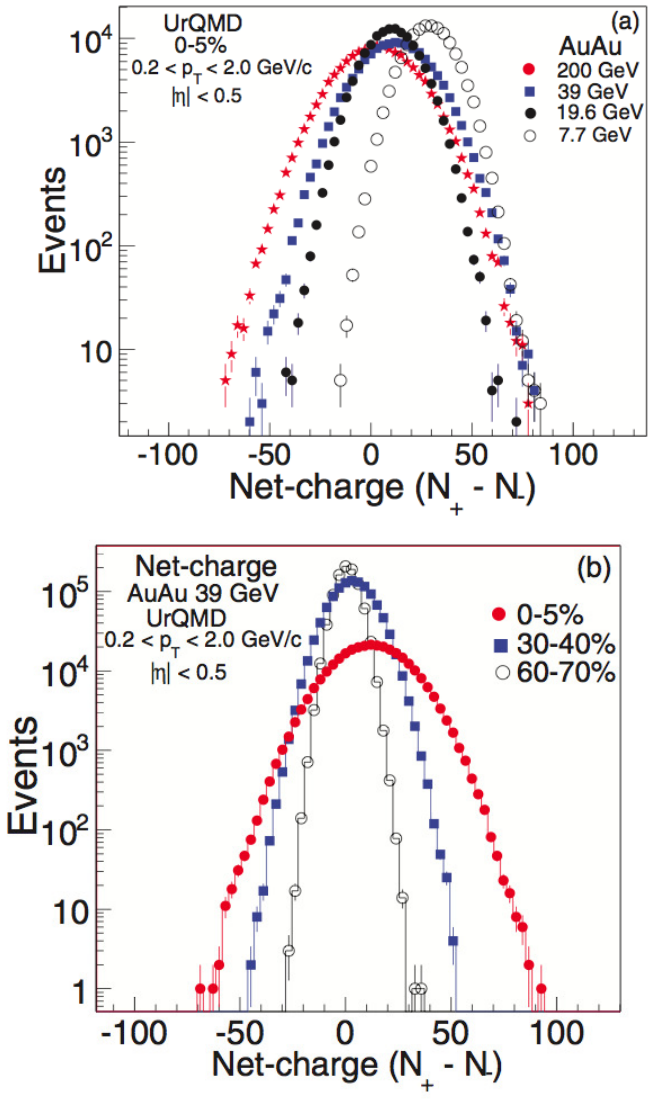

Figure 5.2: The net-charge distributions obtained from UrQMD for Au + Au collisions: (a) for central collisions at $\sqrt{s}_{\rm NN}$= 7.7, 19.6, 39, and 200 GeV, and (b) for three centralities (0-5%, 30-40%, and 60-70% of total cross section) at $\sqrt{s}_{\rm NN}$= 39 GeV [62].

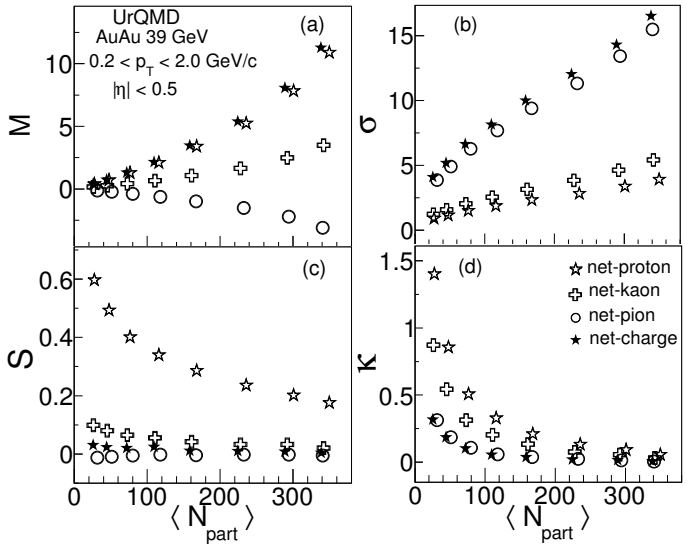

Figure 5.3: The (a) mean, (b) standard deviation, (c) skewness and (d) kurtosis for AuAu collisions at $\sqrt{s_{\rm NN}}$=39 GeV as a function centrality, expressed in terms of number of participating nucleons, for net–charge, net–pion, net–kaon and net-proton.

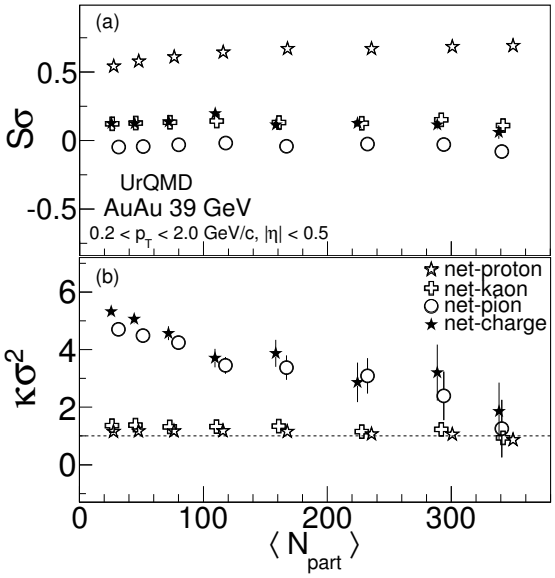

Figure 5.4: Products of moments, (a) $S\sigma$ and (b) $\kappa\sigma^2$, plotted with respect to the average number of participating nucleons, for net–charge, net–pion, net–kaon, and net–proton distributions.

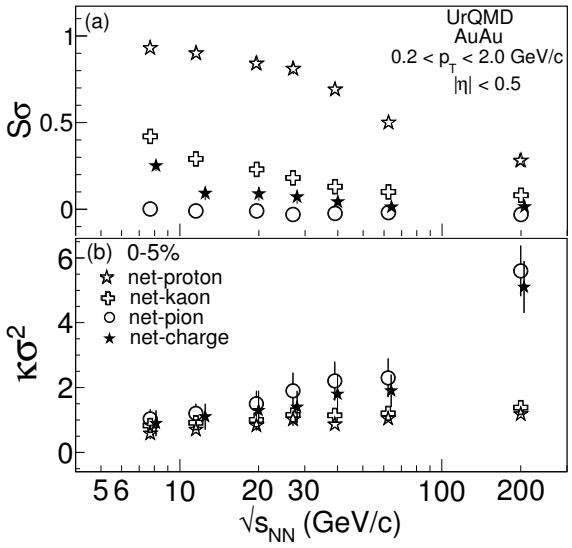

Figure 5.5: Products of moments, (a) $S\sigma$ and (b) $\kappa\sigma^2$, plotted with respect to AuAu collisions at different colliding energies. The moments are obtained from net–charge, net–pion, net–kaon, net–proton distributions.

The centrality dependence of the contributions from different particle species to the moments of net–charge distributions have been studied using UrQMD for AuAu collisions at $\sqrt{s_{\rm NN}}$=39 GeV. Inclusive charged particles as well as identified particles are selected in the same pseudo-rapidity ($|\eta| < 0.5$) window and same transverse momentum ranges ($0.2 < p_{\rm T} < 2.0$ GeV/c). Figure 5.4 shows the mean, standard deviation, skewness and kurtosis for net–charge, net–pion, net–proton and net–kaon distributions as a function of centrality. It is observed that the effect of particle species on the net–charge distributions are significant, and different species affect the moments in a different manner. The mean of the net–charge distributions are dominated by the effect of net–protons.

The mean of the net–pion distributions, on the other hand, are seen to decrease

going from peripheral to central collisions, whereas the trend is opposite for other three cases. The mean for net–pions shift to negative values for central collisions. The trend for mean of net-kaons is similar to those of net–charges. The widths of net–charge distributions are close to those of the net–pions. The widths of net–kaons and net–protons are close to each other, but the values are smaller than those of net–charges. The skewness of the net–charge distributions are close to those of the net–pions, whereas net–kaon values are not so far. But skewness for net–proton distributions are much larger compared to net–charges and has a significant centrality dependence. This may be because of the difference in the number of protons and anti-protons produced in different centrality classes at this energy. The kurtosis of net–charge distributions are close to those of net–pions, and smaller than those of the for net–kaons and net–protons.

As the products of moments (such as $S\sigma$ and $\kappa\sigma^2$) can directly be compared to lattice calculations, we have studied their centrality dependence in Fig 5.4 as a function of centrality for AuAu collisions at $\sqrt{s}_{\rm NN}$=39 GeV. It is observed that the $S\sigma$ values do not show centrality dependence at this energy. $S\sigma$ for net–charges are close to those of the net–kaons, whereas $S\sigma$ for net–pions are close to zero. These values for net–protons are much larger compared to net–charges. The $\kappa\sigma^2$ values for net–charges are close to those of the net-pions, and show strong centrality dependence. For net–kaons and net–protons, these values remain close to unity. The beam energy dependence of $S\sigma$ and $\kappa\sigma^2$ for top central AuAu collisions, obtained using UrQMD, have been presented in Fig. 5.5, where the upper and lower panels show the results for $S\sigma$ and $\kappa\sigma^2$, respectively. It is observed that $S\sigma$ for net–pions are close to zero at all energies, whereas a decreasing trend with increase of energy

is observed for all other cases. For net–charges, $S\sigma$ values get close to zero at higher energies. The energy dependence of net–proton is quite prominent with much larger $S\sigma$ values. The values of $\kappa\sigma^2$for net–charge are close to those of net–pions, and show increasing trend with increase of beam energy. For net–proton and net–kaon distributions, $\kappa\sigma^2$are close to unity at all energies.

Production of charged particles and net–charge distributions in proton-proton and heavy-ion collisions are affected by resonance decays. This can be studied by an event generator where one can track each of the particles in order to know its origin and history of the decay. THERMINATOR-2 offers such possibility for AuAu collisions at $\sqrt{s}_{\rm NN}$=200 GeV, where decays of resonances, such as, Ξ, Δ^{++}, ρ, ϕ and ω, and their anti-particles, can be turned on and off. Net–charge distributions have been computed with resonance decays turned on and off, which allows us to study the effects on the products of moments are studied. Figure 5.6 shows the results for $S\sigma$ and $\kappa\sigma^2$ as a function of centrality. $S\sigma$ shows no centrality dependence, and the values with resonance decay turned on are closer to zero compared to those without the decay. Values of $\kappa\sigma^2$without resonance decay are higher compared to those with the decay at all centralities. The reason for this could be the presence of double charged baryons, like Δ^{++}, which may affect the net–charge distributions, and enhance the higher order moments [64]. The net-charge distributions are sensitive to the particle production mechanisms. HIJING treats the heavy-ion collisions as a superposition of nucleon-nucleon collisions. It is well suited to study the effects of jets and mini-jets on produced particles. UrQMD is a hadronic transport model including strings. It has been used successfully to describe stopping power and hadronic

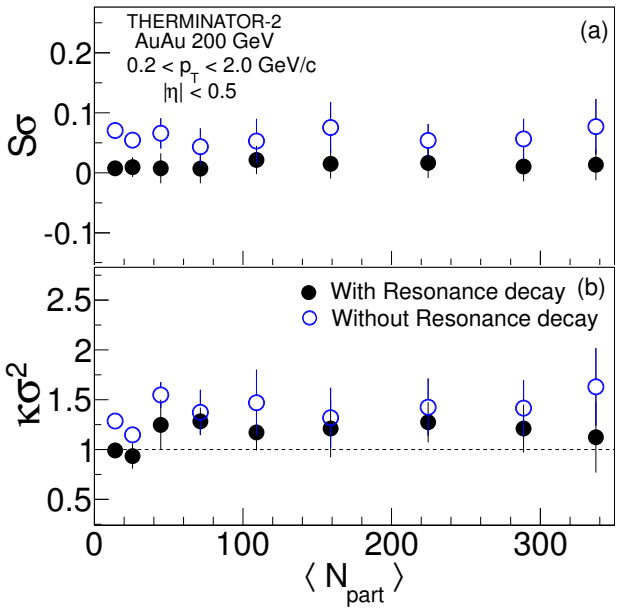

Figure 5.6: The product of the moments, (a) $S\sigma$ and (b) $\kappa\sigma^2$, are plotted with respect to average number of participating nucleons for two cases: with decay of all resonances and without resonance decays using THERMINATOR-2 event generator [61].

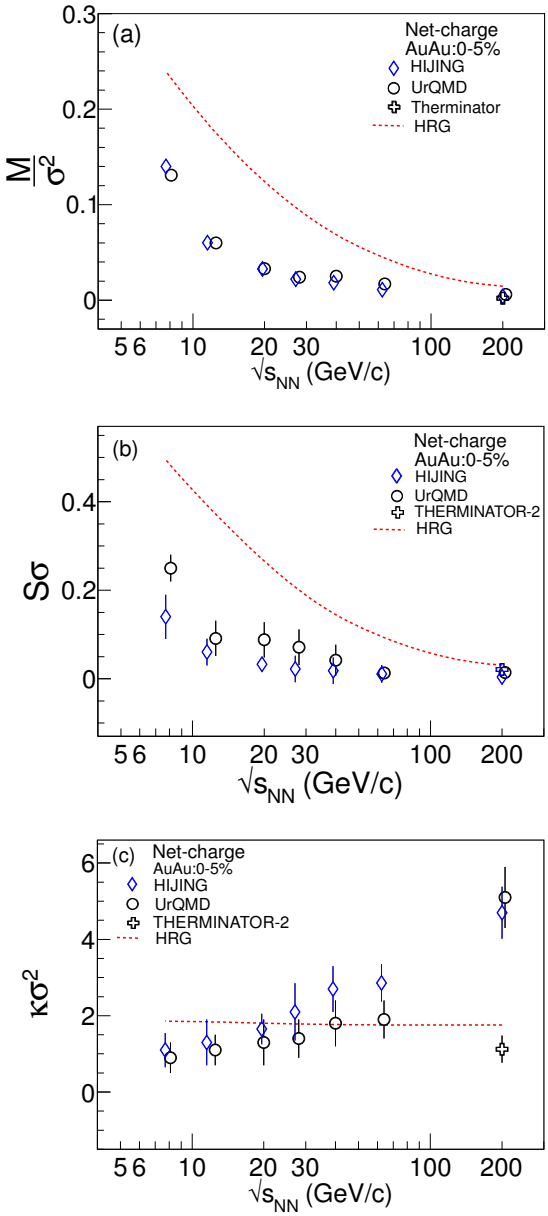

Figure 5.7: The collision energy dependence of the (a) M/σ^2, (b) $S\sigma$ and (c) $\kappa\sigma^2$ from net–charge distributions for top central (0-5%) collisions. The results are shown for HIJING, UrQMD, and THERMINATOR-2. The predictions from the HRG model for the net-charge are plotted in all cases.

re-scattering along with various hadronic resonances. The Lund string model is used for the particle production both in the HIJING and UrQMD models. On the other hand, THERMINATOR-2 gives a good description for the thermal model of particle production. The moments and their products for the net-charge distributions are analyzed for the three event generators for AuAu collisions at $\sqrt{s_{\rm NN}}$=200 GeV. Although the trends of all the distributions are similar, there are some differences in terms of magnitudes. The M and σ increase from peripheral to central collisions for all three models, whereas S and κ values decrease with increase in collision centrality. The values of M are lower in THERMINATOR-2 as compared to HIJING and UrQMD, but the standard deviations are similar in all three cases. The centrality dependence of S and κ for THERMINATOR-2 are also weaker as compared to the other two cases. Combinations of the moments, such as M/σ^2, $S\sigma$ and $\kappa\sigma^2$, have been constructed for central (0-5% of cross section) AuAu collisions at $\sqrt{s_{NN}}$=7.7 to 200 GeV using the three event generators. These are shown Fig. 5.7, along with the predictions from the HRG model calculations. It is observed that M/σ^2 and $S\sigma$ decreases with increasing colliding energy in all cases. The results from the three event generators are close together and HRG gives higher values. The values of $\kappa\sigma^2$from HRG model is seen remain constant close to 2, whereas variations are seen for the event generators. The consideration of double charged baryons in HRG model is probably responsible for $\kappa\sigma^2$to be close to 2. HIJING and UrQMD values are close to unity at low energy, after which these steadily increase as a function of energy. THERMINATOR-2 is available only at $\sqrt{s_{NN}}$ = 200 GeV, and the value is close to unity. At this energy, the models with thermal equilibrium (HRG and THERMINATOR-2) have produced lower values of $\kappa\sigma^2$compared to HIJING and

UrQMD.

5.3 Poisson Distribution

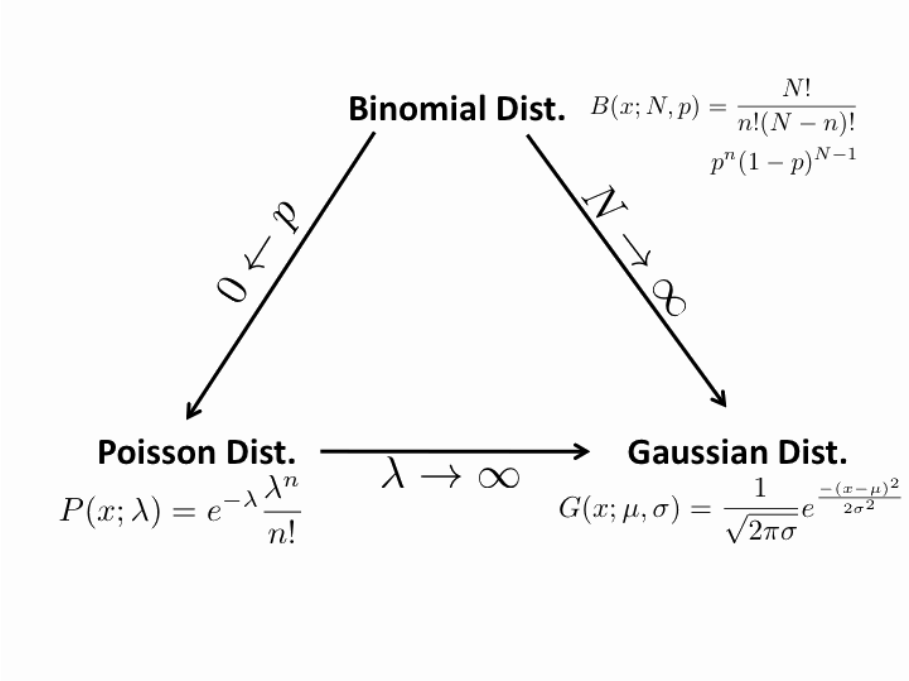

Figure 5.8: Diagrammatic representation of two limiting cases of Binomial distribution.

For the non-Critical baseline, the Poisson expectation is studied. Figure 5.8 shows the different limit of the three *pdf*, like Binomial, Poisson and Gaussian pdf. Poisson distribution is a limiting case of Binomial, when probability of success $p \to 0$. In the limit stopping parameter goes to infinity, $r \to \infty$, of Negative Binomial (NB) distribution and probability of success, p, goes to zero such that mean of the distribution constant, then NB distribution tend to Poisson Distribution. On the other hand, in the limit of mean of the Poisson distribution goes to infinite, Poisson distribution tend to Gaussian distribution.

In this approach, the positive and negative charged particles distributions are assumed to be independent Poisson distribution where it has been assumed that there is no dynamical correlation between the positive and negative charge particles. Hence, the net-charge distribution is taken as a Skellam distribution (resultant of the difference of two Poisson distributions) which serve as one of the baseline for this analysis. For the Skellam distribution,

$$M = N_+ - N_- \tag{5.2}$$

$$S\sigma = \frac{N_+ - N_-}{N_+ + N_-}, \tag{5.3}$$

$$\frac{\sigma^2}{M} = \frac{N_+ + N_-}{N_+ - N_-}, \tag{5.4}$$

$$\kappa\sigma^2 = 1 \tag{5.5}$$

Here N_+ and N_- are the means of the positive and negative charged particle distributions. The means of the positive and negative charged particle distributions have been estimated for each centrality bin. The results of Poisson expectations have been discussed in the result section in comparison with data and also discussed in [63]. Any deviation of data from these expectation could be due to the presence of dynamics of the system.

5.4 Negative Binomial Distribution expectation

Negative Binomial Distribution (NBD) can be expressed as,

$$NB(k; r, p) = \binom{k + r - 1}{k} p^r (1 - p)^k \tag{5.6}$$

Where p is the probability of success and k is the failure before the rth success. here r is also known as stopping parameter. As discussed above the limiting cases NBD or Binomial distribution are the Poisson and Gaussian distribution. It is worth noting that for the Gaussian distribution, the skewness and kurtosis are zero.

The NBD is valid in case of mean (μ) of the distribution is less than that of the variance, σ^2, $\mu < \sigma^2$. The probability of success is defined as $p = \frac{\mu}{\sigma^2}$. The cumulants of the NBD can be expressed in terms of the p and r as follows,

$$c_1 \sim \mu = \frac{r(1-p)}{p}, \tag{5.7}$$

$$c_2 \sim \sigma^2 = \frac{r(1-p)}{p^2}, \tag{5.8}$$

$$c_3 = \frac{r(p-1)(p-2)}{p^3}, \tag{5.9}$$

$$c_4 = \frac{-r(p-1)(6-6p+p^2)}{p^4} \tag{5.10}$$

In this approach, the positive and negative charged particles distributions are assumed to be independently NBD for a given centrality bin. Denoting cumulants of the positive charged distribution are $C^{+}_{n=1,2,3,4....}$, and similarly that for negatively charged particles are $C^{-}_{n=1,2,3,4....}$. Then cumulants of the net-charged distribution can be expressed as

$$C_n = C^{+}_n + (-1)^n C^{-}_n. \tag{5.11}$$

For the estimation of the NBD expectations, bin width correction have also been taken into account by calculating cumulants for the finer bin of the centrality. The

products of moments are constructed using above expressions and also using expression given in 4.23. The results from the data of AuAu collisions for beam energy scan in comparison with Poisson expectations also be discussed in results section in detail.

Chapter 6

Analysis details

For the study of higher moments of the net-charge distributions various system sizes as well as various beam energies have been analyzed at RHIC energies. It is necessary in the event-by-event fluctuation analysis to suppress background fluctuation originating from bad and outlier runs. For this a detailed has been performed. Besides this extensive study on centrality determination, finite bin width effect, central limit theorem, detector effect, efficiency correction for cumulants, and systematic as well as statistical error estimation have been discussed in the following sections.

6.1 Data sets and Track selection

The RHIC beam energy scan data for Au+Au collisions at 39, 27, 19.6, 11.5 and, 7.7 GeV along with 200 and 62.4 GeV have been analyzed. For the smaller colliding system, Cu+Cu collisions at 200 and 62.4 GeV and p+p collisions at 200 GeV have also been studied. In the table 6.1, the data set used for the net-charge higher moments analysis have been listed with the colliding system, beam energies, data

production name, trigger name, and trigger Id. The minimum bias events have been analyzed by using minimum bias trigger Id.

Table 6.1: The RHIC data set for various systems such as Au+Au, Cu+Cu and p+p collisions at different beam energies. The STAR production, Trigger name and Trigger Id are listed. The listed Trigger Id are minimum bias.

	$\sqrt{s}_{NN}$ (GeV)	**Production**	**Trigger Name**	**Trigger Id**
AuAu	200	AuAu_200Production_2011	P11id	350043
	62.4	AuAu62_Production	P10id	270021,270011, 270001
	39	AuAu39_Production	P10ik	280001
	27	AuAu27_Production_2011	P11id	360001
	19.6	AuAu19_Production	P11ik	340001,340011, 340021
	11.5	AuAu11_Production	P10ih	310014,310004
	7.7	AuAu7_Production	P10ih	290004,290001
CuCu	200	cuProductionMinBias	P07ic	66007
	62.4	cu62ProductionMinBias	P07ic	76007,76001
pp	200	pp2pp Production2009	P10ic	7,250107

For the analysis of the above data sets, off-line cuts are used during analysis. Along the longitudinal direction of the beam pipe, V_z, the events are selected within $\pm$30 cm from the center of the TPC detector. This ensures uniform acceptance. In addition, 2.0 cm radius in the transverse plane of the beam are used. The additional $|VpdV_z - V_z| < 4$ cm is used for AuAu collisions at 200, 62.4, and 39 GeV. All these cuts are shown in Fig 6.1-6.3 for AuAu collisions at 39 GeV. The extensive run quality assurance has been performed based on average distance of closest approach (DCA), p_T , η, and ϕ on the track variables and similarly on average reference multiplicity (Refmult), number of primary tracks for event variables. The outlier run rejection has been done based on appropriate σ of the above average variables.

In Fig. 6.4, the average value of Refmult and ϕ for various Runs (Run index assigned with Run numbers) are plotted for AuAu collisions for 200 GeV. The pile up events have been removed by taking correlation between TPC tracks (Refmult) and number of ToF matched tracks as shown in the Fig. 6.5 and 6.6. Here a line is drawn to separate well correlated and piled up events in a data sample. Similar procedure was followed for all energies. In Fig. 6.7, the correlation between positive charged particles and negative charged particles with respective to Refmult2 are show after removing pile-up events. The charged particles are bent due to the presence of 5

Table 6.2: Events cuts used for different data sets. The Vertex-z, Vertex-r, VpdVz cuts based on Vertex-z, and total no. of events after using these cuts have been listed for different systems and different colliding beam energies.

	$\sqrt{s}_{NN}$ (GeV)	$\|V_z\|$ (cm)	$\|V_r\|$ (cm)	$\|VpdVz - V_z\|$ (cm)	**Events (x10^6)**
AuAu	200	30	2	4	74.6
	62.4	30	2	4	31.4
	39	30	2	4	55.8
	27	30	2	-	24.1
	19.6	30	2	-	15.5
	11.5	30	2	-	2.4
	7.7	30	2	-	1.5
CuCu	200	30	2	-	5.2
	62.4	30	2	-	7.6
pp	200	30	2	-	2

Tesla magnetic field in STAR TPC. Using Helix-algorithm, the path of the charged particles are traced. Primary tracks, satisfying criteria for tracks with distance of closest approach (DCA) less than 3 cm and at least 10 hits in TPC pad rows, of an event are used for the analysis. In the TPC detector, tracks can have a maximum of 45 hits. For this analysis, minimum 20 hits are required for each track

to avoid track splitting effects. The tracks within $0.2 < p_T < 2.0$ GeV/c transverse momentum range are analyzed. The pseudorapidity, η, in the range $|\eta| < 0.5$ is used for the charged particles selections because of the uniform acceptance and counting efficiency for the charged particles in this region. Figure 6.8 shows the uniform η *vs* p_T acceptance of the STAR TPC and the blue window represents acceptance window used for the analysis. The full 2π azimuthal coverage of the TPC is used. To remove the beam pipe contamination, primary tracks with DCA < 1 cm is used.

Table 6.3: For the charged particles selection, various physics and experimental cuts have been listed.

Type	**Range**
Pseudorapidity (η)	-0.5 to 0.5
nFitPoints	>20
DCA	<1 cm
Track quality cut	>0.52
nhitsdedx	>10

In addition, extra cuts have also been used to remove spallation protons, originating due to particles hitting at beam pipe. These spallation protons have been removed within p_T range: 200< p_T <400 MeV/c with additional experimental cuts such as maximum hit points greater than 20 and global DCA less than 1 cm and 2σ on proton dE/dx (energy loss per unit length in TPC pad). The detail discussion about the background protons due to beam pipe interaction can be found in Ref. [72]. All the above quality cuts both on events and at track level have been considered to reduce the background fluctuation which may contribute to net-charge fluctuation.

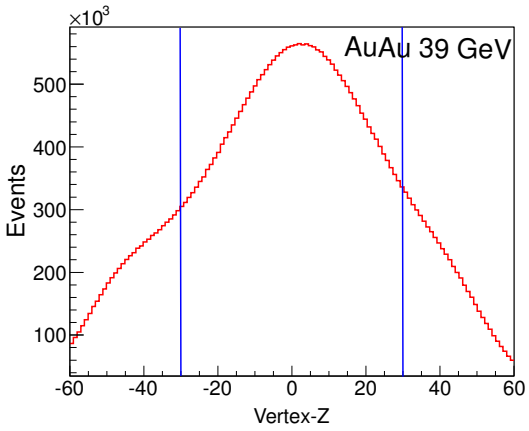

Figure 6.1: Vz distribution for AuAu 39 GeV.

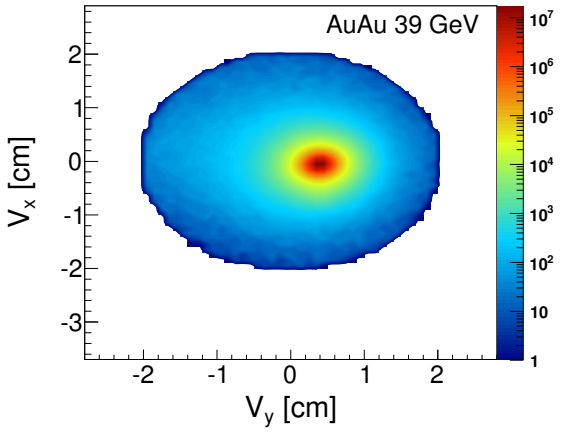

Figure 6.2: Vx vs Vy distribution for AuAu 39 GeV

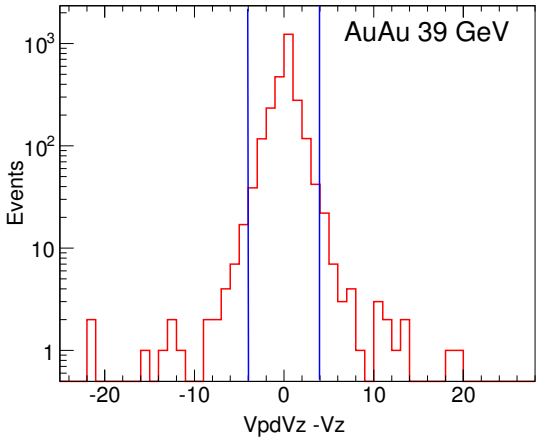

Figure 6.3: VpdVz - Vz distributions with analysis cut

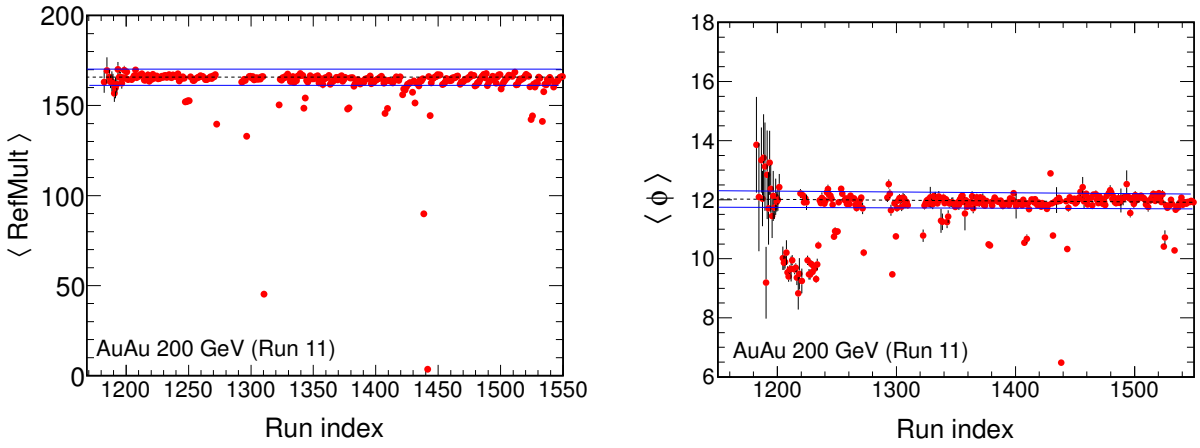

Figure 6.4: Run by Run QA for Au+Au collisions for 200 GeV based on <Refmult> and $< \phi >$.

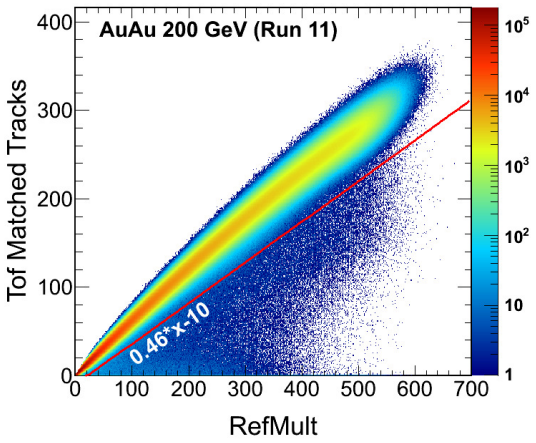

Figure 6.5: Presence of pile-up events in AuAu collisions at 200 GeV.

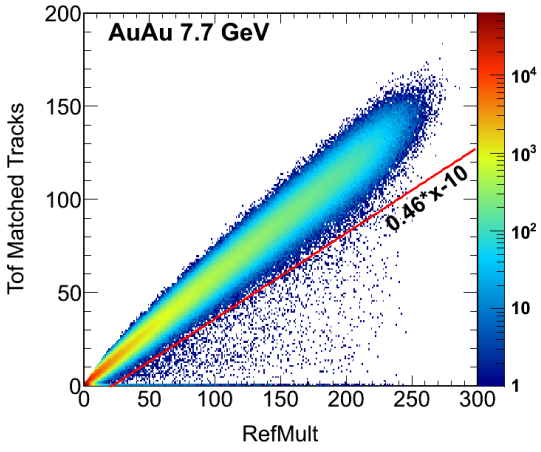

Figure 6.6: Presence of pile-up events in AuAu collisions at 7.7 GeV.

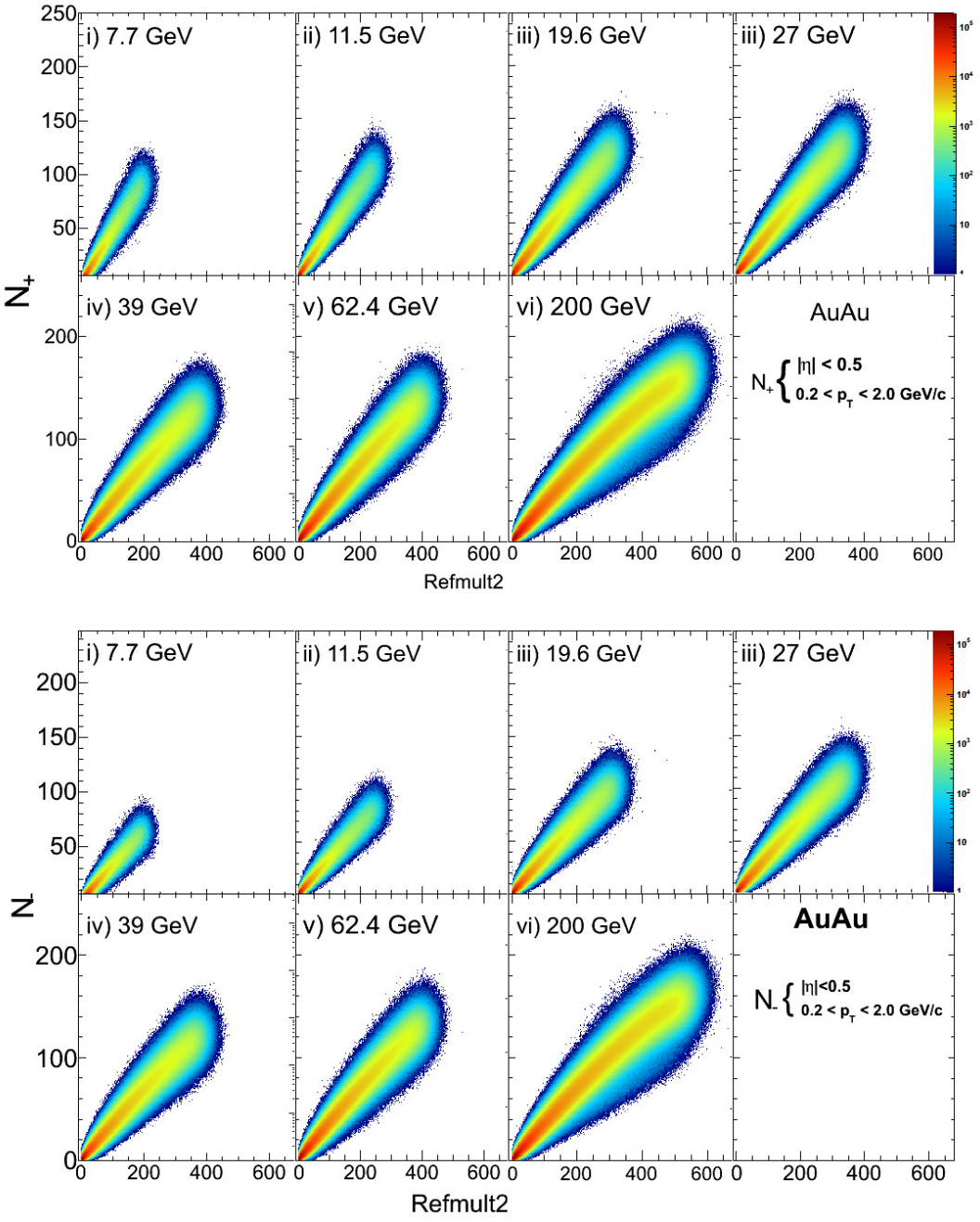

Figure 6.7: (Top panel) Positive charged particle multiplicity (N_+) *vs* Refmult2 and (Bottom panel) Negative charged particle multiplicity (N_-) *vs* Refmult2 after removing pile-up events.

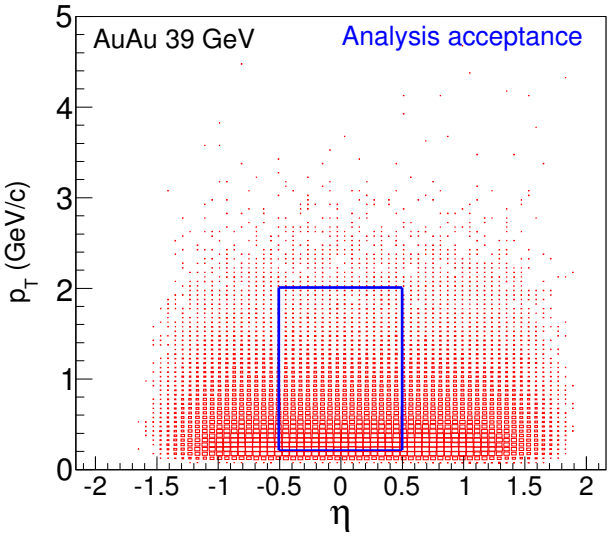

Figure 6.8: Uniform: η vs p_T acceptance for all charged particles. The blue boundary represents the analysis acceptance for the net-charge higher moment.

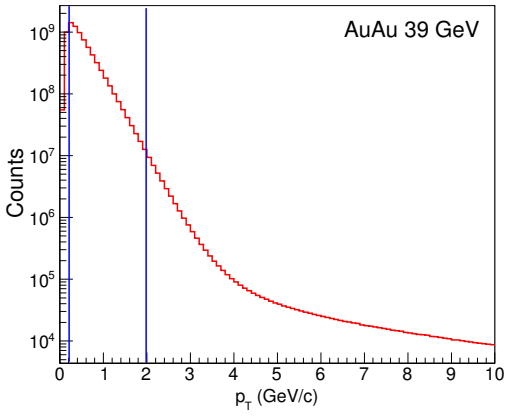

Figure 6.9: p_T distribution for AuAu 39 GeV.

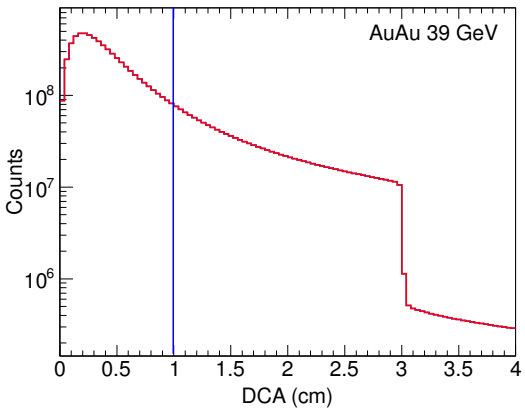

Figure 6.10: DCA distribution for AuAu 39 GeV

6.2 Centrality Determination

Each event in A-A collisions is characterized by number of participant nucleons (N_{part}), impact parameter of the collision (b) (as shown in Fig. 6.11), and/or number of binary collisions (N_{coll}). The average values of these variables over a collection of events are related to the collisions geometry of the colliding system. In heavy-ion-collisions, the collision geometry of the colliding system is also considered in terms of the total number of the inclusive charged particles multiplicity (N_{ch}) in a given acceptance. The cross-section of collision geometry, in the heavy ion collision, is expressed as the centrality class. The total inclusive charged particles multiplicity distribution is shown in the Fig. 6.13. It illustrates the various collision geometry of the A-A collisions in terms of N_{part}, b and N_{ch}. Based on the collision geometry or centrality class, events are coined as central, semi-central, semi-peripheral and peripheral as in the Fig. 6.13.

In heavy-ion-collisions, it is not possible to measure N_{part}, b or N_{coll} experimentally. But the mapping can be done by N_{ch} measured in each event with the average value of N_{part}, b and N_{coll}. This relates the experimentally measured observable with phenomenological calculated quantities. Experimentally, dN_{event}/dN_{ch} is estimated as illustrated in Fig. 6.13. By using Monte Carlo (MC) Glauber simulation [73] with known system geometry and p-p inelastic cross-section (σ_{inel}^{NN}), $< N_{part} >$, $< b >$ and $< N_{coll} >$ can be estimated.

6.2.1 Procedure to obtain centrality definition

In the STAR experiment, the inclusive charged particles are measured within given η window, like $|\eta| < 1.0$. Due to vertex reconstruction inefficiency at low multiplicity

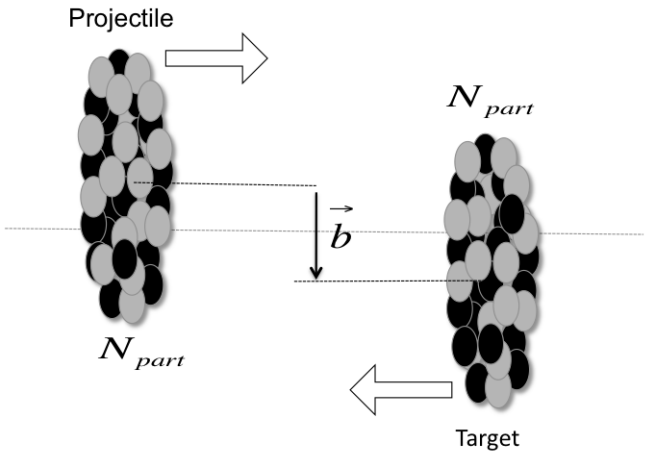

Figure 6.11: An illustration of the nucleus-nucleus collision. Here impact parameter (b) and number of participants are shown.

events or peripheral events, MC simulation are done to produce dN^{MC}_{event}/dN_{ch} mapping with true experimentally measured dN_{event}/dN_{ch}. This MC particle multiplicity are simulated by convolution of N_{part} distribution form MC Glauber simulation and a Negative Binomial Distribution (NBD),

$$NBD(n;\mu,k) = \frac{\Gamma(n+k)}{\Gamma(n+1)\Gamma(k)} \frac{(\mu/k)^n}{(n/k+1)^{n+k}}. \tag{6.1}$$

In Fig. 6.22, the correlation between N_{coll} and N_{part} are plotted from MC Glauber simulation for AuAu collisions at $\sqrt{s}_{\rm NN} = 200$ GeV. Similarly, for other BES energies, the MC simulations have been done. The MC multiplicity distribution can be reproduced by iterating NBD parameters. The relevant plots have been discussed in the following sections. Having simulated dN^{MC}_{event}/dN_{ch}, it is mapped with MC Glauber variables to get the mean values. The centrality class or event classification can be performed based on this MC simulated multiplicity and are defined as the fraction of the total integral of the multiplicity distribution. This can be understood

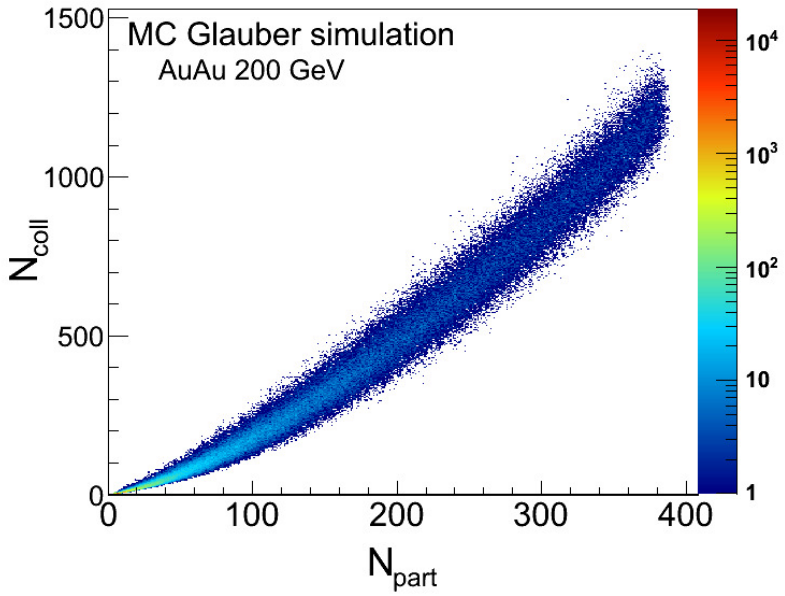

Figure 6.12: Number of binary collisions (N_{coll}) *vs* number of the participant nucleons are plotted for AuAu collisions at 200 GeV from MC Glauber simulation.

as follows

$$\frac{\int_{\infty}^{n_5} \frac{dN_{event}^{MC}}{dN_{ch}} dN_{ch}}{\int_{\infty}^{0} \frac{dN_{event}^{MC}}{dN_{ch}} dN_{ch}} = 0.05 \tag{6.2}$$

Here n_5 represents the bin number at which 5% of total integral occurred. So, any event lying above the multiplicity with number n_5 is considered top 0-5% central events. Experimentally, using these cuts centrality selection is performed in heavy-ion-collisions. In this analysis, similar methods have been undertaken and list of such centrality cuts have been tabulated and discussed in the following sections.

6.2.2 Auto-correlation effect and corrections technique

The traditional centrality selection in the STAR experiment is done by the uncorrected inclusive charged particle multiplicity within $|\eta| < 0.5$. Unfortunately, STAR

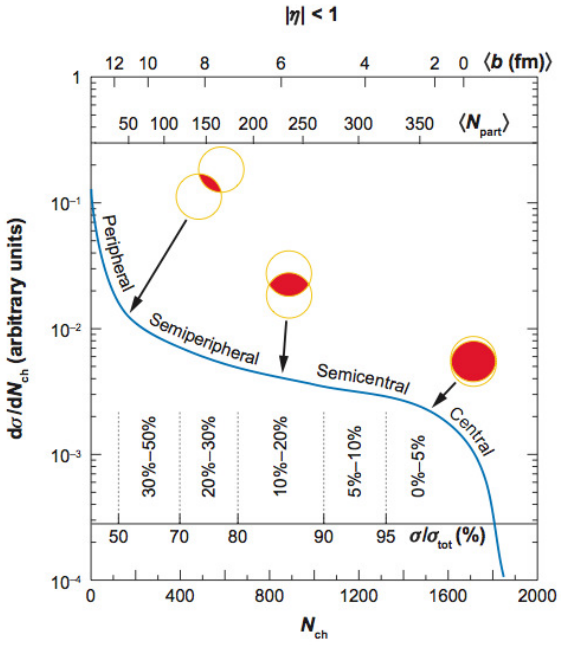

Figure 6.13: An illustration of the total inclusive charged particles multiplicity and number of participant (N_{part}) and impact parameter (b) of the AuAu collisions [71].

has no other good detector system for the centrality selection. In the net-charge higher moments analysis, all the charged particles have been selected in same η-window ($|\eta|$ <0.5). Because of same charged particles used in both the analysis and also in centrality selection, auto-correlation effect is expected to play significant role. And, this effect is observed in higher moments analysis for net-charge distribution. To reduce this effect, another centrality windows within $0.5 < |\eta| < 1.0$ is introduced. In Fig 6.15, it is shown that η *vs* p_T correlation indicating different η-windows for centrality selection and analysis region. Traditionally, the old centrality selection (with $|\eta|$ <0.5) is termed as Reference Multiplicity or shortly "RefMult", whereas this new centrality definition ($0.5 < |\eta| < 1.0$) is coined as Reference Multiplicity-2 or shortly "RefMult2". The net-charge distributions for AuAu collisions at 7.7 GeV for three centralities, 0-5%, 30-40%, and 60-70%, are

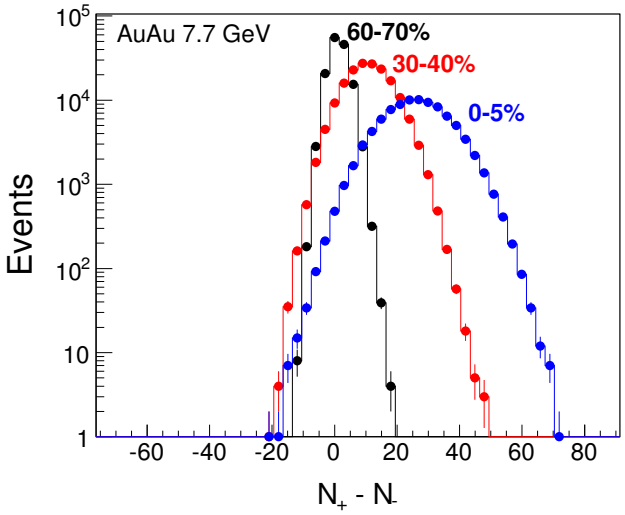

Figure 6.14: The net-charge distribution for AuAu collisions at 7.7 GeV for three centralities.

shown in Fig. 6.14. These centralities are estimated from "RefMult2" centrality definition. Figures. 6.16 show the higher moments of the net-charge distribution and their products for AuAu Collisions at 7.7 GeV colliding energy. Due to auto-correlation effect, the centrality selection procedure for the events is improper and it decreases the moments values. Therefore, by choosing suitable centrality definition, this effect can be reduced. So, RefMult2 definition is used through out this analysis.

To validate this new centrality definition, MC Glauber simulation has been performed for all energies. In Figs. 6.17, the MC simulated as well as measured multiplicity distributions are plotted and the ratio of the data to MC is shown. At peripheral collisions, the ratio of data to MC shows less than unity that is due to trigger inefficiency for low multiplicity events. Based on the MC simulated multiplicity, centrality definition is performed. Figure 6.18 shows the RefMult2 distributions from the data and that from MC simulation for the AuAu collisions at $\sqrt{s}_{\rm NN}$= 7.7

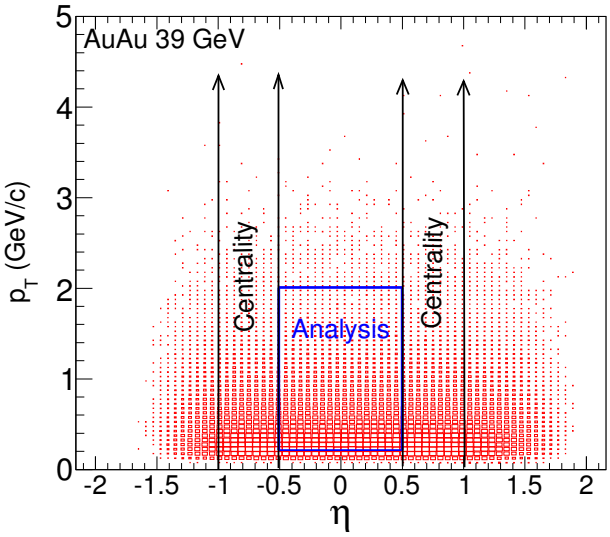

Figure 6.15: Centrality selection window and analysis window in η vs p_T distribution for AuAu 39 GeV

			Centrality								
System	$\sqrt{s_{NN}}$(GeV)		0-5%	5-10%	10-20%	20-30%	30-40%	40-50%	50-60%	60-70%	70-80%
AuAu	200	Refmult2	>453	>383	>268	>181	>117	>71	>40	>20	>9
		$< N_{part} >$	349.67	302.22	237.26	169.02	116.73	76.93	47.21	27.43	14.96
	62.4	RefMult2	>334	>279	>194	>131	>84	>51	>29	>15	>7
		$< N_{part} >$	344.4	296.71	232.08	164.59	113.49	75.08	46.26	26.56	13.78
	39	RefMult2	>307	>257	>179	>121	>78	>47	>27	>14	>7
		$< N_{part} >$	341.76	291.95	227.72	160.87	110.54	72.86	45.25	26.23	17.96
	27	RefMult2	>284	>237	>164	>111	>71	>43	>25	>13	>6
		$< N_{part} >$	340.96	291.78	227.42	167.17	110.87	72.93	45.43	26.06	13.43
	19.6	RefMult2	>258	>215	>149	>100	>65	>40	>22	>12	>5
		$< N_{part} >$	340.67	293.93	232.41	167.02	117.86	79.93	51.21	31.43	17.96
	11.5	RefMult2	>206	>172	>118	>80	>52	>32	>18	>9	>4
		$< N_{part} >$	338.42	288.74	224.29	158.38	109.30	71.92	44.32	25.59	14.044
	7.7	RefMult2	>165	>137	>95	>64	>41	>25	>14	>7	>3
		$< N_{part} >$	337.36	290.41	226.64	160.94	109.02	71.36	44.56	25.62	13.85
CuCu	200	RefMult2	>138	>120	>83	>56	>36	>22	>13		
		$< N_{part} >$	106.5	93.2	74.4	53.9	38.1	26.1	17.2		
	62.4	RefMult2	>97	>84	>58	>39	>25	>16	>10		
		$< N_{part} >$	103.2	90.1	71.8	52.1	36.8	25.3	16.7		

Table 6.4: Centrality definition for AuAu and CuCu collisions for RHIC energies. The RefMult2 cuts and $< N_{part} >$ have been listed for different centrality.

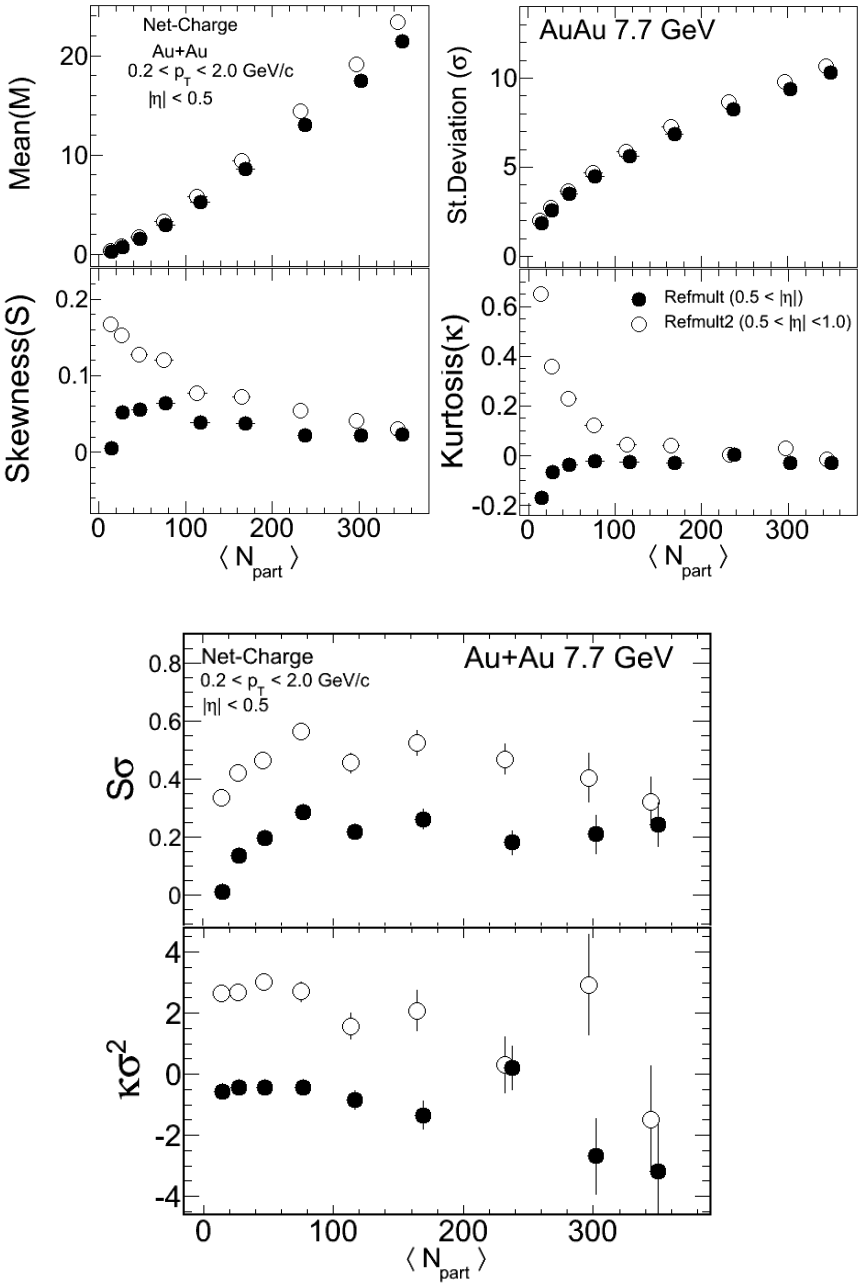

Figure 6.16: Higher moments of the net-charge distribution and their products for Au+Au collisions at 7.7 GeV center of mass energy using Refmult and Refmult2 centrality definition.

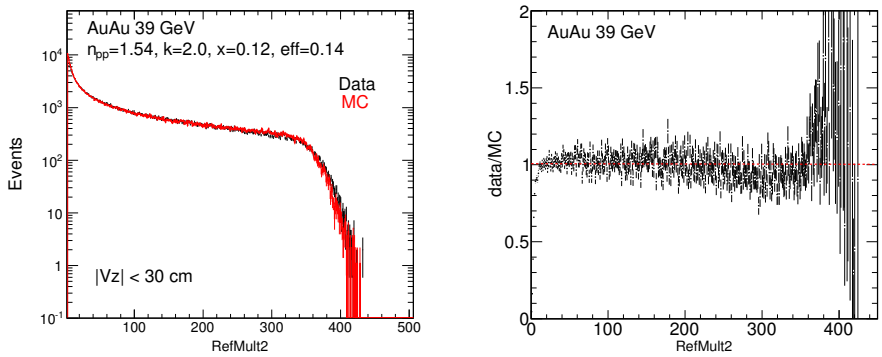

Figure 6.17: (left side) Data and MC: Refmult2 distribution. (right side) ratio of Data and MC distribution of Refmult2.

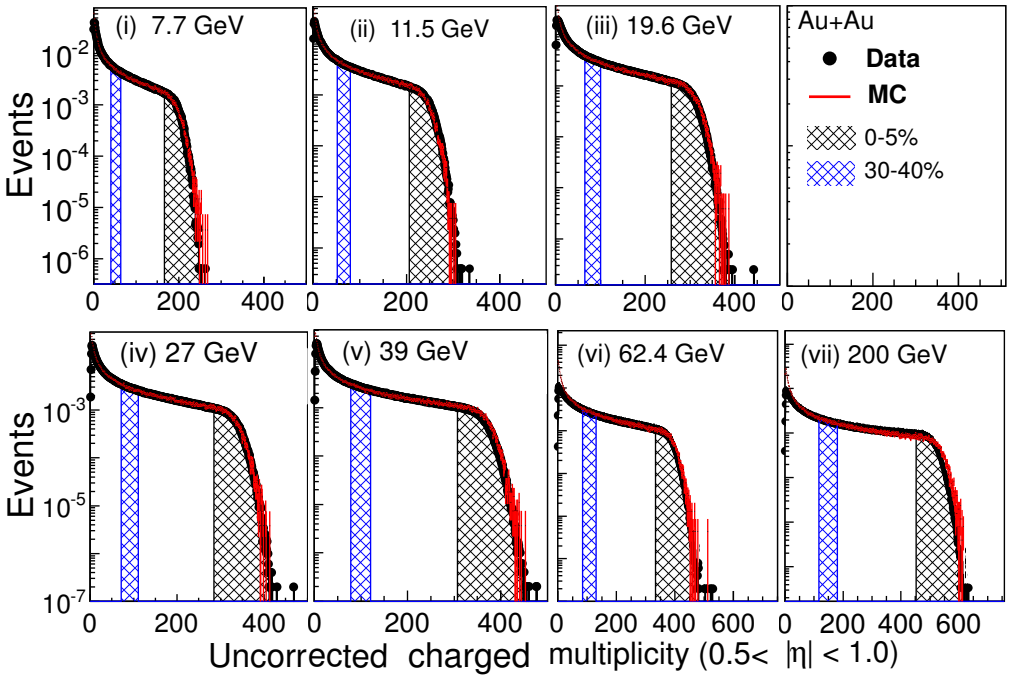

Figure 6.18: Refmult2 distributions for Au+Au collisions at $\sqrt{s}_{\rm NN}$= 7.7 to 200 GeV.

to 200 GeV for 0-5% and 30-40% centrality. In Table. 6.4, the RefMult2 cuts and corresponding $< N_{part} >$ have been listed for different centrality bins.

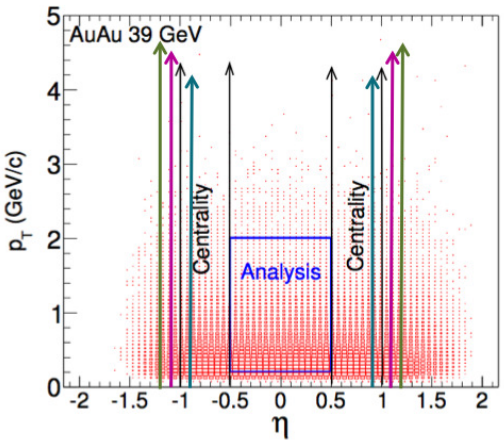

Figure 6.19: Various η-windows for the Refmult2 definition to check centrality resolution.

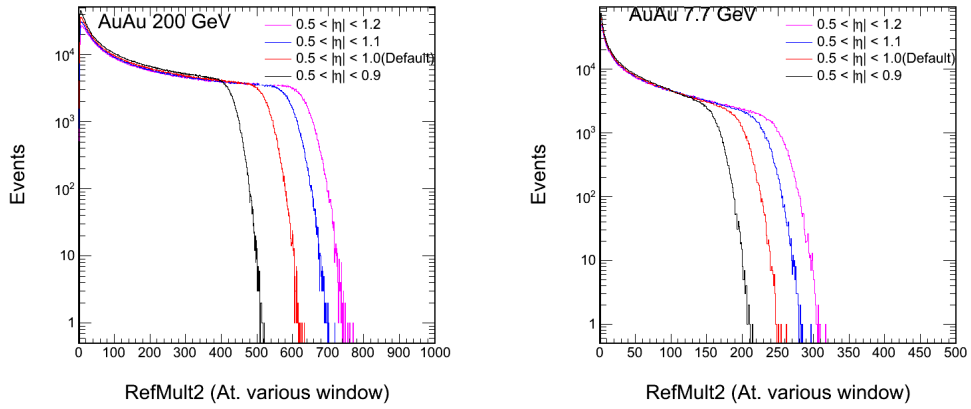

Figure 6.20: Refmult2 distribution at various η-windows for AuAu collisions at 200 and 7.7 GeV center of mass energy.

6.2.3 Centrality resolution effect

The choice of centrality definition in the heavy-ion-collisions plays a vital role in the physics analysis. Using RefMult2 centrality definition, to check the effect of the cen-

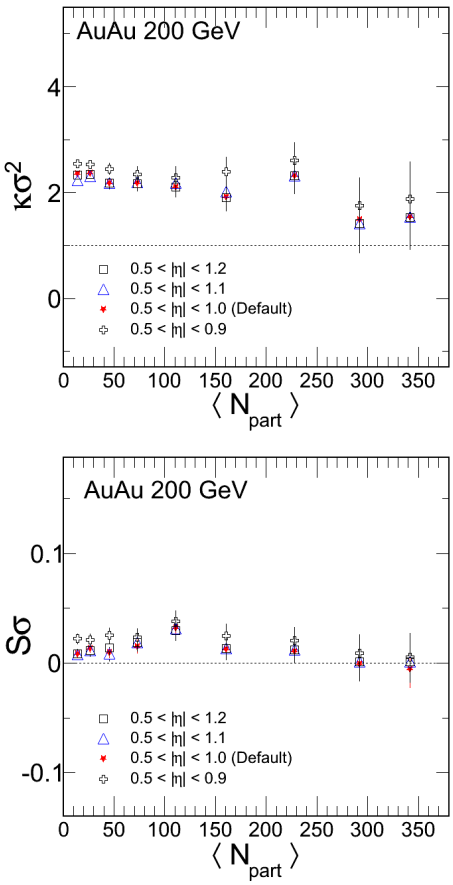

Figure 6.21: $\kappa\sigma^2$and $S\sigma$ for AuAu collisions at 200 GeV for different η-windows.

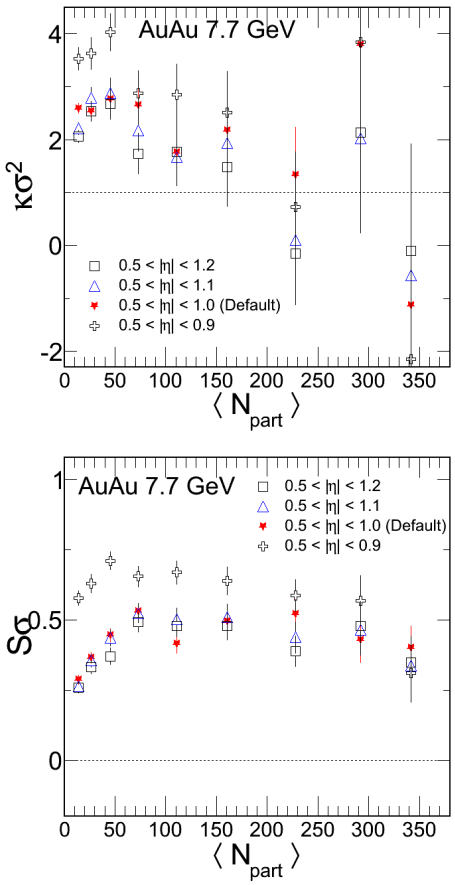

Figure 6.22: $\kappa\sigma^2$ and $S\sigma$ for AuAu collisions at 7.7 GeV for different η-windows.

trality resolution—the multiplicity distributions are varied by changing η-windows as shown in Fig. 6.19. Different η-windows have been studied like, $0.5 < |\eta| < 0.9$, $0.5 < |\eta| < 1.0$ (default), $0.5 < |\eta| < 1.1$ and $0.5 < |\eta| < 1.2$ as shown in the Fig. 6.19. The Refmult2 distributions for different η-windows are shown in the Figs. 6.20 for AuAu collisions at 200 and 7.7 GeV. By increasing the size of the η-window, the multiplicity distribution increases. For all four cases the higher moments for the net-charge distribution within $|\eta| < 0.5$ have been studied. In Fig. 6.21 and 6.22 show the $\kappa\sigma^2$ and $S\sigma$ for different η-windows. It is observed that with increasing centrality η-windows the value of the product of moments gets saturated above the size of η-windows of RefMult2. So, it is safe to use centrality definition using RefMult2 ($0.5 < |\eta| <1.0$) within ambit of the STAR detector system for centrality determination.

6.3 Centrality Bin Width Correction

A given centrality class is a collection of events having a range of impact parameters or $\langle N_{\rm part}\rangle$, thus comprising of events with different charged particle multiplicities. This results in additional fluctuations in the number of produced particles within each centrality class. Below we will discuss the effect of finite bin width of a given centrality class on the moments of distributions and prescribe a method to correct for this effect. Centrality classes were chosen using three different centrality bin widths, *viz.*, 2.5%, 5% and 10% of the cross section. From Fig. 6.23, it is observed that M and σ of the net–charge distributions are close to each other for all three centrality classes, whereas deviations are observed for S and κ, and their products

$(S\sigma, \kappa\sigma^2)$. This deviation is the result of choosing centrality class with a large bin.

The effect due to the finite centrality bin can be reduced by choosing smaller bins. In some cases because of practical reasons such as resolution of centrality determination, statistics of available events, it is not possible to choose fine bins. In this case, a centrality bin width weighting method can be used to minimize the effect. For this, net–charge distributions are constructed for finer bins in centrality within a centrality class. For moments of the distributions are obtained for each finer bin and weighted to get the final moments, according to:

$$X = \frac{\sum_i n_i X_i}{\sum_i n_i}, \tag{6.3}$$

where X represents a given moment, the index i runs over each fine centrality bin, n_i is the number of events in the i^{th} bin, and $\sum_i n_i$ is the total number of events in the given centrality class. Figure 6.24 shows the moments of net–charge distributions in each centrality class with appropriate weighting using centrality bin width method. After this correction, no centrality bin width dependence is observed in the three centrality classes. Hence the correction method does an appropriate job in correcting the finite centrality bin width effect.

6.4 Application of central limit theorem

As discussed in Section. 4.2.3-4, a Binomial and Poisson distribution approach Gaussian distribution under certain limits. The Gaussian distribution is closely related with the Central Limit Theorem (CLT), which states that,

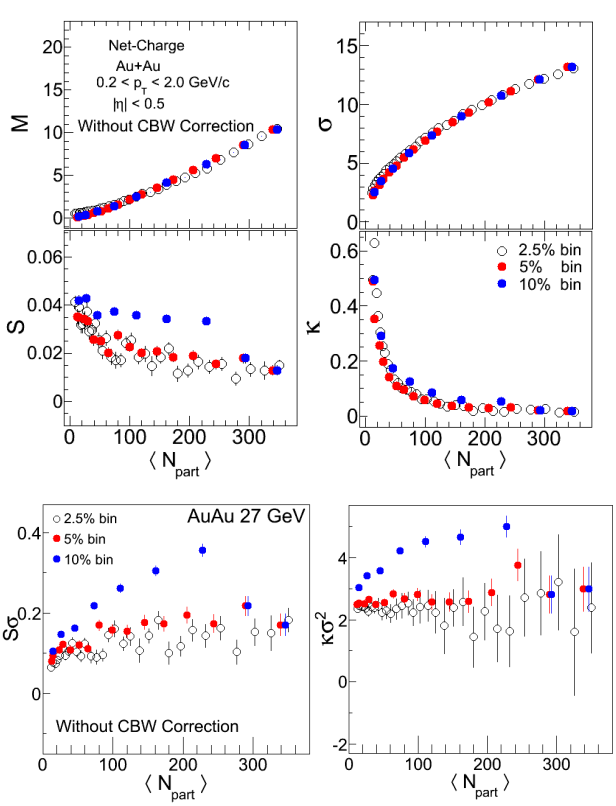

Figure 6.23: Upper panel: without CBW corrected for M, σ, S and κ Lower panel: that of $\kappa\sigma^2$and $S\sigma$ for AuAu collisions at 27 GeV center of mass energy.

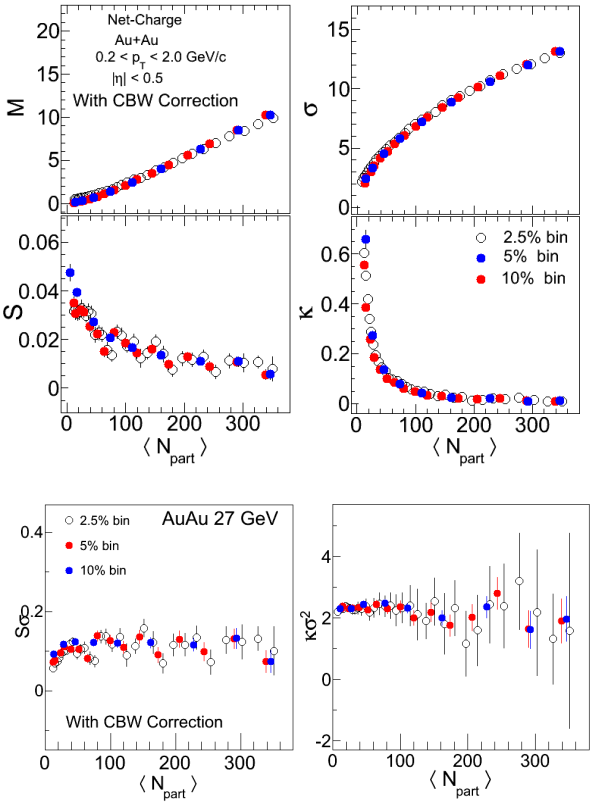

Figure 6.24: Upper panel: with CBW corrected for M, σ, S and κ Lower panel: that of $\kappa\sigma^2$and $S\sigma$ for AuAu collisions at 27 GeV center of mass energy.

" The sum of the independent and identically distributed (i.i.d) random variables follows a Normal/Gaussian distribution as the number of trials increases. "

Here the samples of random variables are said to be $i.i.d$ when each random variable is drawn from same parent probability distribution and all the random variables are mutually independent.

Mathematically, the CLT can be understood as follows,

if X_i, $i = 1, 2, 3, ..., n$, are $i.i.d$ random variables having probability distribution $f_i(x)$ with mean M_i and a variance σ^2. The random variable $Y = \frac{\sum_i X_i}{n}$, or average of X_i of each distribution $f_i(x)$ tends to Normal/Gaussian distribution with mean ($E[Y] = \frac{\sum_i M_i}{n}$) and variance ($Var[Y] = \frac{\sum_i \sigma_i^2}{n^2}$), as $n \to \infty$.

Therefore, using CLT, one can write down the form of mean and standard deviation, assuming M_i and σ_i same for all X_i as follows

$$M_i = n\ M(Y), \tag{6.4}$$

$$\sigma_i = \sqrt{n}\ \sigma(Y). \tag{6.5}$$

Similarly, for skewness and kurtosis [74], one can write down

$$S_i = 1/\sqrt{n}\ S(Y), \tag{6.6}$$

$$\kappa_i = 1/n\ \kappa(Y). \tag{6.7}$$

The centrality evolution of the higher moments can be understood better by invoking the CLT, which gives the dependence of the moments on the number of participating nucleons. In this case, one can consider the number of sample size

n as average number of participating nucleons, $< N_{\rm part} >$, in a centrality class. And each N_{part} can be considered by the source of independent emission of particles production. As in this case, there is no idea about the parent distribution. The moments can be written as follows

$$\begin{aligned} M &\propto < N_{\rm part} >, \\ \sigma &\propto \sqrt{< N_{\rm part} >}, \\ S &\propto \frac{1}{\sqrt{< N_{\rm part} >}}, \\ \text{and } \kappa &\propto \frac{1}{< N_{\rm part} >}. \end{aligned} \tag{6.8}$$

Here $\langle N_{\rm part} \rangle$ can be treated as the proxy for the volume of the system size. As going from peripheral to central, volume of the system increases. These moments show the volume dependence and these dependence can be cancelled by suitably multiplying these moments.

The centrality dependence of higher moments of the net-charge distribution are fitted with CLT expression as in Equations. 6.8. Fig. 6.25-6.27 show the CLT fit for the four moments. The χ^2/ndf of each CLT fitting for M, σ, S and κ is plotted for seven energies in Fig 6.28. Here for a given energy, M, σ, S and κ are fitted with respective CLT form as given in the above expression with constant of proportionally as a free parameter. It is due to the lack of information about the constant of proportionality in experiment. The CLT fitting give the idea that the higher moments of the distribution tend to the value that of the Gaussian distribution as the system possesses large and large independent emission sources.

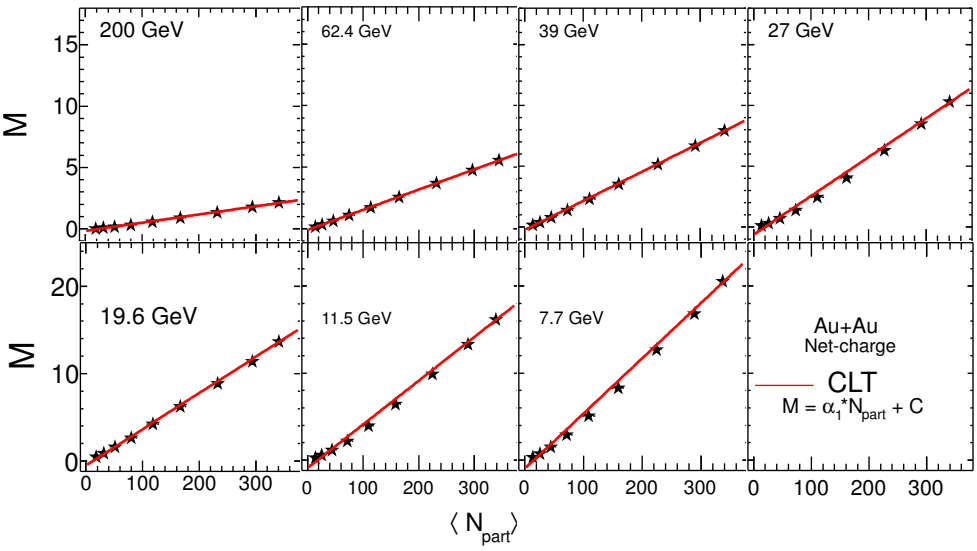

Figure 6.25: Mean (M) vs $\langle N_{\rm part} \rangle$. The red line represents the fitted CLT expectation.

6.5 Error estimation

For the higher moments of the net-charge distributions, statistical and systematical errors have been estimated. The statistical error estimations have been performed in several ways and discussed in Section 6.5.1. The uncertainties due to instrumental cause are discussed in Section 6.5.2. In addition to this, detector efficiency also gives rise to an additional uncertainty in the higher moments of the net-charge distribution. This has been elaborated in Section 6.6.

6.5.1 Statistical Error

The higher moments of the net-charge distribution analysis needs large statistics to minimize the statistical fluctuation. So, for the limited statistics, this analysis needs very careful measurement of the statistical uncertainty. For this analysis four ways, of calculating the statistical error have been employed — such as, 5 Sub-group [A.1],

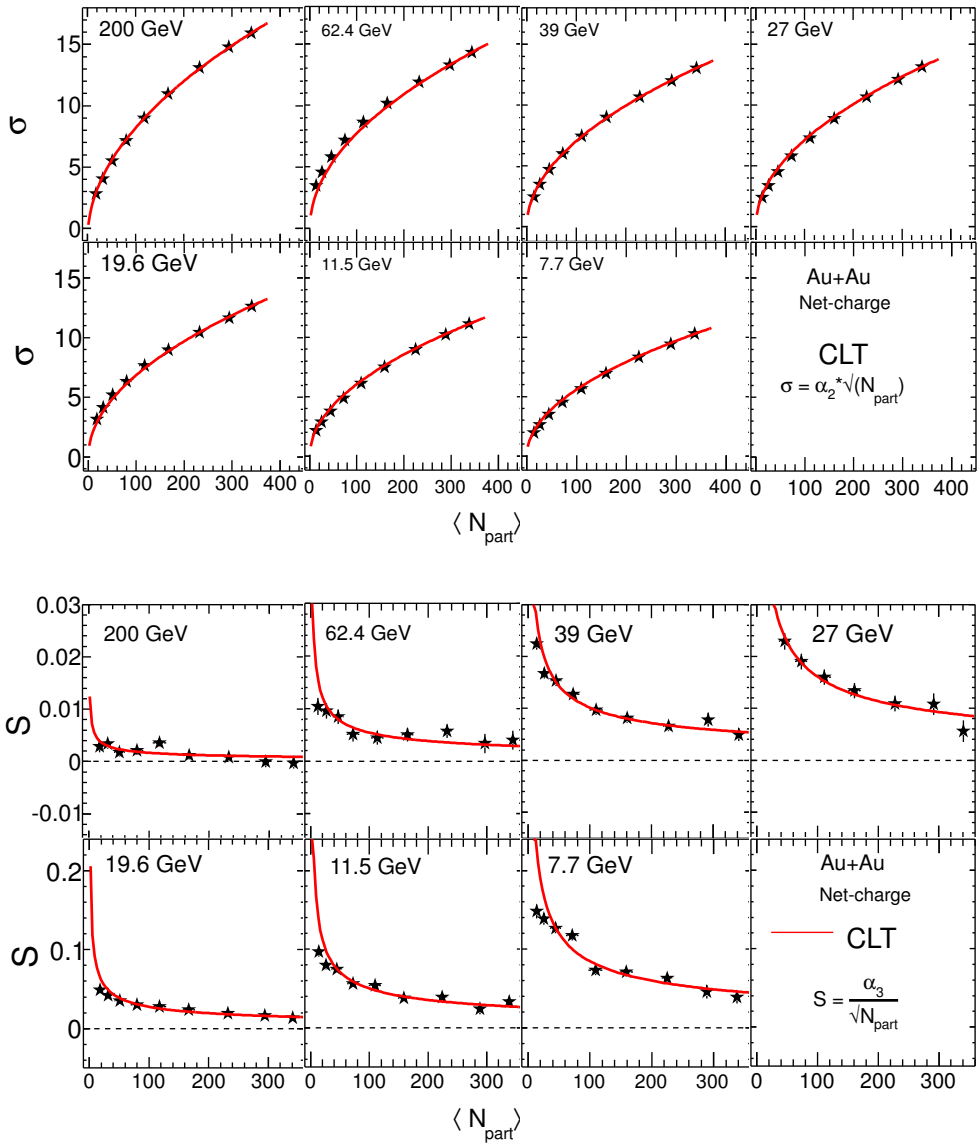

Figure 6.26: Standard Deviation (σ) and Skewness (S) vs $\langle N_{\rm part} \rangle$. The red line represents the fitted CLT expectation.

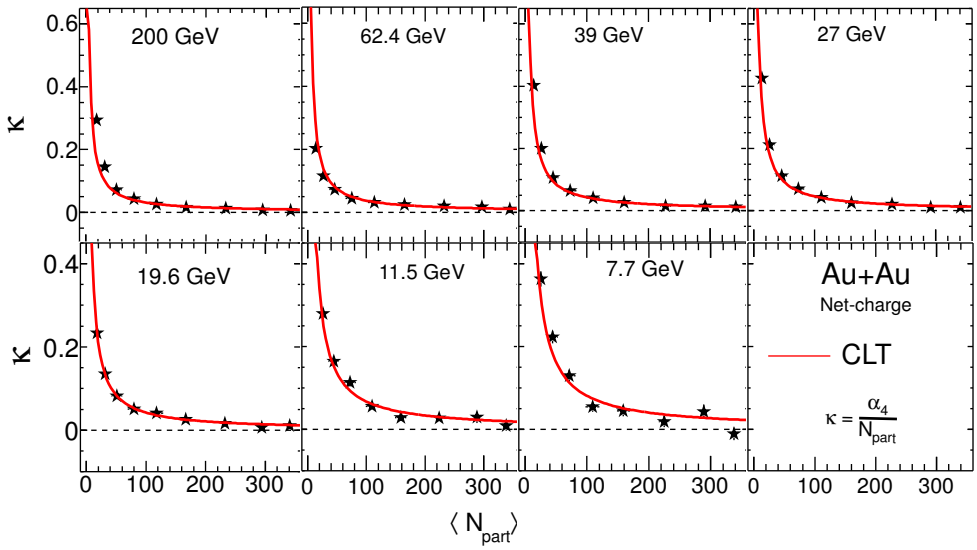

Figure 6.27: Kurtosis (κ) vs $\langle N_{\rm part} \rangle$. The red line represents the fitted CLT expectation.

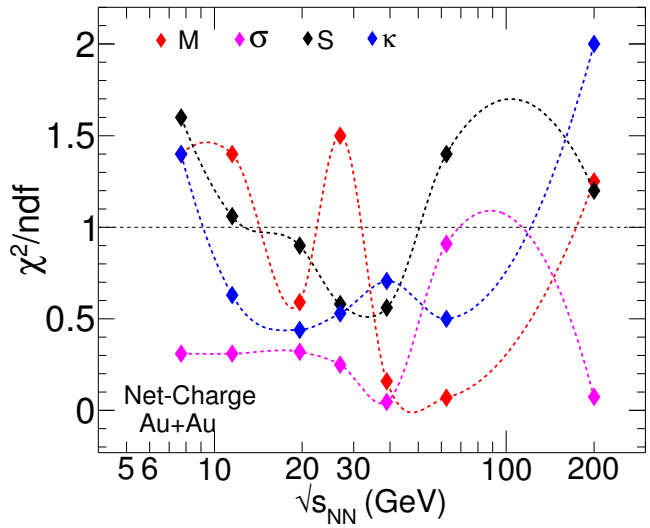

Figure 6.28: χ^2/ndf for each moment as a function of $\sqrt{s}_{\rm NN}$

Analytic [A.2], Bootstrap [A.3] and Delta theorem [75] methods. In fig. 6.29, the statistical errors for above four approaches have been shown for $\kappa\sigma^2$and $S\sigma$. It is observed that 5-subgroup method gives very random values of the error irrespective of the statistics of the centrality class. On the other hand, analytical method also overestimate the statistical error. The Bootstrap and Delta theorem method are observed to be consistent to each other. The Delta theorem method have been used for the estimation of the statistical error through out this analysis.

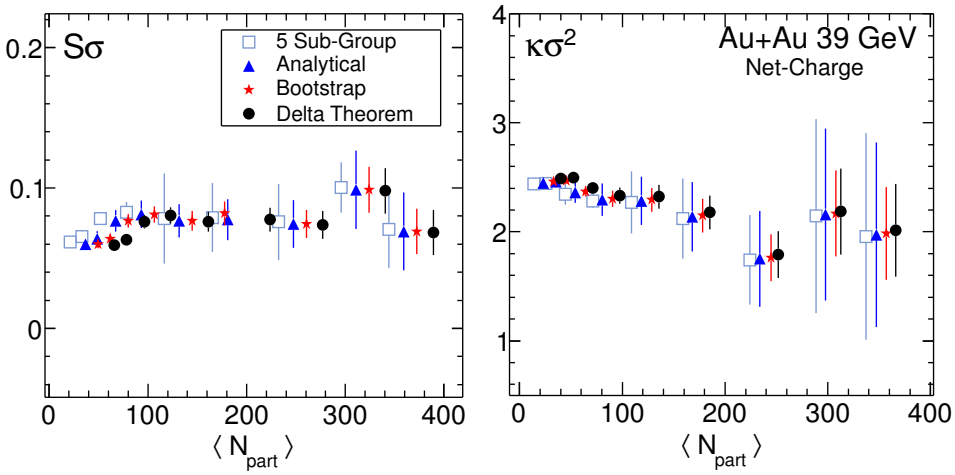

Figure 6.29: Different approaches of the statistical error estimation and their comparison, for AuAu collisions at 39 GeV, for $\kappa\sigma^2$and $S\sigma$.

6.5.2 Systematic Error

Systematic uncertainty has been estimated based on the STAR TPC detector system. The charged particles are measured for this analysis by the STAR TPC using suitable track quality cuts on the number of hits point (nFitpoints), distance of

closest approach (DCA), and the number of hits for the *dE/dx* measurement (nhitsdedx). These track quality cuts play an important role in counting the number of the positive and negative charged particles for the net-charge distribution. Significant change in default cuts for this analysis makes noticeable changes in final results of the net-charge distribution. So in order to make the results unbiased on choosing track quality cuts for the systematic error estimation, above cuts are chosen such that the mean of net-charge of the distribution ought to have close values to that of the data. The systematic variation for the efficiency uncorrected higher moments and their products are discussed below. The efficiency correction procedure is discussed in next Section 6.6.2

For the systematic error estimation, following track quality cuts have been studied for the efficiency uncorrected results.

- nFitpoints: 18, 19, 20(default), 21, 22
- DCA: 0.8, 0.9, 1.0 (default), 1.1, 1.2
- nhitsdedx: 8, 9, 10 (default), 11, 12

So, by varying above experimental cuts, the systematic error has been estimated and the formula used for these estimation is as follows

$$RMS = \sqrt{\frac{1}{n}\sum_{i}\frac{Y_i - Y_{St.Cut}}{Y_{St.Cut}}}, \qquad Sys.Err = Y_{St.Cut}\sqrt{\sum RMS^2}. \tag{6.9}$$

Where , Y_i : moments values from different cuts and $Y_{St.Cut}$: moments values from Standard (default) cut .

Figure. 6.30 shows all the efficiency uncorrected moments plots for varying DCA about its default mean value of the net-charge distribution for AuAu collisions at

39 GeV. Here the mean and standard deviation are observed to have negligible dependence (about 1% variation) on the variation of DCA about its default mean values of the net-charge distribution. The skewness and kurtosis do show a small dependence on the DCA cut. Similar studies have been done for all experimental cuts (as listed in the above bullets) and for all energies. The systematic uncertainties are found to be 4%, 1%, 16% and 9% on average over all energies and centrality for M, σ, S and κ, respectively. The DCA variation shows 20% and 10% variation in the $S\sigma$ and $\kappa\sigma^2$, respectively.

In case of efficiency corrected results, additional systematic errors have also been included. Those are followings.

1. Effect of track quality cuts on efficiency estimation

   In this case, three types of track cuts have been selected that give optimum variation of mean of the net-charge values. Those cases are followings.

   - Case-1: nFitPoints>23 and DCA > 1.0 cm
   - Case-2: nFitPoints>20 and DCA > 1.3 cm
   - Case-3: nFitPoints>18 and DCA > 1.0 cm
   - Default: nFitPoints>20 and DCA > 1.0 cm

   The systematic variation for the above cases are shown in Fig. 6.31. Similarly, for other energies, these are also done. It is observed that up-to 50% variation is observed in both the moments products.

2. Effect of 5% efficiency on higher moments of the net-charge distribution

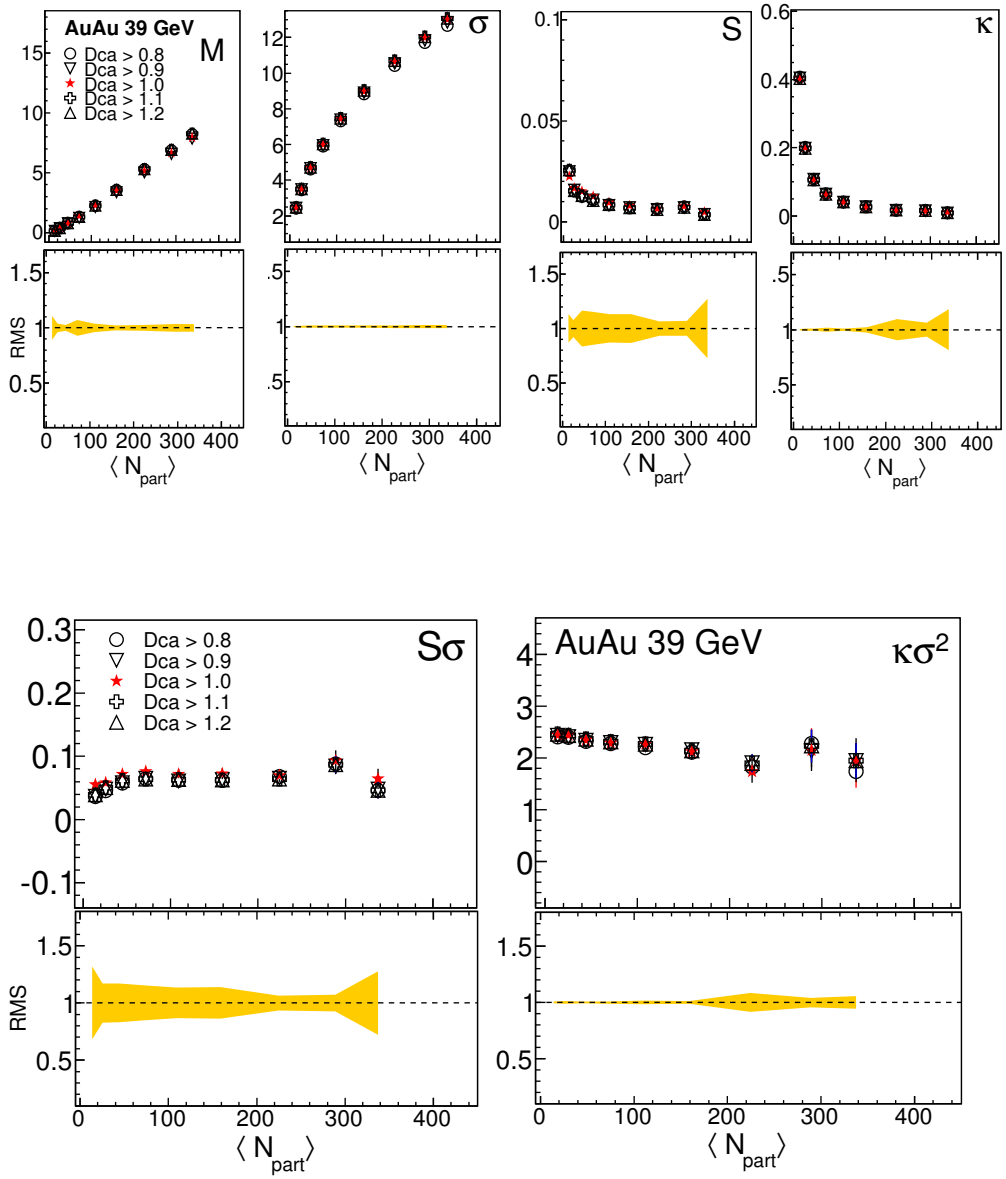

Figure 6.30: Efficiency uncorrected mean, standard deviation, skewness, kurtosis and their products have been plotted as a function of $\langle N_{\rm part} \rangle$by varying DCA.

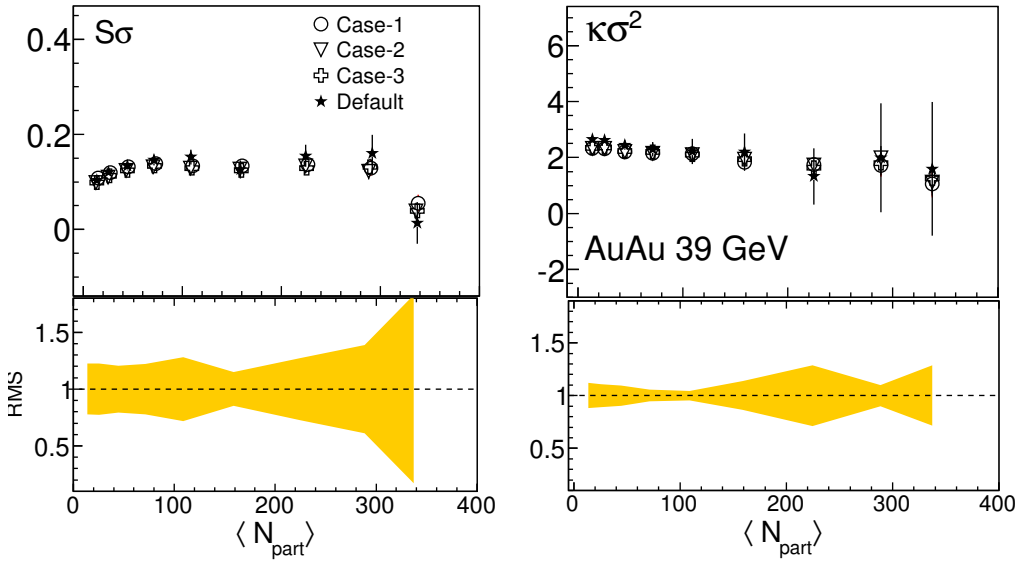

Figure 6.31: The Efficiency corrected mean, standard deviation, skewness, kurtosis and their products have been plotted as a function of $\langle N_{\rm part}\rangle$by track quality cuts for the efficiency estimation. Here Case-1: nFitPoints>23 and DCA $>$ 1.0 cm, Case-2: nFitPoints>20 and DCA $>$ 1.3 cm, Case-3: nFitPoints>18 and DCA $>$ 1.0 cm, and Default: nFitPoints>20 and DCA $>$ 1.0 cm.

The efficiency, estimated from the embedding sample, is not perfect. It is observed that there is 5% variation in efficiency due to contamination. This variation are included in systematic error in higher moments of the net-charge distribution. In this case, the efficiency for each centrality is varied ±5% of the default values.

6.6 Detector effect

Every instrument has finite efficiency to perform a certain task. In STAR experiment, all detectors and trigger system have finite efficiency for tracking particles and to identify the events respectively. The higher moments of the net-charge distributions are affected by these finte efficiencies.

To understand the event-by-event charged particles detection efficiency, one has to know the sources of the inefficiency. There are several controbuting factors for example, tracking inefficiency, inefficiency due to acceptance, vertex reconstruction inefficiency, momentum resolution inefficiency etc. in heavy ion collisions. These inefficiencies are very difficult to correct in an event-by-event analysis. In addition to this, efficiencies — due to different sources— are not additive. The expressions of the higher order cumulant (combination of cumulants give various moments of the distributions) are very sensitive to the higher power of fluctuation like efficiency fluctuation. In Section 6.6.1, the effect due to efficiency on the net-charge higher moments have been discussed in details.

6.6.1 Geant simulation study

As we discussed in previous section, to take into account the difference due to detector effects on higher moments both HIJING+GEANT and HIJING events have been studied. In this case, HIJING+GEANT events have been simulated in exactly similar way as the data of AuAu collisions at 19.6 GeV. Similar track quality cuts mentioned in Table. 6.3 and event cuts, like Vertex-r and Vertex-z, have been used to make data like events.

In Fig. 6.32, the positive and negative charged particles distributions are presented for 0-5%, 30-40%, and 60-70% centrality bins and in Fig. 6.34 the net-charge distributions have been presented for three centrality bins for HIJING and HIJING+GEANT. The mean and width of the distribution changed due to efficiency effect. The M, σ, S, and κ, for AuAu collisions at 19.6 GeV for HIJING+GEANT and HIJING, are shown in Fig. 6.34 and that of $\frac{\sigma^2}{M}$, $S\sigma$, and $\kappa\sigma^2$ are shown in Fig. 6.35. It is observed that due to detector/efficiency effect M and σ decrease, whereas S and κ and the values of $\frac{\sigma^2}{M}$, $S\sigma$, and $\kappa\sigma^2$ increase for all centralities.

6.6.2 Efficiency correction for cumulants

Let us consider the net-charge probability distribution, $P(N_+, N_-)$, of positively charged particles, N_+, and Negatively charged particles, N_-, of ideal detector (efficiency 100%). Assuming binomial probability distribution for the efficiency in the detector,

$$p(n_+, n_-) = \sum_{N_+=n_-} \sum_{N_-=n_-} B(n_+|N_+, \epsilon_+) B(n_-|N_-, \epsilon_-) P(N_+, N_-). \tag{6.10}$$

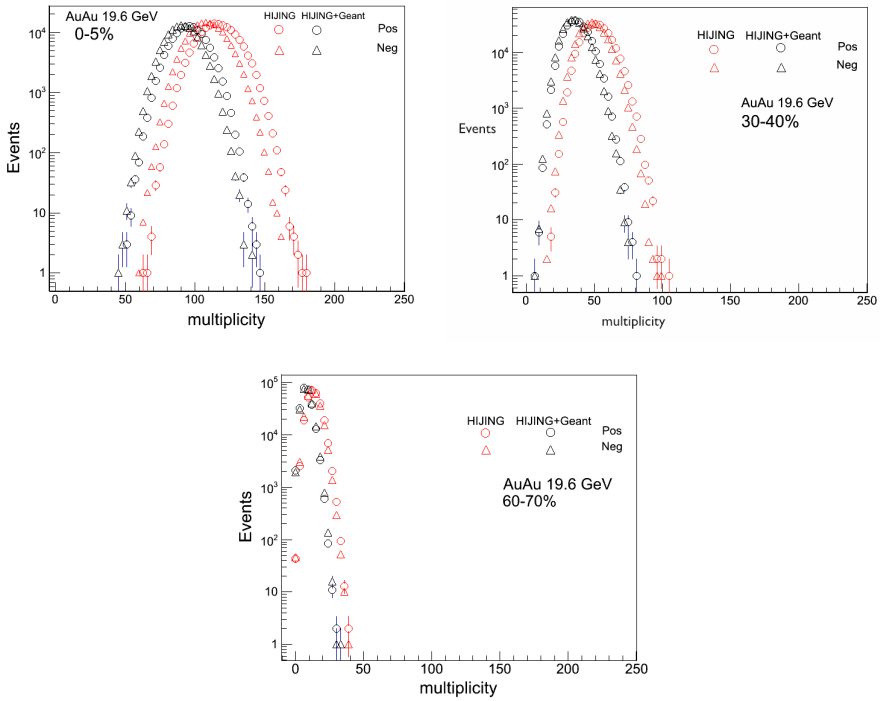

Figure 6.32: The positive and negative charged multiplicity distribution, for 0-5%, 30-40%, 60-70%, for AuAu collisions at 19.6 GeV for HIJING+GEANT and HIJING.

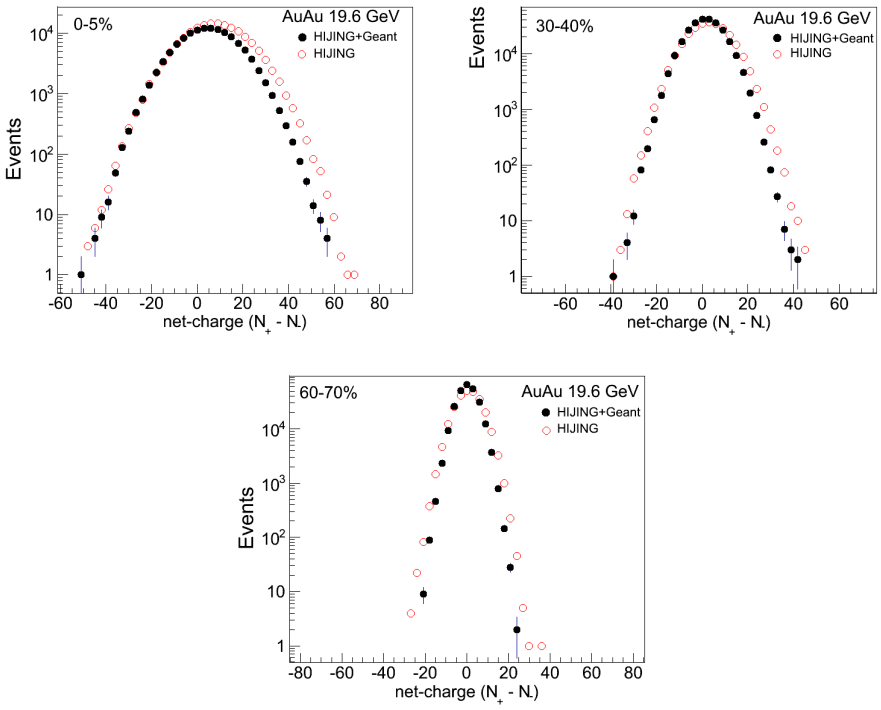

Figure 6.33: The net-charge distribution, for 0-5%, 30-40%, 60-70%, for AuAu collisions at 19.6 GeV for HIJING+GEANT and HIJING.

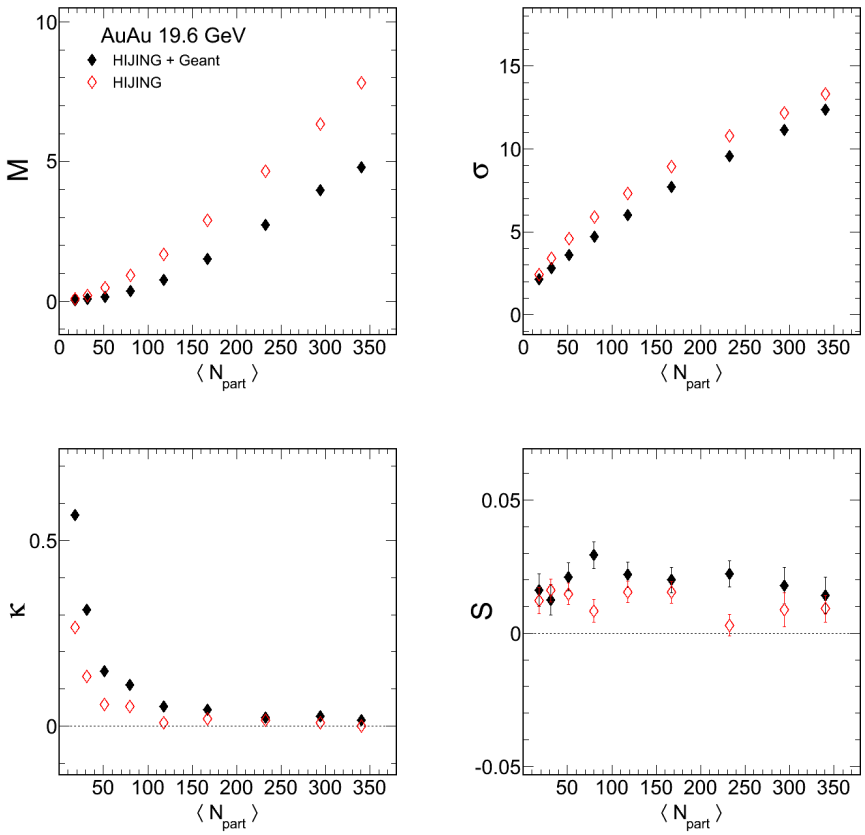

Figure 6.34: The M, σ, S, and κ for AuAu collisions at 19.6 GeV for HIJING+GEANT and HIJING. The charged particles are selected within $|\eta| < 0.5$ and $0.2 < p_T < 2.0$ GeV/c.

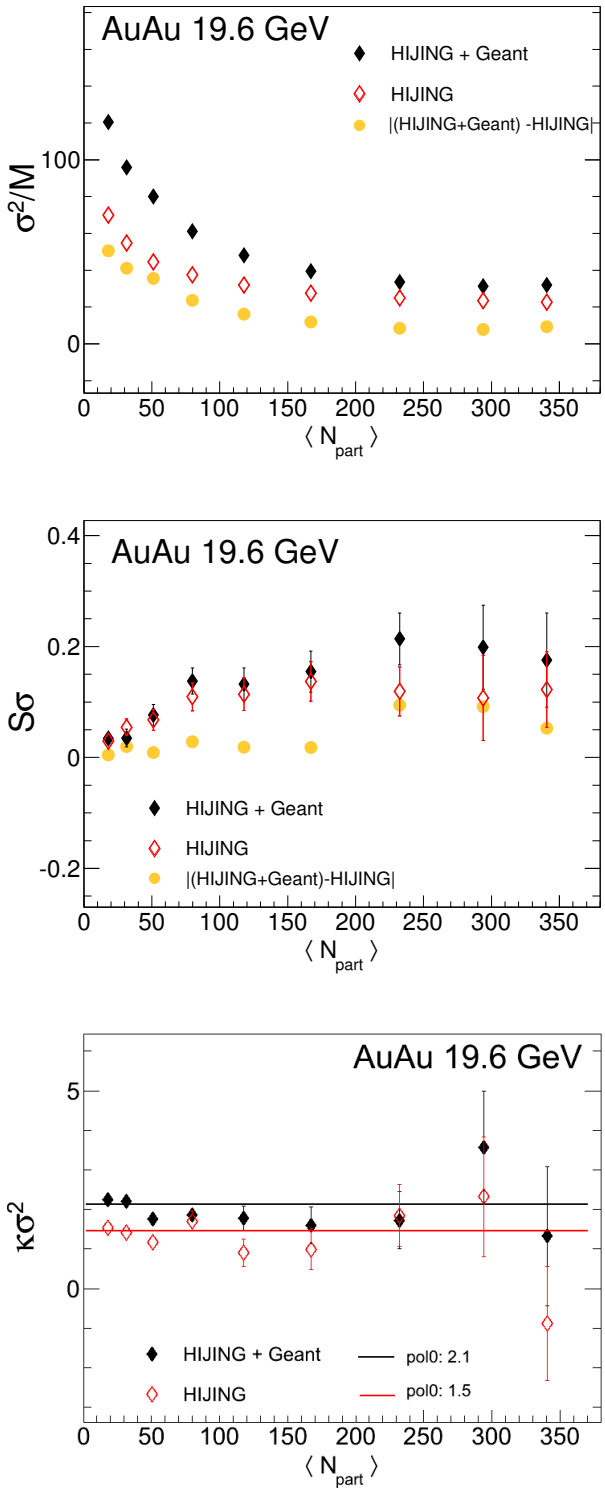

Figure 6.35: The $\frac{\sigma^2}{M}$, $S\sigma$, and $\kappa\sigma^2$ for AuAu collisions at 19.6 GeV for HIJING+GEANT and HIJING. The charged particles are selected within $|\eta| < 0.5$ and $0.2 < p_T < 2.0$ GeV/c.

Here $p(n_+, n_-)$ is the measured net-charge probability distribution with positive and negative charged particles efficiency ϵ_+ and ϵ_+. Then the moment generating function can be defined as

$$m(z) = \sum_{N_+=n_-} \sum_{N_-=n_-} P(N_+, N_-)[1-(1-z)\epsilon_+]^{N_+}[1-(1-z^{-1})\epsilon_-]^{N_-}. \quad (6.11)$$

The cumulant generating function can be defined as

$$g(t) = ln[l(e^t)] = \sum_{k=1}^{\infty} \frac{t^k}{k!}. \quad (6.12)$$

We can construct different cumulants both for true and measured, using following expression

$$c_n = \frac{d^n g(t)}{dt^n}|_{t=0}, \qquad C_n = \frac{d^n G(t)}{dt^n}|_{t=0}. \quad (6.13)$$

Here, c_n and C_n are the n^{th} order measured and true cumulants and $G(t)$ is the cumulant generating function at $\epsilon_- = \epsilon_+ = 1$. In the net-charge analysis, for simplification one can assume $\epsilon_- = \epsilon_+ = \epsilon$. Using above expressions, it can be derived for

the efficiency correction of cumulant,

$$C_1 = c_1/\epsilon, \tag{6.14}$$

$$C_2 = (c_2 - n(1-\epsilon))/\epsilon^2, \tag{6.15}$$

$$C_3 = (c_3 - c_1(1-\epsilon^2) - 3(1-\epsilon)(f_{02} - f_{02} - nc_1))/\epsilon^3, \tag{6.16}$$

$$C_4 = (c_4 - n\epsilon^2(1-\epsilon) - 3n^2(1-\epsilon)^2 - 6\epsilon(1-\epsilon) \tag{6.17}$$
$$\times(f_{20} + f_{02}) + 12c_1(1-\epsilon)(f_{20} - f_{02}) - (1-\epsilon^2)(c_2 - 3{c_1}^2)$$
$$-6n(1-\epsilon)({c_1}^2 - c_2) - 6(1-\epsilon)(f_{03} - f_{12} + f_{02} + f_{20} - f_{21} + f_{30}))/\epsilon^4.$$

Here n is the measured average total charged particles. f_{ij} is the factorial moment of the measured distribution. Using Eq. 6.10, it can be derived that,

$$f_{ij} = \epsilon_+^i \epsilon_-^j F_{ij}. \tag{6.18}$$

Where F_{ij} is the true factorial moments. The factorial moments factories the efficiency as expressed above. The detail derivation can be found in Ref. [76]. In the next section, the procedure of obtaining efficiency for positive and negative charged particles are discussed in details.

6.6.3 Efficiency estimation

In the net-charge analysis, average efficiency, $\epsilon = \frac{\epsilon_+ + \epsilon_-}{2}$, is taken for the cumulant correction. In the STAR experiment, efficiencies are estimated by embedding Monte Carlo (MC) tracks in the real events. The reconstruction algorithm is used to get back the number of embedded MC tracks in the real events. The efficiency is

estimated based on the real embedded MC tracks and reconstructed tracks of an event. In the embedding procedure, identified particles, like $p, \bar{p}, \pi^+, \pi^-, K^+$ and K^-, etc., are used. In Fig. 6.36, the p_T dependance of efficiency for the π^+ for 0-5% centrality is shown. These efficiencies are estimated based on the net-charge analysis track and vertex cuts (as given in table 7.2 and 6.1). To estimate the efficiency for

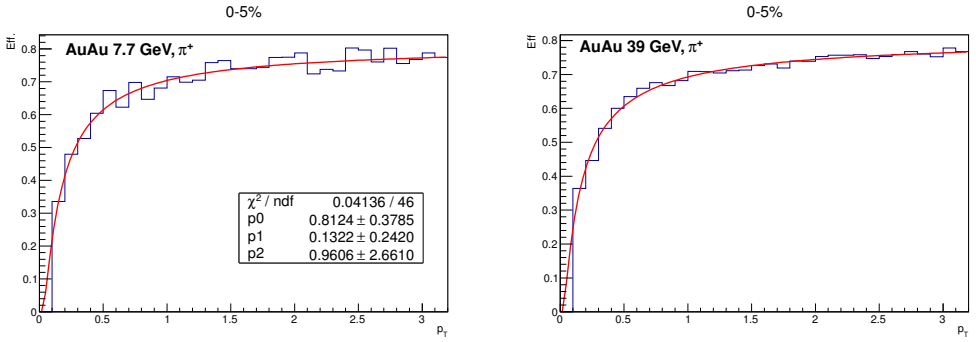

Figure 6.36: The p_T dependance of efficiency, for 0-5% centrality, of Au+Au collisions at 7.7 and 39 GeV for π^+ are plotted.

the positive charged particles, it is assumed that total positive charged particles are collection of p, K^+ and π^+. Similarly for the efficiency of negative charged particles, it is assumed that total negative charge particles are collection of $\bar{p}, K^-$ and π^-. The weighting is done as following expression

$$w_p + w_{K^+} + w_{\pi^+} = 1. \tag{6.19}$$

Where w_x is the weight of particle species x. The values of w_p, w_{K^+} and w_{π^+} are estimated from the particle ratio as follows

$$\frac{p}{\pi^+} = r, \frac{K^+}{\pi^+} = s. \tag{6.20}$$

These particles ratios are taken from the respective particle p_T spectra. Using Eq. 6.19 and 6.20, one can find

$$w_{\pi^+} = \frac{1}{r+s+1}, \tag{6.21}$$

$$w_p = r w_{\pi^+}, \tag{6.22}$$

$$w_{K^+} = s w_{\pi^+} \tag{6.23}$$

and similarly for anti-particles. Expression for positive and negative charge particle efficiency with above weight is expressed as follows,

$$\epsilon_+ = w_p \epsilon_p + w_{K^+} \epsilon_{K^+} + w_{\pi^+} \epsilon_{\pi^+}, \tag{6.24}$$

$$\epsilon_- = w_{\bar{p}} \epsilon_{\bar{p}} + w_{K^-} \epsilon_{K^-} + w_{\pi^-} \epsilon_{\pi^-}. \tag{6.25}$$

Where w_x and ϵ_x are the weight and efficiency of particles species x. w_x is estimated from the particle ratio for different charged particles like, $\frac{p}{\pi^+}$, $\frac{\bar{p}}{\pi^-}$, $\frac{K^+}{\pi^+}$, $\frac{K^-}{\pi^-}$, and ϵ_x is estimated by integrated p_T dependance efficiency using expression

$$\epsilon_x = \frac{\int \epsilon'_x(p_T) f(p_T) p_T dp_T}{\int f(p_T) p_T dp_T}. \tag{6.26}$$

Here ϵ'_x is the efficiency obtained from embedding for all particles species and $f(p_T)$ is the function obtained by fitting the transverse momentum spectra for all energies and centralities. In case of π^+, for AuAu collision at 7.7 and 39 GeV at 0-5% centrality, p_T dependance plots have been shown in Fig 6.36. The systematic error by varying $\pm 5\%$ of the average efficiency is also included. The efficiency for positive (ϵ_+) and negative (ϵ_-) charged particles and the average efficiency (ϵ) listed in

$\sqrt{s_{\rm NN}}$(GeV)	0-5%	5-10%	10-20%	20-30%	30-40%	40-50%	50-60%	60-70%	70-80%
Positive charged particles (ϵ_+)									
62.4	0.62	0.63	0.64	0.65	0.66	0.67	0.69	0.68	0.70
39	0.62	0.64	0.65	0.66	0.67	0.67	0.68	0.70	0.71
27	0.63	0.65	0.65	0.66	0.67	0.68	0.68	0.69	0.70
19.6	0.63	0.66	0.67	0.67	0.68	0.69	0.70	0.71	0.71
11.5	0.64	0.65	0.66	0.67	0.68	0.69	0.70	0.71	0.72
7.7	0.65	0.66	0.67	0.68	0.69	0.70	0.71	0.72	0.72
Negative charged particles (ϵ_-)									
62.4	0.64	0.65	0.66	0.67	0.68	0.69	0.70	0.71	0.72
39	0.64	0.65	0.66	0.67	0.68	0.69	0.69	0.70	0.72
27	0.65	0.66	0.66	0.67	0.67	0.68	0.69	0.69	0.71
19.6	0.66	0.67	0.67	0.68	0.69	0.70	0.71	0.72	0.72
11.5	0.67	0.67	0.68	0.69	0.70	0.71	0.72	0.72	0.73
7.7	0.66	0.67	0.68	0.69	0.71	0.70	0.72	0.72	0.73
Average ($\epsilon = (\epsilon_+ + \epsilon_-)/2$)									
62.4	0.63	0.64	0.65	0.66	0.67	0.68	0.69	0.69	0.71
39	0.63	0.64	0.65	0.66	0.66	0.68	0.68	0.70	0.71
27	0.64	0.65	0.65	0.67	0.67	0.68	0.68	0.69	0.70
19.6	0.65	0.66	0.67	0.68	0.69	0.70	0.70	0.71	0.72
11.5	0.66	0.66	0.67	0.67	0.68	0.69	0.70	0.71	0.72
7.7	0.66	0.67	0.67	0.68	0.69	0.70	0.71	0.72	0.73

Table 6.5: Efficiencies for positive and negative particle for different centralities. The average efficiency (ϵ) is also listed below for different energies and centralities.

Table. 6.5.

6.6.4 Validation of efficiency correction method

To validate the efficiency correction method as discussed in Subsection 6.6.2, we assume our data is of 100% efficienct. In this case, randomly throwing particles in each centrality, we artificially introduce 80% Binomial efficiency in each centrality. Figure 6.37 shows event-by-event efficiency distribution for 0-5% centrality. As it is observed that mean of the efficiency distribution is 80%. Using this efficiency distribution, the positive (N_+) and negative (N_-) charged distributions are obtained as shown in Fig. 6.38. Due to 80% efficiency, the positive and negative charged

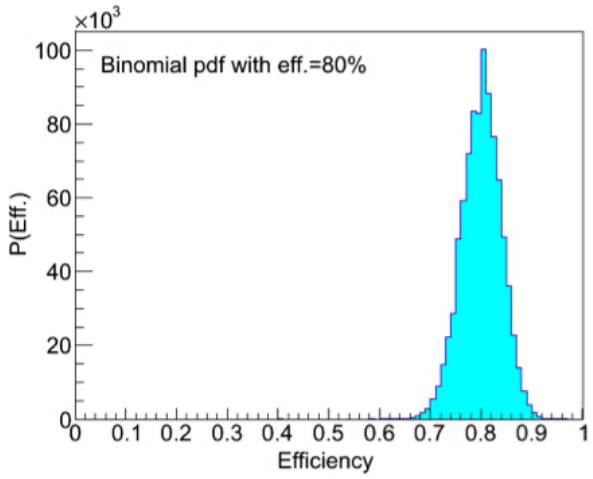

Figure 6.37: The Binomial efficiency distribution introduced in each centrality for both the positive (N_+) and negative (N_-) charged distributions for AuAu 19.6 GeV.

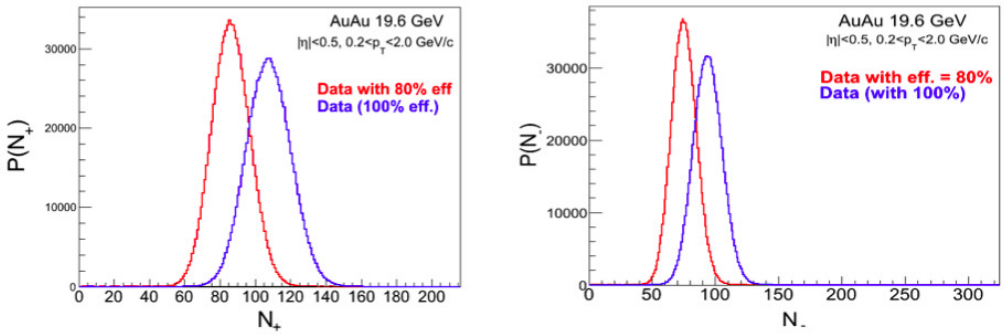

Figure 6.38: The positive (left panel) and negative (right panel) charged distribution after using 80% Binomial efficiency for AuAu 19.6 GeV at 0-5% centrality.

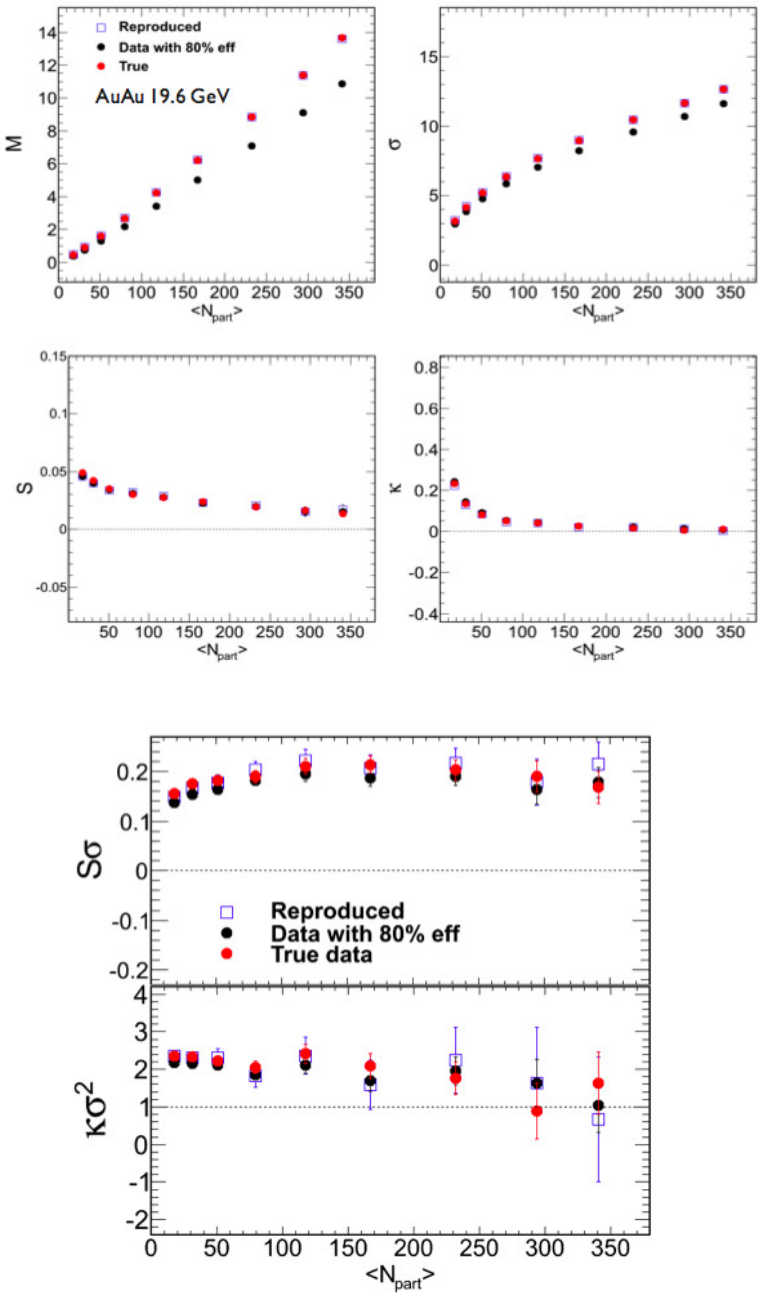

Figure 6.39: (Top panel) Various moments as a function of $\langle N_{\rm part} \rangle$. (Bottom panel) The products of moments as a function of $\langle N_{\rm part} \rangle$. Real data which is assumed to be 100%, data with artificially introduced 80% efficiency using and reproduced data after using efficiency correction method.

distribution shifts to the left. Here it can be observed that efficiency fluctuates event-by-event, whereas the mean of the Binomial distribution implies the efficiency of that centrality. So, while dealing with efficiency correction in the higher order cumulants like, c_3, c_4, etc., proper weighting should be done to avoid the efficiency fluctuation within a centrality window. It is also observed that efficiency is very much dependent on multiplicity of the event. As we see in Table. 6.5, the efficiency increases with decrease in centrality, since multiplicity decreases going from central to peripheral events. It is mainly due to tracking inefficiency in high multiplicity events.

The efficiency correction (preferring to coin multiplicity bin-by-bin efficiency correction) should be done before centrality bin width correction, with proper efficiency, to get cumulants in a given centrality. Figure 6.39 shows various moments and their products estimated for three cases, 1) the true higher moments of the data assuming 100% (red circle), 2) 80% Binomial efficiency introduced in the data (black circle) and 3) reproduced data using efficiency correction method using expression 6.14 (blue box). It is observed that using above correction method and efficiency correction expression, the true higher moments can be reproduced.

It is worthwhile to note that this correction procedure is able to reproduce true moments if the exact efficiency is known for each multiplicity. But in the STAR experiment, the efficiency is estimated from embedding for each centrality. So, the exact efficiency for each multiplicity bin is difficult to estimate. It is also good to have efficiency for each centrality multiplicity bin which can give more accurate results.

While doing efficiency correction for higher order moments, the expressions for the $5^{th}, 6^{th}...8^{th}$ moments contain large number of correction terms. This creates many problem while coding for the estimation for the statistical error by Delta Theorem. To avoid these complexity, Bootstrap method A.3 is used.

Chapter 7

Results of higher moments analysis

In this chapter, we present the final results of the analysis of the higher moments of the net-charge distributions.

7.1 Net-charge multiplicity distributions

In the heavy-ion-collisions, initially the system is in a purely baryon dominated positively charged (dominated by protons) condition. Therefore the system is expected to be of positively charged dominated in the final state. In addition to this, the event-by-event net-charge is estimated in a finite acceptance (both in pseudo-rapidity and transverse momentum range), so it is always expected to be positive mean of the net-charge distribution in a given ensemble of the events. The event-by-event net-charge ($N_+ - N_-$) distribution within $|\eta| < 0.5$ and $0.2 < p_T < 2.0$ GeV/c, are shown in Fig. 7.1. These distributions are efficiency and centrality bin width uncorrected net-charge distributions. It is observed that the width of the distribution increases with the increase of centrality. These net-charge distributions are

plotted with the Skellam distribution assuming both positive and negative charged particle distributions to be independently Poisson distributed. The expression of the Skellam distribution is given by

$$f(k;\mu_1,\mu_2) = e^{-(\mu_1+\mu_2)}(\frac{\mu_1}{\mu_2})^{k/2} I_{|k|}(2\sqrt{\mu_1\mu_2}) \tag{7.1}$$

Here μ_1 and μ_2 are the mean of the positive and negative charged particles respectively. $I_{|k|}(z)$ is the modified Bessel function of the first kind. The net-charge distribution has been plotted with respective Skellam distribution for AuAu collisions for 0-5% to 60-70% centralities, taking input as the mean of the positive and negative charge distribution for respective centrality. It shows that the Sekllam distribution qualitatively follows the net-charge distributions. Figure 7.2 shows the net–charge distributions for top central (0-5%), semi-central (30-40%) and peripheral (60-70%) collisions for $\sqrt{s}_{\rm NN}$= 7.7 to 200 GeV. It has been observed that the mean of the distributions is close to zero for high energy collisions and shifts towards positive values for lower energies. This is expected because of dominance of particles on anti-particles at low energies at mid-rapidity. The distributions are seen to be wider for higher energy collisions compared to those of the lower energies. The Skellam distribution comparisons with the different distribution shows that it closely follows the peripheral as compared to central bins (0-5%).

7.2 System size dependence

The higher moments of the net-charge distribution have been estimated for different collision geometries, like CuCu, AuAu and pp collisions. With the increase of system

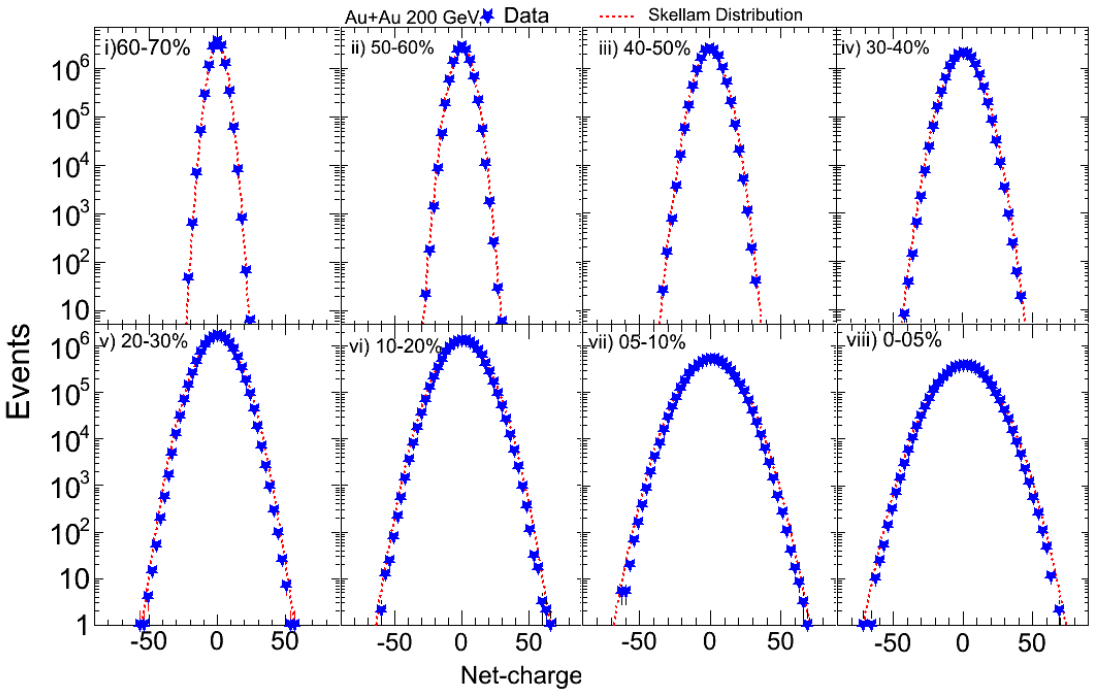

Figure 7.1: The net-charge distribution, for AuAu collisions at 200 GeV within $|\eta| < 0.5$ and $0.2 < p_T < 2.0$ GeV/c, drawn with the Skellam distribution for different centralities.

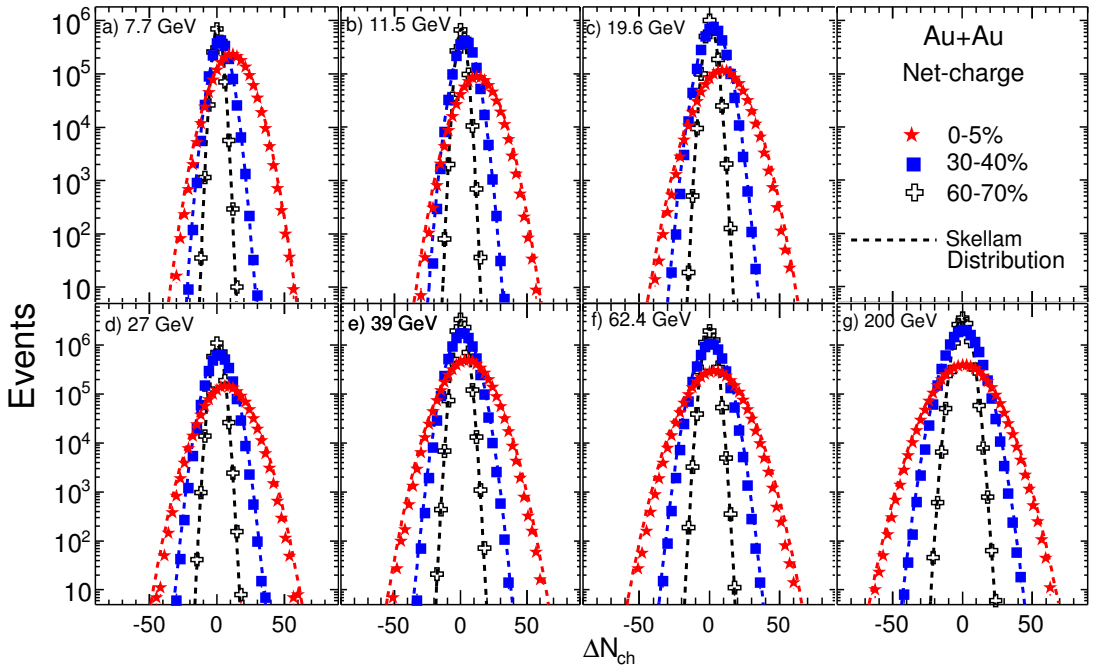

Figure 7.2: The net-charge distribution, for AuAu collisions at 7.7 to 200 GeV within $|\eta| < 0.5$ and $0.2 < p_T < 2.0$ GeV/c, drawn with the Skellam distribution for three different centralities (0-5%, 30-40%, 60-70%).

size, number of participant, N_{part}, for the collision increases and hence more energy density is produced during collision for a given colliding energy. So, it is expected that the large number of particle are produced for heavy ion collisions. On the other hand, according to CLT, with increase in N_{part}, the higher moments of the net-charge distribution tends to a *Gaussian limit* and with increase in centrality, M and σ show increasing trend whereas S and κ show decreasing trend. This behavior can be studied using different colliding geometry.

In Fig. 7.3, the centrality dependency of various moments and their products, like $\kappa\sigma^2$ and $S\sigma$, are shown for CuCu and AuAu collisions at 200 and 62.4 GeV and pp collisions for 200 GeV. M and σ increase as increasing centrality, however the trend of S and κ decrease as expected by CLT. The $S\sigma$ for CuCu collisions show relatively large values as compared to that of AuAu collisions and in case of pp collisions it is in between the CuCu and AuAu most peripheral collisions. The values of $\kappa\sigma^2$ show relatively large as compared with that of large system size. It is observed that the results of central events of CuCu collisions akin with that of AuAu collisions, whereas *pp* collisions close to peripheral collisions of AuAu and CuCu collisions.

7.3 Effect of phase space and experimental cuts

7.3.1 Effect of pseudorapidity (η) window

The total charge is conserved at full phase space in the heavy ion collisions. For a finite acceptance, the conserved charge varies event-by-event and hence gives rise event-by-event fluctuation. The charged particle multiplicity are varied by choosing different η windows. For the small η-gap, fewer charged particles are accessed, and

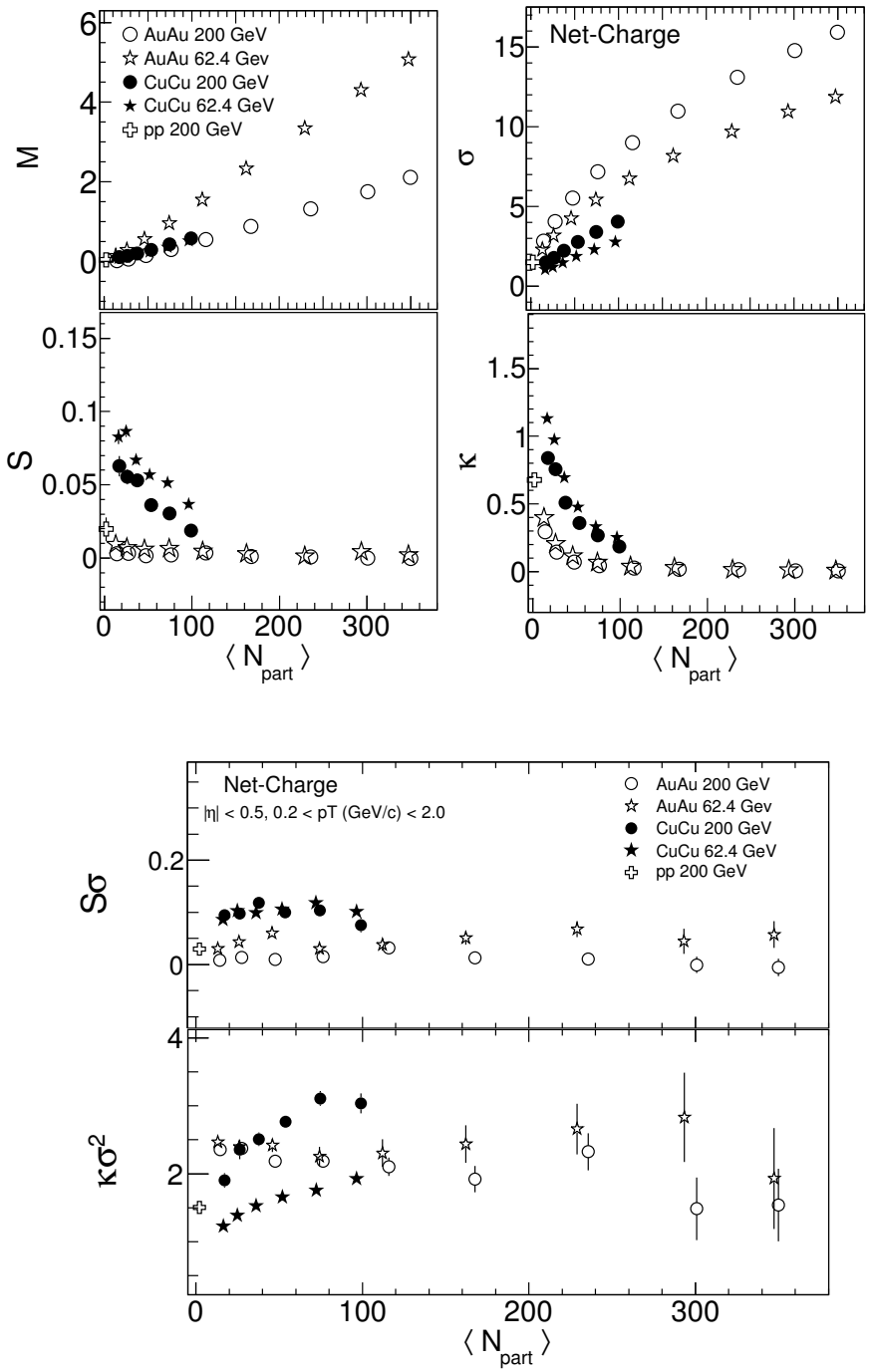

Figure 7.3: The centrality dependance of efficiency uncorrected M, σ, S, κ (upper panel) and $\kappa\sigma^2$ and $S\sigma$ (lower panel) for CuCu and AuAu collisions at 200 and 62.4 GeV and pp collisions for 200 GeV.

with increase in η-gap, more and more charged particles are accessed. To understand the evolution of the various moments of the net-charge distribution with η-gap, different η windows are chosen, -0.1 to 0.1, -0.2 to 0.2, -0.3 to 0.3, -0.4 to 0.4 and -0.5 to 0.5, for given transverse momentum region 0.2 to 2.0 GeV/c. In Fig. 7.4, M and σ are plotted for different η-gap. The M of the net-charge distribution increases with increasing η-gap and this increasing trend is observed both in the central (0-5%) and peripheral (60-70%) events. Similar increasing trend is also observed in σ for both central and peripheral events. In Fig. 7.5, the S and κ are plotted, for most central and peripheral events, as a function of different η-window. With increase in η-window, the skewness of the net-charge distribution increases both for central and peripheral events, in the contrary kurtosis decreases with increase in the η-window. The $\kappa\sigma^2$ and $S\sigma$ increases with increase in η-gap for central to peripheral events for all seven energies as shown in Fig 7.6. It is observed that due to increase in η-window, number of charged particles are increased and hence the mean of the net-charge distribution and its width also increase. With increase in multiplicity, the tail of the net-charge distribution gets skewed towards positive side. On the other hand the peakedness of the distribution decreases.

7.3.2 Effect of transverse momentum (p_T)

Large p_T windows allow to access more inclusive charged particles in a given η window and with inclusion of high p_T , more jet particles may be included which gives rise to additional fluctuation. In addition, long range fluctuation is expected to be originated from the low transverse momentum particles according to the *uncertainty principle*. The effect of different p_T windows have been studied. In Fig. 7.7, upper

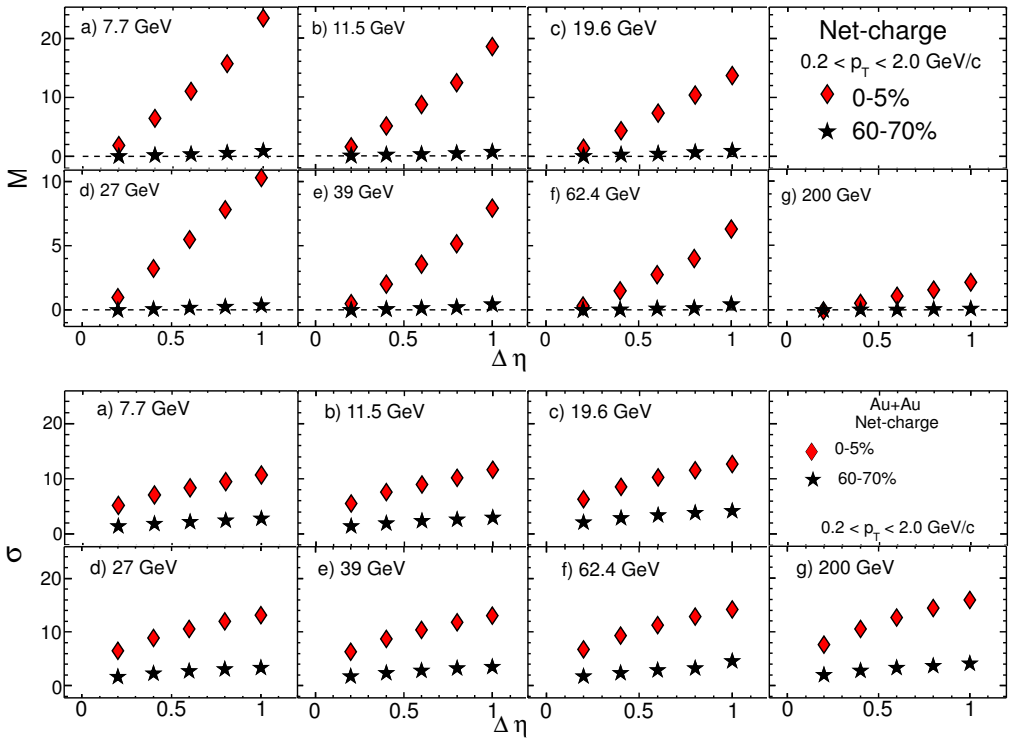

Figure 7.4: The Efficiency uncorrected M and σ are the plotted as a function of different η-window for different energies from $\sqrt{s}_{\rm NN}$=7.7 to 200 GeV at two 0-5% and 60-70% centralities.

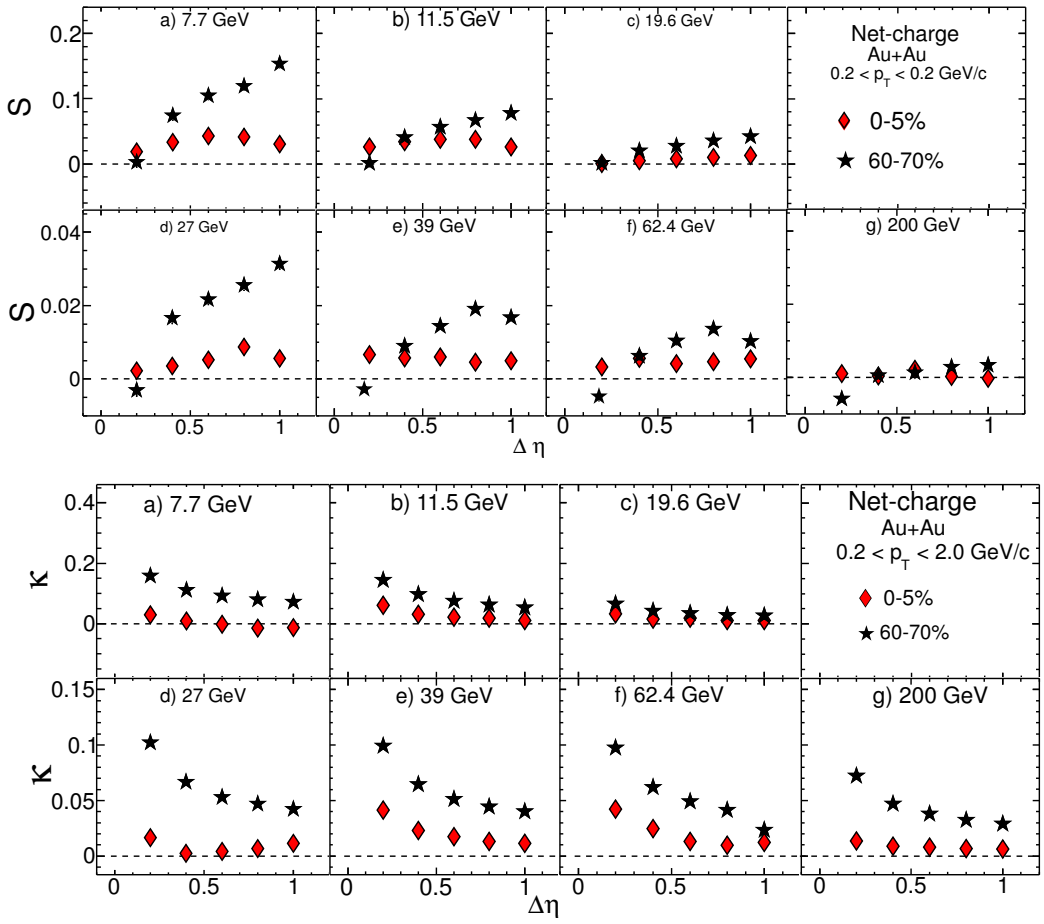

Figure 7.5: The efficiency uncorrected S and κ are the plotted for different energies as a function of different η-window from $\sqrt{s}_{\rm NN}$=7.7 to 200 GeV at two 0-5% and 60-70% centralities.

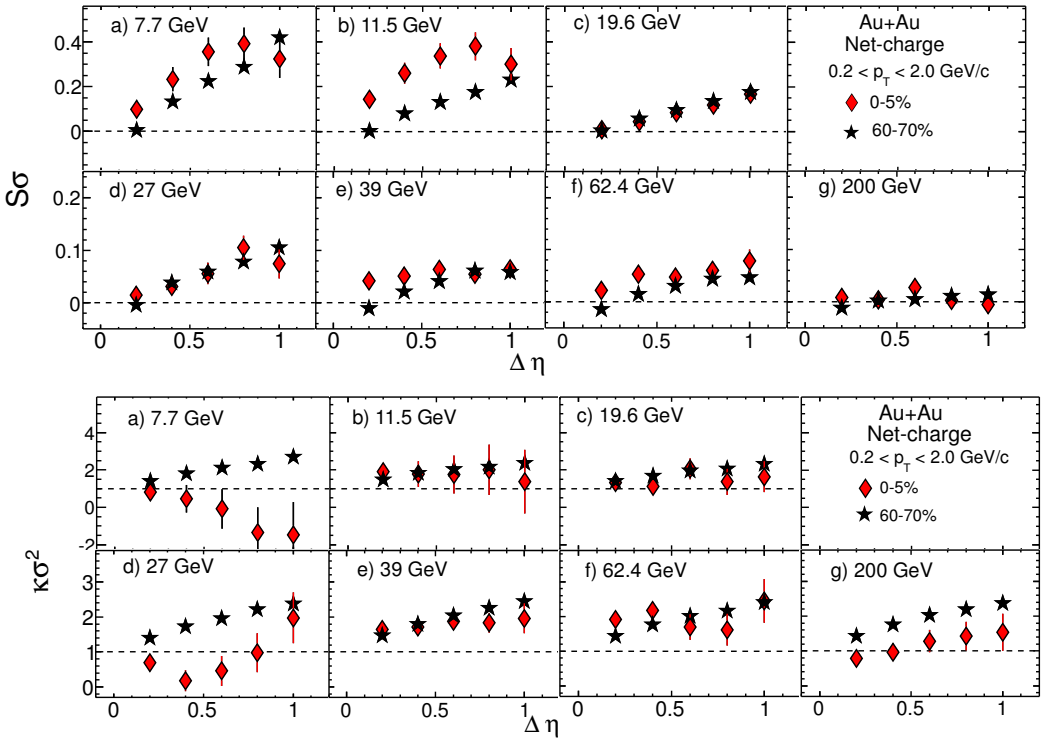

Figure 7.6: The efficiency uncorrected $S\sigma$ and $\kappa\sigma^2$ are the plotted for different energies as a function of different η-window from $\sqrt{s}_{\rm NN}$=7.7 to 200 GeV at two 0-5% and 60-70% centralities.

p_T ($p_{T max}$) cuts are varied for the estimation of the moments at $|\eta| < 0.5$. The M and σ are observed to increases with $p_{T max}$ up-to 2.0 GeV/c and gets saturated above it for all centralities (top central and peripheral events have been shown only) and for all colliding energies. The values of S increases, whereas the values of κ decreases with increase in $p_{T max}$ and gets saturated above $p_{T max}$ = 2.0 GeV/c for both cases, as shown in Fig. 7.8.

In Fig. 7.9, the $\kappa\sigma^2$ and $S\sigma$ are plotted for different $p_{T max}$ for 0-5% and 60-70% centralities. Both the observables show increasing trend and then above $p_{T max}$ =2.0 GeV/c saturation effects are observed for all colliding energies. The thermal particles may carry more information about the underlying physics as compared to hard particles ($p_T > 2.0$ GeV/c).

7.3.3 Effect of changing the track quality cuts

In the STAR TPC, the charged particles are tracked by using number of hit information in each pad of a sector. The maximum number of hits, for a track is 45, so for the analysis it can be varied for different track fit points. For good quality tracks one can use large values of fit points but it decreases the number of charged particle multiplicity of an event. So, to understand the effect of fit points for the present analysis, the charged particles are counted for different fit points at $|\eta| < 0.5$ and $0.2 < p_T < 2.0$ GeV/c. In Fig 7.10, the various moments M, σ, S and κ, and their products like, $\kappa\sigma^2$ and $S\sigma$, are plotted as a function of different track fitting points for 0-10% central events. It is observed that these various moments of the net-charge distribution and their products show negligible effect within fit points 10 to 28 points. For the complete analysis, number of fit points 20 is used throughout

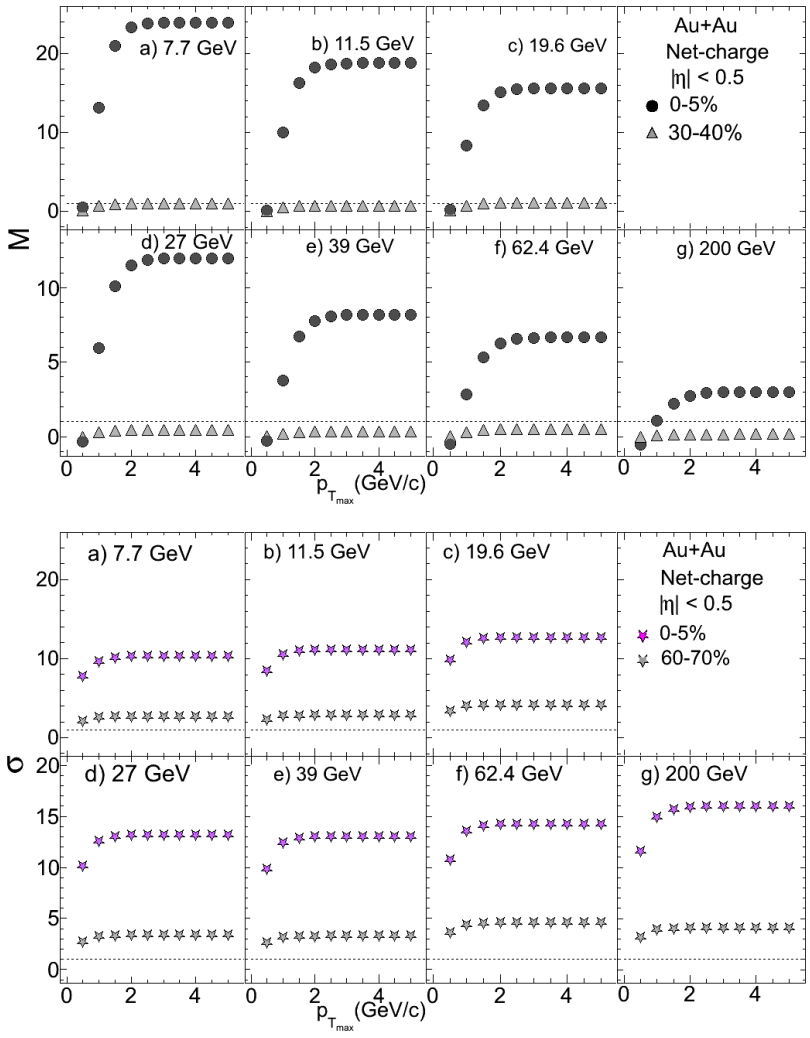

Figure 7.7: The maximum p_T cut-off dependency of efficiency uncorrected M and σ are the plotted for different energies from $\sqrt{s}_{\rm NN}$=7.7 to 200 GeV at two 0-5% and 60-70% centralities.

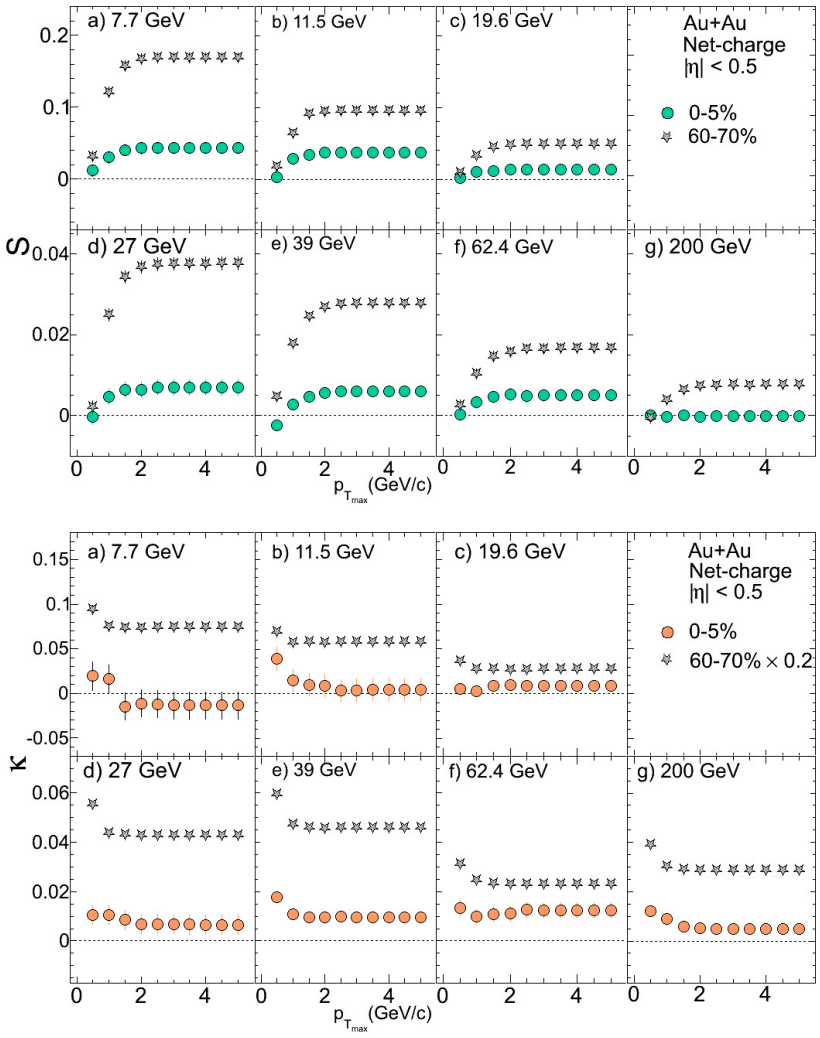

Figure 7.8: The maximum p_T cut-off dependency of efficiency uncorrected S and κ are the plotted for different energies from $\sqrt{s}_{\rm NN}$=7.7 to 200 GeV at two 0-5% and 60-70% centralities.

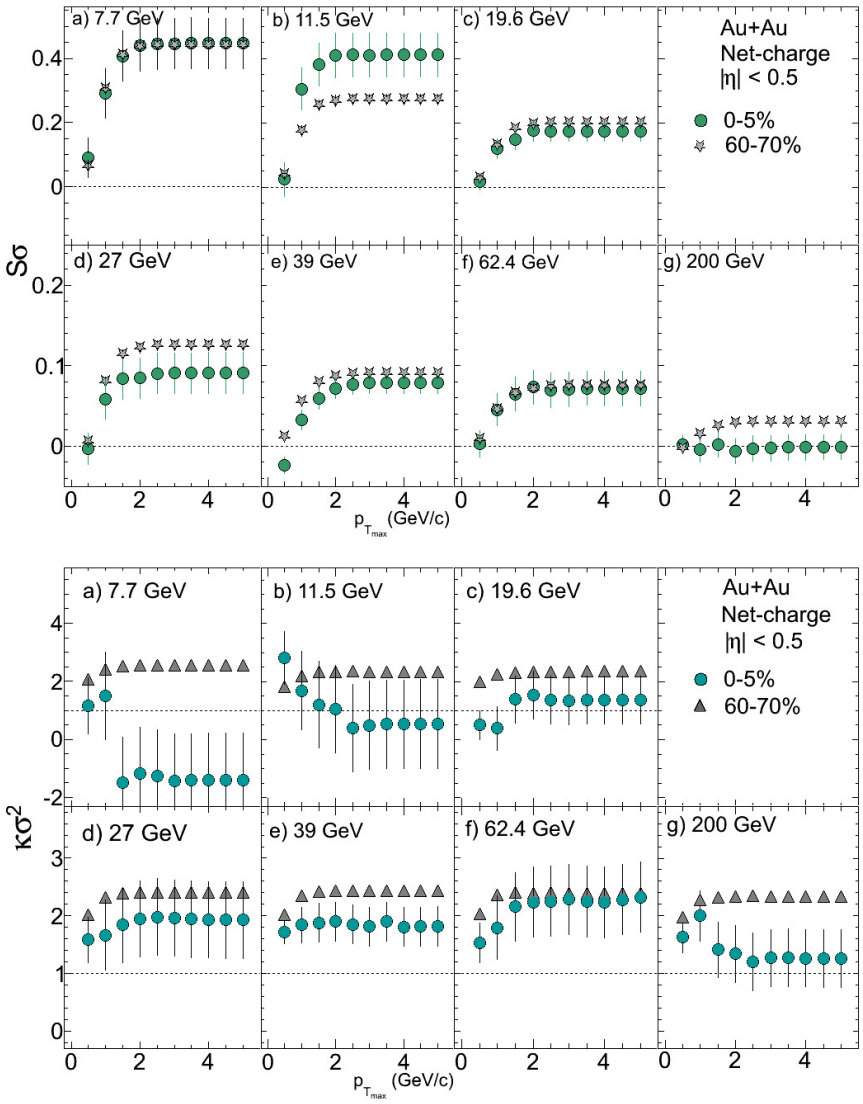

Figure 7.9: The maximum p_T cut-off dependency of efficiency uncorrected $S\sigma$ and $\kappa\sigma^2$ are the plotted for different energies from $\sqrt{s}_{\rm NN}$=7.7 to 200 GeV at two 0-5% and 60-70% centralities.

the analysis.

Each charged particle track is projected to primary vertices in the STAR TPC. The distance of closest approach (DCA) from the primary vertex for each track can be varied from 0 to 3 cm. In Fig 7.11, the moments M, σ, S and κ, and their products, $\kappa\sigma^2$ and $S\sigma$, are plotted as a function of DCA for 0-10% central events. There is small DCA dependency is observed.

7.4 Various moments and their products

Centrality dependency of the M, σ, S, κ for the net-charge distributions are extracted for Au+Au collisions at all seven colliding energies. In Fig. 7.12, the first four efficiency uncorrected moments of the net-charge distributions are plotted in terms $\langle N_{\rm part} \rangle$ for all colliding energies. Similarly, in Fig. 7.13 that for efficiency corrected results are plotted. The statistical errors dominate in most cases since the systematic errors are within symbol size. For all the colliding energies, we observe that the M and σ values increase from peripheral to central collisions, whereas S and κ values decrease with increasing N_{part}. The centrality dependence of the moments can be understood by the central limit theorem (CLT), which assumes that each of the collisions is a collection of a finite number of identical, independent emission sources. Under this assumption, $\langle N_{\rm part} \rangle$ can be considered a proxy for the volume of the colliding system at a given centrality. The resulting CLT curves are superimposed on the data points in Fig. 7.12 and 7.13. The χ^2/ndf values, for the CLT fitting are found to be below 1.5, 1.0, 1.6 and 2.0, in case of M, σ, S and κ, respectively. Thus, the centrality dependence of the moments at a given energy follows the general expectations form of CLT, indicating that the moments depend

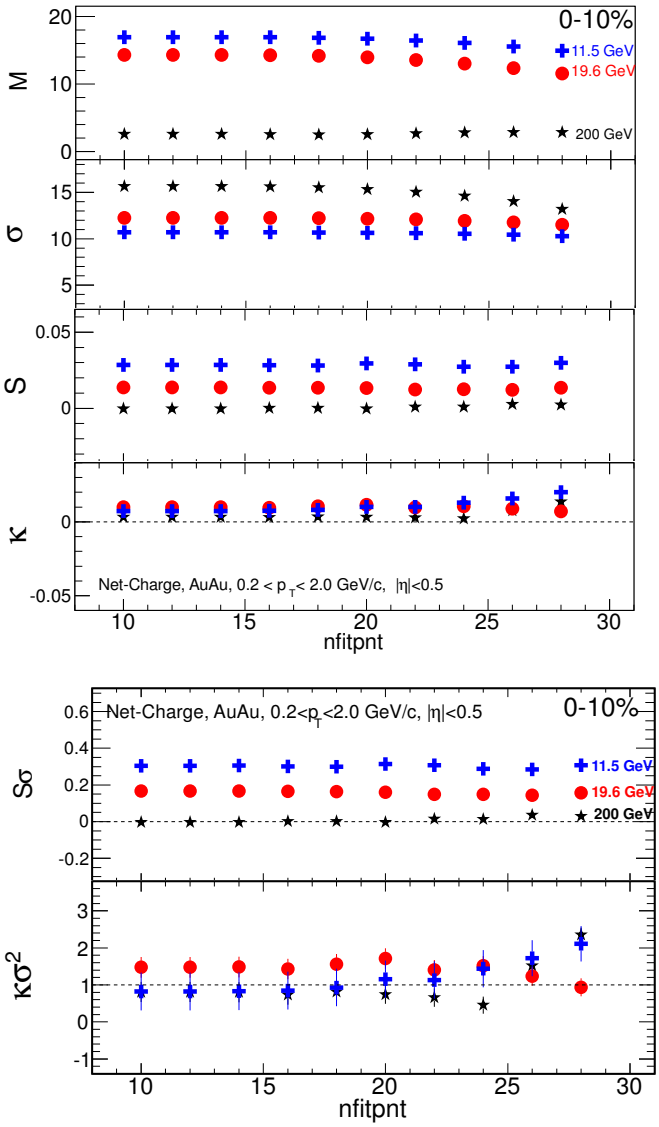

Figure 7.10: (Top panel) Various moments and (bottom panel) their products are the plotted as a function of number of fit points at AuAu collisions for $\sqrt{s}_{\rm NN}$=11.5, 19.6 and 200 GeV for 0-10% centrality.

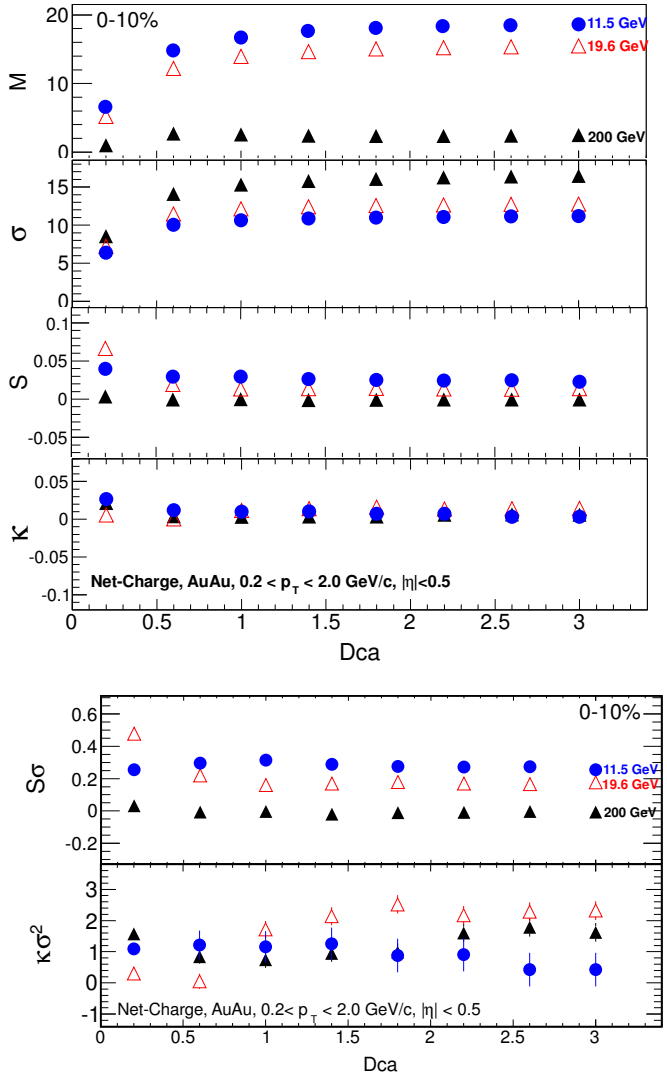

Figure 7.11: (Top panel) Various moments and (bottom panel) their products are the plotted as a function of DCA at AuAu collisions for $\sqrt{s}_{\rm NN}$=11.5, 19.6 and 200 GeV for 0-10% centrality.

on the system volume. This is one of the reasons to construct different combinations of moments, which removes the volume dependences.

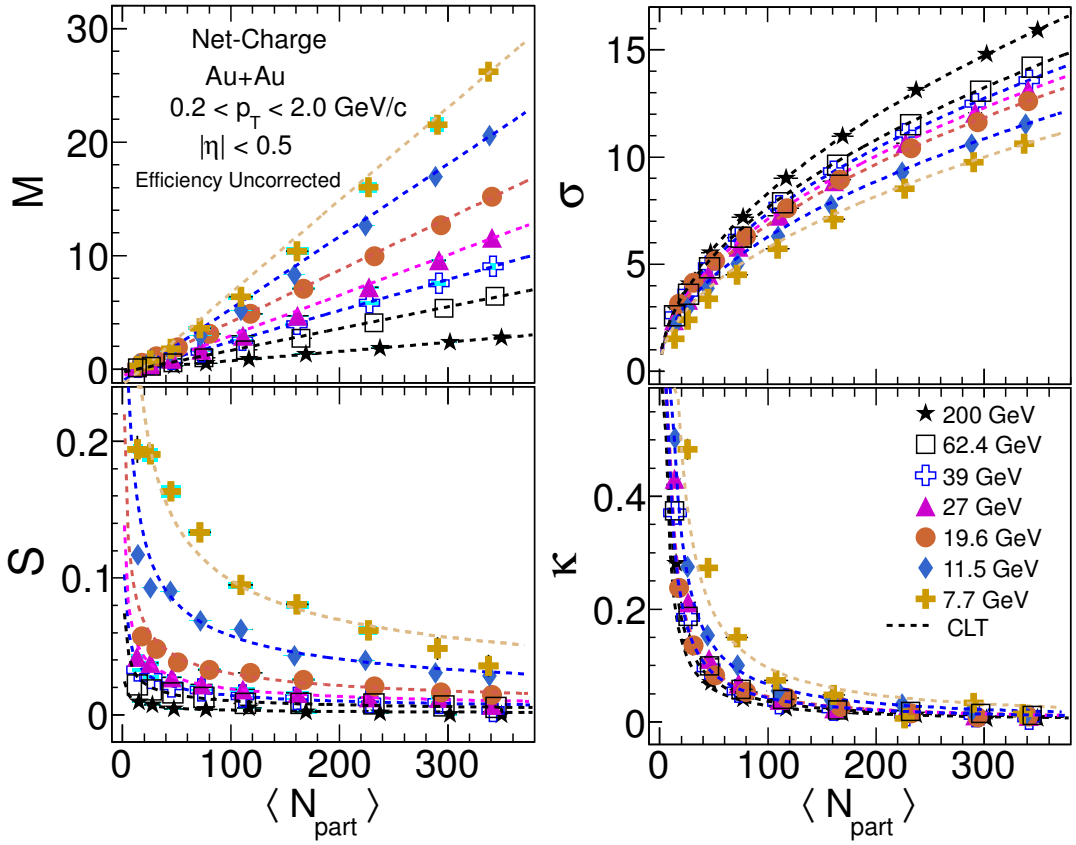

Figure 7.12: The efficiency uncorrected centrality dependency of various moments, such as M, σ, S and κ are the plotted for different energies from $\sqrt{s}_{\rm NN}$=7.7 to 200 GeV. The dotted lines represents central limit theorem fitted for different colliding energies.

Figure 7.14 shows both the efficiency uncorrected and corrected values of $S\sigma$ plotted as a function of $\langle N_{\rm part}\rangle$ for Au+Au collisions at each of the colliding energies. In general, $S\sigma$ values are observed to decrease with increasing beam energy. The efficiency corrected $S\sigma$ values show little higher as compared to that of uncorrected

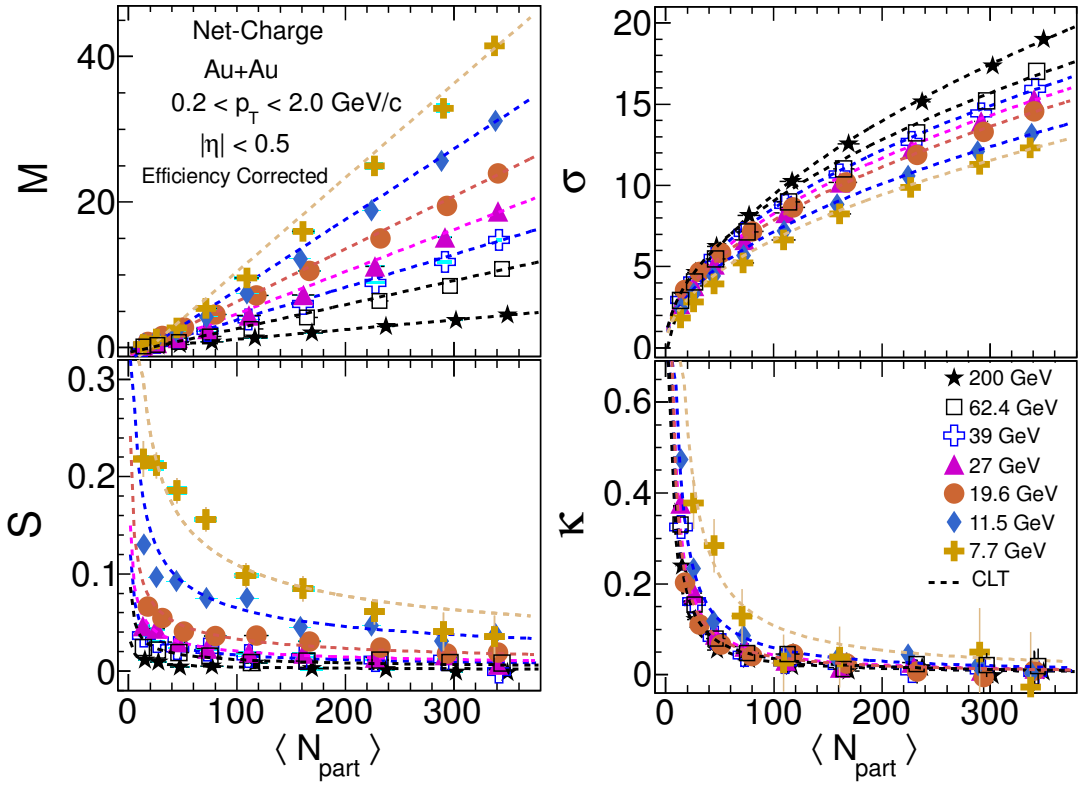

Figure 7.13: The efficiency corrected centrality dependency of various moments, such as M, σ, S and κ are the plotted for different energies from $\sqrt{s}_{\rm NN}$=7.7 to 200 GeV. The dotted lines represents central limit theorem fitted for different colliding energies.

one. To understand the baseline for this product, expectations from Poisson statistics and NBD baseline are studied. In this approach, the distributions for positive and negative charged particles are assumed to follow Poisson and NBD statistics without any dynamical correlations. The moments of the net-charge distributions are then constructed using the mean values of the positive and negative charged particle distributions for Poisson baseline. For NBD, both mean and variance of positive and negative charged distributions are used. Details about the estimation for the Poisson and NBD baseline can be found in Section 5.3 and 5.4, respectively. For collisions at $\sqrt{s}_{\rm NN}$=200 GeV the data points agree well with the Poisson expectations. For all other energies, deviations from Poisson expectations are observed, and these deviations increase with the decrease of beam energy. The efficiency uncorrected NBD expectations are also plotted for different beam energies as shown in Fig. 7.14. The NBD expectations are close to $S\sigma$ for all centralities.

Figure 7.15 shows both the efficiency uncorrected and corrected values of $\kappa\sigma^2$ as a function of $\langle N_{\rm part}\rangle$ for Au+Au collisions at each of the colliding energies. Both the statistical and systematic errors are indicated in figure. The efficiency corrected $S\sigma$ shows little higher values as compared to that of uncorrected one. The expectation from Poisson statistics for all cases are constant at unity, which are shown by dotted lines. The efficiency uncorrected NBD expectations are also plotted for different beam energies. Within the statistical uncertainties, the values of $\kappa\sigma^2$ are above the Poisson expectations, with the exceptions of central collisions at lowest energy.

The centrality dependency of both the efficiency uncorrected and corrected $\frac{\sigma^2}{M}$ for seven energies are plotted in Fig. 7.16. At a given colliding energies, the $\frac{\sigma^2}{M}$ decreases goes from peripheral to central events. The $\frac{\sigma^2}{M}$ increases with decrease

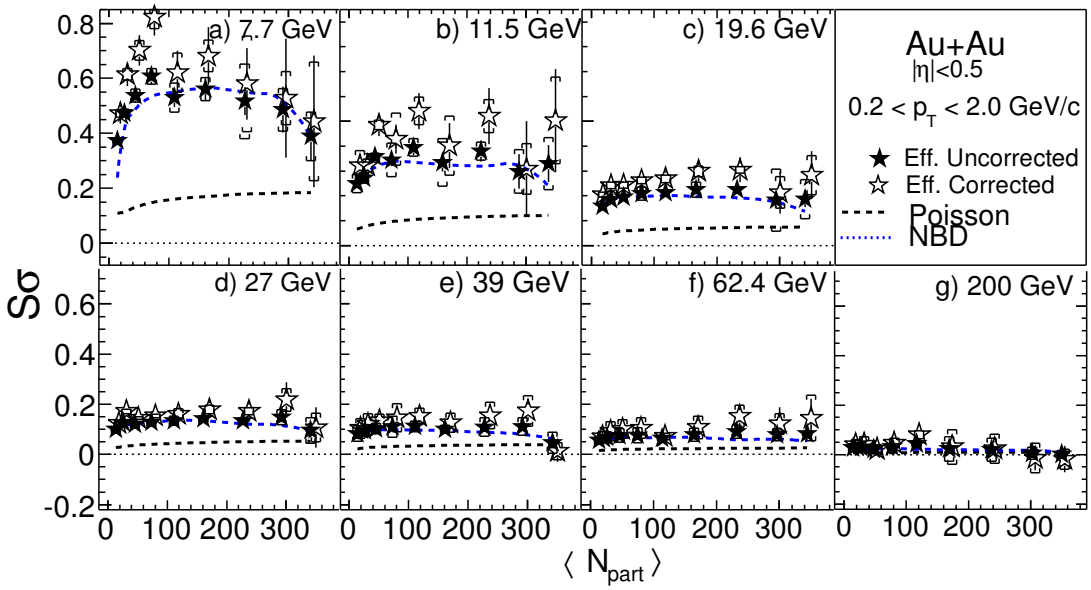

Figure 7.14: The centrality dependency of $S\sigma$ is the plotted for different energies from $\sqrt{s}_{\rm NN}$=7.7 to 200 GeV. The filled and open star represent efficiency corrected and uncorrected $S\sigma$ results, respectively. The dotted and blue dashed lines represent the Poisson expectations and NBD expectation for different colliding energies. The vertical lines represent the statistical error bar and caps represent systematic error.

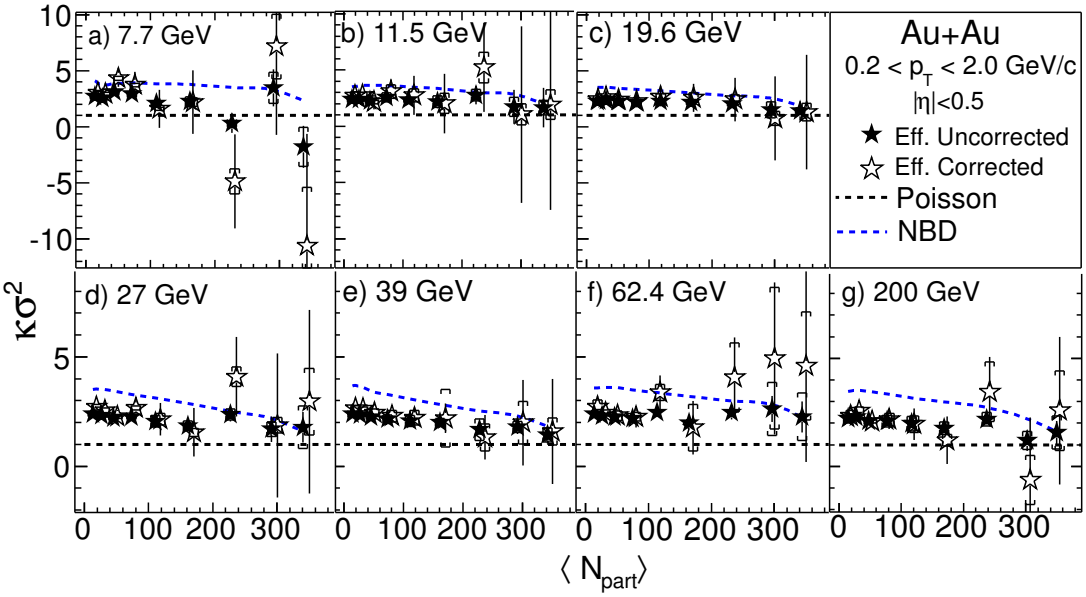

Figure 7.15: The centrality dependency of $\kappa\sigma^2$ is the plotted for different energies from $\sqrt{s}_{\rm NN}$=7.7 to 200 GeV. The filled and open star represent efficiency corrected and uncorrected $\kappa\sigma^2$ results, respectively. The dotted and blue dashed lines represent the Poisson expectations and NBD expectation for different colliding energies. The vertical lines represent the statistical error bar and caps represent systematic error.

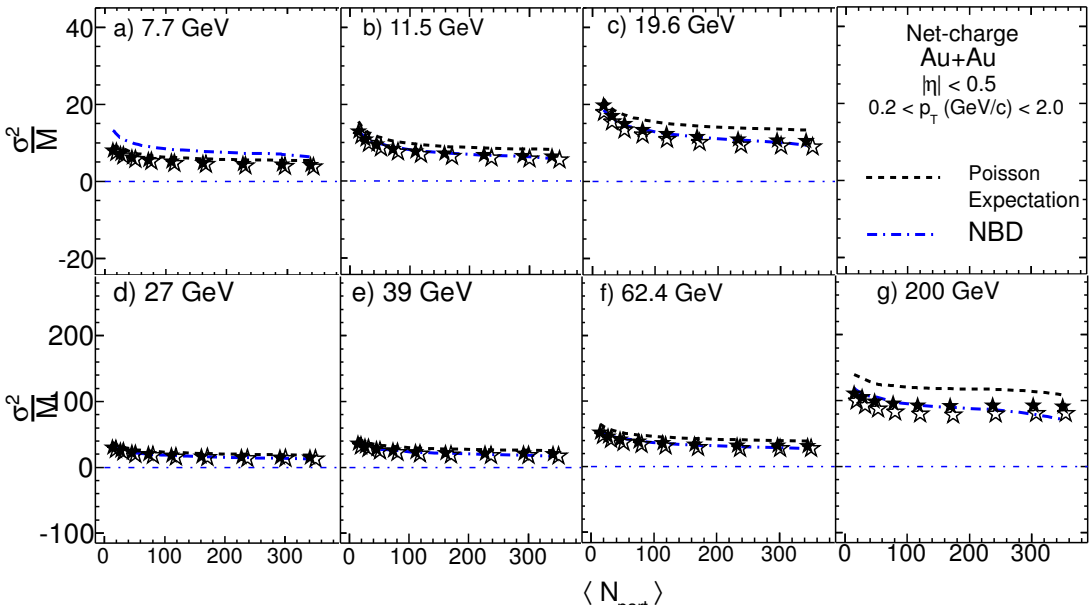

Figure 7.16: The centrality dependency of $\frac{\sigma^2}{M}$ is the plotted for different energies from $\sqrt{s}_{\rm NN}$=7.7 to 200 GeV. The filled and open star represent efficiency corrected and uncorrected $\kappa\sigma^2$ results, respectively. The black dotted and blue dashed lines represent the Poisson expectations and NBD expectation for different colliding energies. The systematic and statistical error are within marker size.

in colliding energies. It implies that with increase in beam energies the net-charge fluctuation ($\frac{\sigma^2}{M}$) increases. The efficiency corrected values of $\frac{\sigma^2}{M}$ show smaller values than that of uncorrected one. In addition, the Poisson and efficiency uncorrected NBD expectation are also plotted in Fig. 7.16. Both expectations show similar centrality dependency behavior. The NBD expectations show larger than that of Poisson for all centralities and beam energies. Figure 7.17 shows the beam-energy

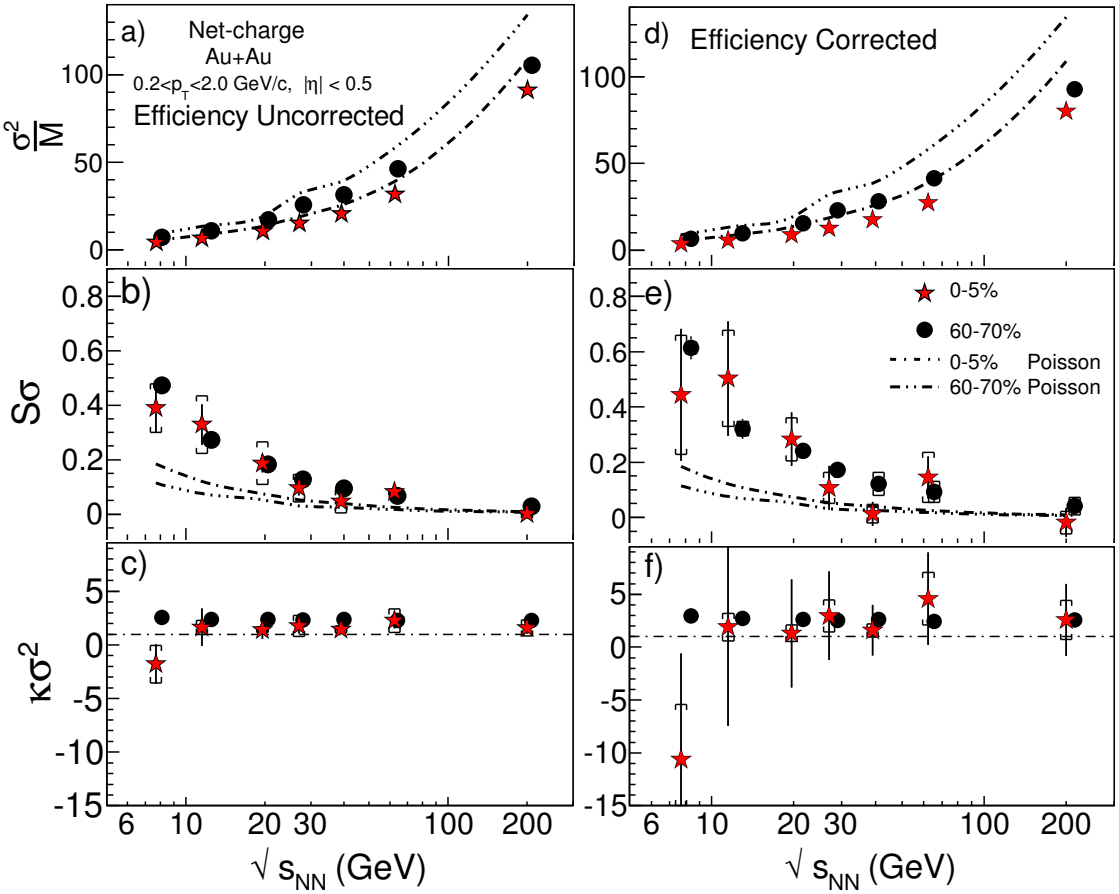

Figure 7.17: The beam energy dependency of $\frac{\sigma^2}{M}$, $S\sigma$ and $\kappa\sigma^2$ are the plotted for three centralities. The dotted lines represents the Poisson expectations for different colliding energies. The blue dashed line represents HRG model predictions. The vertical lines represent the statistical error bar and caps represent systematic error.

dependence of $\frac{\sigma^2}{M}$, $S\sigma$ and $\kappa\sigma^2$, for two centrality bins, *viz.*, 0-5%, and 60-70% of the total cross section for efficiency corrected and uncorrected results. Both the statistical and systematic errors are plotted. The results from Poisson expectations is superimposed on the experimental data points. The values $\frac{\sigma^2}{M}$ are observed to increase with increasing beam energy. At all energies, $\frac{\sigma^2}{M}$shows lower values than that of Poisson expectation as shown in the top panel of the figures (a) and (d). The middle panel of the figures, (b) and (e), show the values of $S\sigma$, which are close to zero for $\sqrt{s}_{\rm NN}$=200 GeV and increase with decreasing beam energy for all thwo centralities. The energy dependence of $S\sigma$ shows systematically large deviations (with significance of deviation larger than 2.0) from that of Poisson expectations below $\sqrt{s}_{\rm NN}$=27 GeV compared to those at higher energies. The bottom panel of the figures, (c) and (f), show $\kappa\sigma^2$as a function of beam energy. For the non-central collisions, these values show no energy dependence. Also for central collision, no energy dependence is observed, excluding the lowest energy.

7.5 Extraction of freeze-out parameters

The experimentally measured higher order moments, $\frac{S\sigma^3}{M}$ and $\frac{M}{\sigma^2}$, can be used to extract freeze-out parameter by comparing lattice QCD results as discussed in Section 1.5. The beam energy dependance of efficiency corrected $\frac{S\sigma^3}{M}$ and $\frac{M}{\sigma^2}$ are shown in Fig. 7.18. The values of $\frac{S\sigma^3}{M}$ are close to ∼2 for $\sqrt{s}_{\rm NN}$= 7.7 to 62.4 GeV with statistical uncertainty whereas for $\sqrt{s}_{\rm NN}$= 200 GeV, it is close to ∼0.3 with large statistical uncertainty. In Table. 7.1 and 7.2, the values of $\frac{S\sigma^3}{M}$ and $\frac{M}{\sigma^2}$, are listed, respectively, for different energy. The Lattice QCD estimation of $R^Q{}_{31}$ for freeze-out temperature, T_f = 150-190 MeV, is shown in shaded region in Fig. 7.18. The values

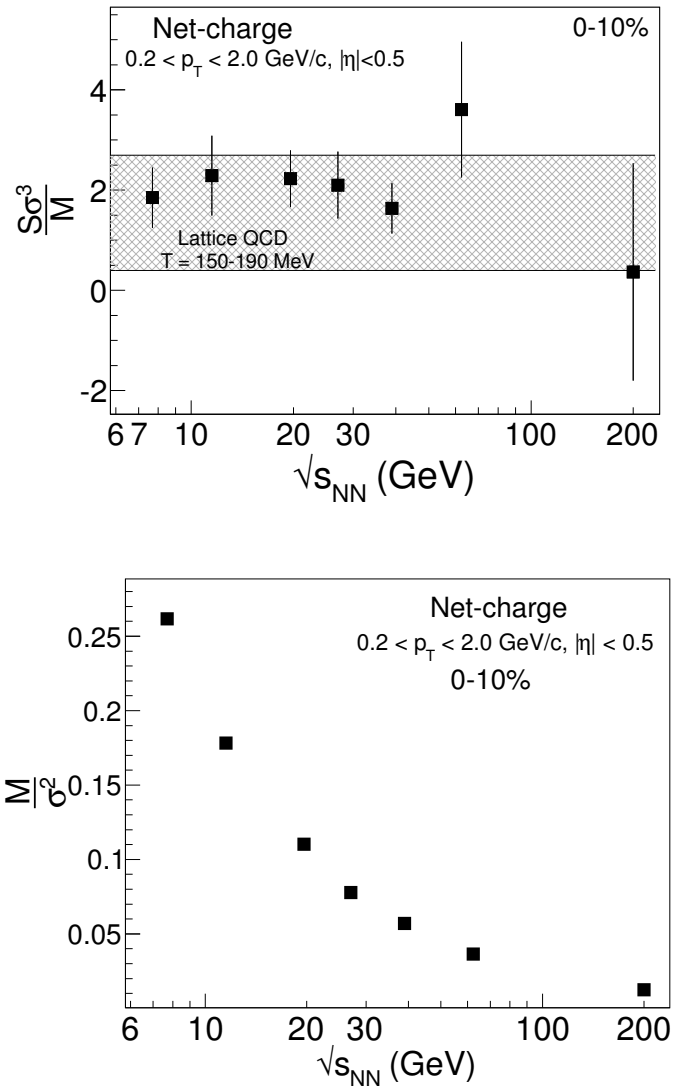

Figure 7.18: (Top panel) The beam energy dependance of efficiency corrected $\frac{S\sigma^3}{M}$ for Au+Au Collisions at 0-10% centrality (for $\sqrt{s}_{\rm NN}$= 200 GeV, 0-17% centrality has been taken to avoid large statistical error with negative value). The $\frac{S\sigma^3}{M}$ is related to $R^Q{}_{31}$ of net-charge in lattice QCD calculation. The shaded region represents lattice QCD estimation region of $R^Q{}_{31}$. (Bottom panel) The beam energy dependance of efficiency corrected $\frac{M}{\sigma^2}$ for Au+Au Collisions at 0-10% centrality (for $\sqrt{s}_{\rm NN}$= 200 GeV, 0-17% centrality has been taken). The $\frac{M}{\sigma^2}$ is related to $R^Q{}_{12}$ of net-charge in lattice QCD calculation.

of $\frac{M}{\sigma^2}$ increase with decrease in colliding energy. It implies, that with the increase in colliding energy baryon chemical potential, μ_{Bf}, decreases at freeze-out surface. The exact value of μ_{Bf} can be estimated by knowing exact T_f at given colliding energy. The large statistics is required to reduce the statistical uncertainties in $\frac{S\sigma^3}{M}$.

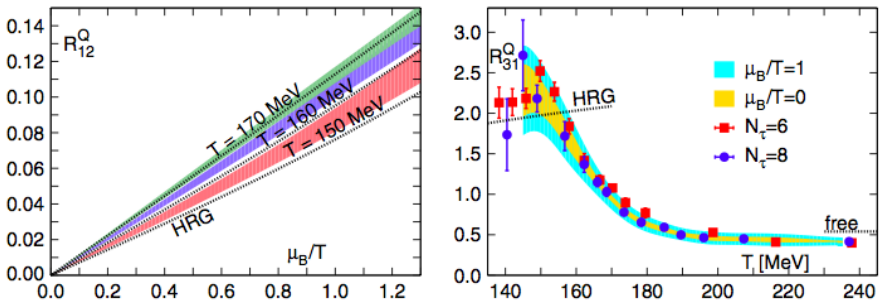

Figure 7.19: Diagrammatic representation of two limiting cases of Binomial distribution [41].

Table 7.1: The values of $R^Q{}_{31}$ and corresponding T_f for different energies are listed below. All these values are estimated for 0-10% centrality whereas 0-17% for $\sqrt{s}_{\rm NN}$= 200 GeV. *T_f are taken from the Fig.7.19 and [79].

	$\sqrt{s}_{\rm NN}$ (GeV)	$R^Q{}_{31} = \frac{S\sigma^3}{M}$	T_f (MeV)
AuAu	200	0.370±2.168	>160
	62.4	3.512±1.353	-
	39	1.637±0.500	∼140-160
	27	2.099±0.66	
	19.6	2.229±0.56	
	11.5	2.290±0.710	
	7.7	1.849±0.790	

Table 7.2: The values of $R^{Q}{}_{12}$ and corresponding μ_B/T for different energies are listed below. All these values are estimated for 0-10% centrality whereas 0-17% for $\sqrt{s}_{\rm NN}$= 200 GeV. *μ_B/T are taken from the Fig.7.19 and [79].

	$\sqrt{\mathbf{s}}_{\rm NN}$ (GeV)	$R^{Q}{}_{12} = \frac{M}{\sigma^3}$	μ_B/T
AuAu	200	0.0125±1.6e-04	∼0.15
	62.4	0.036± 6.19e-04	∼0.35-0.43
	39	0.056±5.4e-04	∼0.56-0.72
	27	0.077±1.3e-04	∼0.8-1.3
	19.6	0.110±1.4e-04	∼1.1-1.2
	11.5	0.178±3.6e-04	-
	7.7	0.261±1.6e-03	-

Chapter 8

Summary

Prime aim of the RHIC beam energy scan program is to map the QCD phase diagram and to search for the location of critical point. To achieve these goals, the STAR experiment has collected data for Au+Au collisions at 7.7, 11.5, 19.6, 27, 39, 62.4 and 200 GeV, in the year 2010 and 2011. STAR experiment has unique advantages with full 2π coverage in azimuth, and uniform η *vs* p_T acceptance. This program covers baryon chemical potential, μ_B, from 20-410 MeV in the QCD phase diagram. All these make the STAR experiment one of the unique detector system in the world to search for the QCD critical point.

Lattice QCD calculations have proposed that the higher order moments such as variance (σ^2), skewness (S) and kurtosis (κ), discussed in Section 4.1, of the conserved charges (X = Q, B, and S) are related to respective higher order susceptibilities. At the critical points, the higher order susceptibilities of the conserved charges diverge. Therefore, the higher order moments of the conserved charge distribution as a function of beam energy, could show non-monotonic behavior at the

critical point. Various suitable moments products, such as $\frac{\sigma^2}{M}$, $S\sigma$ and $\kappa\sigma^2$, are constructed to cancel the volume in the susceptibilities of the conserved charges. This thesis work covers the higher moments of net-charge distribution at RHIC energies. In order to understand the effect of background physics, like jet production, jet-quenching, resonance production, baryon stopping, and thermal equllibrium etc., on the higher moments of the net-charge distribution, various models, like HIJING, UrQMD, THERMINATOR, are studied. These model predictions set baseline for the analysis. Besides these, independent Poisson and Negative Binomial assumptions for the positive and negative charged particles distribution have also been studied. In these cases, the results set the baseline from the non-dynamical (or statistical) origin.

For the estimation of higher moments of the net-charge distribution, extensive data clean up processes have been performed. Centrality bin width correction has been done to avoid centrality bin width effect. To avoid auto-correlation effect in the higher moments of the net-charge distribution, new centrality definition is chosen. In these cases, the uncorrected charged particles are selected outside the analysis η-window. To validate these new centrality selection, extensive Monte Carlo simulation has been performed. Besides these, extensive study on various types of statistical error estimation have been performed. Amongst them Booststrap and Delta theorem have been proved to be robust method for the statistical error estimation for higher moments analysis. The efficiency correction for these higher moments are also done by taking Binomial efficiency in the analysis. The efficiency for all beam energies are also estimated from the STAR embedding data.

The mean and width of net-charge distributions increases with increase in centrality and also with the increase in beam energy. The skewness and kurtosis of the distributions decrease with increasing centrality. The centrality evolution of these higher order moments follow the trend of the Central Limit Theorem. The products of moments are studied to cancel the volume dependance in the higher moments of the net-charge distribution. The $\frac{\sigma^2}{M}$ shows decreasing trend by increasing centrality, whereas $S\sigma$ and $\kappa\sigma^2$ show negligible centrality dependence within the statistical uncertainty. The values of $\frac{\sigma^2}{M}$ are observed to increase with increasing beam energy. At all energies, $\frac{\sigma^2}{M}$ shows lower values than that of Poisson expectation. The values of $S\sigma$, which are close to zero for $\sqrt{s}_{\rm NN}$=200 GeV and increase with decreasing beam energy for all centralities. The energy dependence of $S\sigma$ shows systematically large deviations from that of Poisson expectations below $\sqrt{s}_{\rm NN}$=27 GeV compared to those at higher energies. The values of $\kappa\sigma^2$as a function of beam energy show no energy dependence for the non-central collisions. For central collision, no energy dependence is observed excluding at lowest energy $\sqrt{s}_{\rm NN}$= 7.7 GeV. For the extraction of the freeze-out parameters (T_f and μ_{Bf}) the combinations of $\frac{S\sigma^3}{M}$ and $\frac{M}{\sigma^2}$ have beed studied for 0-10% central events. The values of $\frac{S\sigma^3}{M}$, from the 7.7 to 200 GeV, lie between the values ∼3 to 0.36. These values imply T_f = 150 to 190 MeV by comparing with lattice QCD calculation. By comparing lattice QCD calculation with experimental measured $\frac{M}{\sigma^2}$, it is observed that values of the μ_{Bf} are between 16 to 210 MeV (with statistical uncertainties) for 200 to 19.6 GeV beam energies.

Chapter 9

Outlook

The RHIC beam energy scan results for the higher moments of net-charge distributions have been discussed in the above sections. The prime aim of this higher moments analysis is to probe the QCD critical point in the phase diagram. This analysis is very much affected by the statistical uncertainty. The width of the net-charge distribution is quite large as compared to other conserved charge distribution, like net-proton and net-kaon. It is very important to have large statistics to conclude about the results of the net-charge higher moments. In RHIC, it has been proposed the beam energy scan phase-II program to take large collection of data at low energies. In addition to this, an additional colliding energy at $\sqrt{s}_{\rm NN}$= 15 GeV has also been proposed. Besides these, STAR experiment has also proposed to upgrade inner-sector of STAR Time Projection Chamber (iTPC) for BES-II program. This upgrade provide the effective $|\eta|$ <1.7 unit, better momentum resolution, and better dE/dx resolution in STAR TPC. Therefore, the forthcoming BES-II program with large statistics data, large acceptance and better momentum resolution could give clear and robust results on the QCD critical point in phase diagram.

On the other-hand, recently the lattice QCD simulation [41, 42] suggests to extract the freeze-out parameters like T_f and μ_f, from the experimentally measured net-charge higher moments without using phenomenological models. Whereas the statistical thermalization model describes the freeze-out parameters quite well. Lattice QCD calculation calculation reveals the signature of critical point in QCD phase diagram, so it is necessary to put a phase boundary line estimated from the lattice QCD calculation. In this approach, M/σ^2 (χ_1/χ_2) shows dependence on μ_B, hence it is considered as *baryo-meter* — which can be used to get the freeze-out baryon chemical potential. The $S\sigma^3/M$ (χ_{13}/χ_1) shows no dependance on baryon chemical potential in leading order rather dependent on temperature, hence it can be used as *thermo-meter* at a given baryon chemical potential. These two observable for the net-charge distribution can be used for the freeze-out parameters. In this case, it is assumed that all the charged particles freeze-out at same time and hence its susceptibilities (χ) carry the information at the freeze-out. So, the higher moments of the net-charge distribution can serve as tool to estimate the freeze-out parameters by comparing lattice QCD results in the heavy-ion-collisions.

Bibliography

[1] F. Halzen and A. D. Martin, *QUARKS & LEPTONS: An Introductory Course in Modern Particle Physics*.

[2] Siegfried Bethke, Experimental Tests of Asymptotic Freedom, arXiv:hep-ex/0606035.

[3] J.C. Collins and M.J. Perry, Phys. Rev. Lett. 34 (1975) 1353.

[4] J. Adams et al. Nucl. Phys. A 757,102 (2005).

[5] H. M. Ortmanns, Rev. Mod. Phys., Vol. 68, No. 2, April 1996.

[6] Cabibbo N. and Parisi G. 1975 Phys.Lett. B 5967.

[7] Tapan Nayak, http://www.bnl.gov/rhic/news/040808/story3.asp

[8] Y. Aoki, G. Endrodi, Z. Fodor, S. D. Katz and K. K. Szabo, Nature 443, 675 (2006).

[9] R. D. Pisarski and F. Wilczck. Phys. Rev. D **29** (1984) 338.

[10] Helmut Satz, arXiv:0903.2778 [hep-ph].

[11] A. Barducci, R. Casalbuoni, S. De Curtis, R. Gatto, G. Pettini, Phys. Lett. B 231 (1989) 463.

[12] M. Stephanov, Phys. Rev. Lett. *76* (1996) 4472.

[13] M. Alford, K. Rajagopal and F. Wilczek, Phys. Lett. B422 (1998) 247.

[14] Rajagopal K and Wilczek F, arXiv:hep-ph/0011333.

[15] M. Cheng et al., Phys. Rev. **D** 79, 074505 (2009); arXiv:0811.1006 [hep-lat].

[16] R.V. Gavai, S. Gupta, Phys. Rev. D 71 (2005) 114014, R. V. Gavai and S. Gupta, Phys. Rev. D 78, 114503 (2008).

[17] M. A. Stephanov, Phys. Rev. Lett. **102**, 032301 (2009).

[18] M. A. Stephanov, K. Rajagopal, and E. V. Shuryak, Phys. Rev. **D** 60, 114028 (1999).

[19] Masayuki Asakawa, Shinji Ejiri, and Masakiyo Kitazawa, Phys. Rev. Lett. **103**, 262301 (2009).

[20] M. A. Stephanov, Phys. Rev. Lett. **107**, 052301 (2011).

[21] M. A. Stephanov, Int.J.Mod.Phys.A20:4387-4392 (2005); arXiv:hep-ph/0402115.

[22] C. Ratti, M.A. Thaler, W. Weise, Phys. Rev. **D** 73 (2006) 014019.

[23] B.-J. Schaefer, J.M. Pawlowski, J. Wambach, Phys. Rev. **D** 76 (2007) 074023.

[24] V. Skokov, B. Friman and, K. Redlich, Phys. Lett. B 708 (2012) 179.

[25] K. Redlich and H. Satz, Phys. Rev. D 33 (1986) 3747.

[26] M. Stephanov, K. Rajagopal and E. Shuryak, Phys. Rev. *D* 60 (1999) 114028.

[27] B. Berdnikov and K. Rajgopal, arXiv:hep-ph/9912274.

[28] J. D. Bjorken, Phys, Rev. **D** 27, (1983).

[29] Frithjof Karsch, Lecture note on "*Lattice QCD at High Temperature and Density*", arXiv:hep-lat/0106019.

[30] J. Adams et al. [for STAR Collaboration], Phys. Rev. Lett. **91**, 072304 (2003).

[31] S. S. Adler et al. [PHENIX Collaboration], Phys. Rev. Lett. **96**, 202301 (2006).

[32] L. Van Hove, Phys. Lett. 118 B, 138 (1982).

[33] C. Alt et al., [NA49 Collaboration], Phys. Rev. **C** 77, 024903 (2008).

[34] J. Adams et al. Nucl. Phys. **A** 757, 102 (2005).

[35] M. Gazdzicki and St. Mrowczynski, Z. Phys. C *54* (1992) 127.

[36] G. L. Melkumov et al., (NA49 Collaboration), Nucl. Phys. B. 219-220 (2011), T. Anticic et al., (NA49 Collaboration), Phys. Rev. C *79* (2009) 044904.

[37] C. Alt et al, (NA49 Collaboration), Phys. Rev. C *78* (2008) 034914.

[38] T. Anticic et al., (NA49 Collaboration), arXiv:1208.5292 [nucl-ex].

[39] B. I. Abelev et al., (STAR Collaboration), Phys. Rev. Lett. **103** (2009) 092301.

[40] T. Anticic et al., (NA49 Collaboration), Phys. Rev. C *83* (2011) 061902.

[41] A. Bazavov, et al., Phys. Rev. Lett. **109**, 192302 (2012) [arXiv:1208.1220 [hep-lat]].

[42] S. Borsanyi, et al., arXiv:1305.5161 [hep-lat].

[43] M. Anderson et al., Nucl. Instrum. Meth. **A** 499 (2003) 659.

[44] K.H. Ackermann et al., Nucl. Instrum. Meth. **A** 499 (2003) 624.

[45] M. Beddo et al., Nucl. Instrum. Meth. **A** 499 (2003) 725.

[46] M. Beddo et al., Nucl. Instrum. Meth. **A** 499 (2003) 740.

[47] L. Adamczyk et al., (STAR Collaboration), Phys. Rev. C **88** (2013) 14902.

[48] W. J. Llope (STAR TOF Group), Nucl. Instrum. Methods Phys. Res., Sect. **B** 241, 306 (2005).

[49] M. Beddo et al., Nucl. Instrum. Meth. **A** 499 (2003) 751.

[50] F.S. Bieser et al., Nucl. Instrum. Meth. **A** 499 (2003) 766.

[51] J.S. Lange et al., Nucl. Instrum. Meth. **A** 453 (2000) 397.

[52] J.M. Landgraf et al., Nucl. Instrum. Meth. **A** 499 (2003) 762.

[53] N. P. Samios and T. W. Ludlam, Nucl. Phys. **A** 498 323 (1989).

[54] G. L. Melkumov et al., (NA49 Collaboration) Nucl. Phys. **B** (Proc. Suppl.) 219-220 (2011).

[55] M. Stephanov, K. Rajagopal and E. Shuryak, Phys. Rev. D **60** (1999) 210.

[56] V. Koch, arXiv:0810.2520 [nucl-th].

[57] K. F. Riley, M.P. Hobson and S.J. Bence, Mathematical Methods for Physics and Engineering, Cambridge university press

[58] F. Karsch and K. Redlich, Phys. Lett. B **695**, (2011).

[59] M. Gyulassy and Wang X N, 1994 Comput. Phys. Commun. 83 307; X. N. Wang and M. Gyulassy, Phys. Rev. D **44**, 3501 (1991).

[60] S. A. Bass et al., Prog. Part. Nucl. Phys. **41** 255 (1998); M. Bleicher et al., J. Phys. G **25** 1859.

[61] A. Kisiel et al., Comput. Phys. Commun. **174**, 669 (2006); M. Chojnacki et al., Comput.Phys.Commun. 183, 746 (2012).

[62] Nihar R. Sahoo, Sudipan De and Tapan K. Nayak, Phys. Rev. C **87**, 044906 (2013); arXiv:1210.7206 [nucl-ex].

[63] Nihar Ranjan Sahoo (for the STAR Collaboration), Acta Phys. Polon. Supp. 6 (2013) 437-444.

[64] P. Braun-Munzinger et al. Nucl. Phys. A **880** 48 (2012).

[65] A. Andronic, P. Braun-Munzinger, and J. Stachel., arXiv:0511071 [nucl-th].

[66] M.M. Aggarwal et al (for the STAR Collaboration), arXiv:1007.2613 [nucl-ex].

[67] J. Cleymans et al, Phys. Rev. **C** 73, 034905 (2006).

[68] http://www.agsrhichome.bnl.gov/RHIC/Runs/

[69] G. Roland's talk *Experimental Overview and Prospects for RHIC*; https://www.bnl.gov/riken/QCDRhic/talks.asp

[70] H. M. Ortmanns, Rev. Mod. Phys. Vol. 68. No.2, April 1996.

[71] Michael L. Miller, Klaus Reygers, Stephen J. Sanders, and Peter Steinberg, Annu. Rev. Nucl. Part. Sci. 2007.57:205-243.

[72] B. I Abelev et al. (STAR Collaboration), Phys. Rev. **C** 79, 034909 (2009).

[73] Michael L. Miller et al. Annu. Rev. Nucl. Part. Sci. 2007. 57:205; arXiv:0701025 [nucl-ex].

[74] http://en.wikipedia.org/wiki/Skewness;
http://en.wikipedia.org/wiki/Kurtosis.

[75] Xiaofeng Luo, J. Phys. G: Nucl. Part. Phys. 39, 025008 (2012).

[76] A. Bzdak and V. Koch, Phys. Rev. **C** 86, 044904 (2012)

[77] Dr. Xiaofeng Luo, *Thesis*, https://drupal.star.bnl.gov/STAR/theses/phd-11

[78] Bradley Efron, *Computers and the Theory of Statistics: Thinking the Unthinkable* ; http://www.jstor.org/stable/2030104

[79] F. Karsch and Swagato Mukherjee; private communication.

Appendix A

Appendix

A.1 Sub-group method of error calculation

The Sub-group method is one of the simplest method for estimating statistical error of a observable. In this method, the whole data sample (called parent sample) is randomly splitted into n number of sub-samples. For example, if there is N of events in a parent sample, then $\frac{N}{n} = x$. Where n is the number of events in each sub-sample and $x = 2, 3, 4, 5....$, represents number of sub-samples. The observables, O, are estimated on each of these sub-samples. Then statistical error of O can be defined as,

$$Var(O) = \frac{\sigma^2}{x-1}. \tag{A.1.1}$$

Here $\sigma^2 =< (O_i - < O >)^2 >$ and $< O >= \frac{1}{x}\sum_{i=0}^{x} O_i$, where $i = 2, 3, 4, 5..x$ number of samples. In this case, $1/(x-1)$ is used to avoid biased estimator on population variance. In the sub-group method, it is good to use large number of sub-groups.

But the disadvantage is that then it is purely dependent on the statistics. Besides this, for higher moments case like 3rd, 4rd... order, this method doesn't work well.

A.2 Analytic method of error calculation

In the analytic error estimation, propagation of error technique is used to get error expression for the mean (M), standard deviation (σ), skewness (S) and kurtosis (κ). The detail calculation can be found in Ref. [77]. The expression used for this analysis are

$$Error(M) = \frac{\sigma}{\sqrt{n}}, \tag{A.2.1}$$

$$Error(\sigma) = \frac{\sigma}{\sqrt{n}}, \tag{A.2.2}$$

$$Error(S) = \frac{3}{\sqrt{n}} \times \sqrt{\kappa + 2 - S^2}, \tag{A.2.3}$$

$$Error(\sigma) = \frac{4}{\sqrt{n}} \times \sqrt{\frac{< (N - < N >)^6}{\sigma^6} - (\kappa + 3)^2 - S^2}. \tag{A.2.4}$$

Above expressions have been derived assuming uncertainty of each event is equal to uncertainty in ensemble of events. Beside this, while deriving these expressions, covariance or correlation between observables are neglected. So, these expressions yield large uncertainty in higher moments as shown in Fig 6.29.

A.3 Bootstrap method of error calculation

In this method, *Monet carlo* technique is used. Some information can be found in Ref [78].

Let's consider a sample $X = (x_1, x_2, x_3, ...x_n)$, where x_i is drawn from a parent distribution. So, for this sample, there can be n^n number of ways to make samples which is known as Bootstrap samples. For example, $N = 2$, $X = (x_1, x_2)$. which can be arranged $2^2 = 4$ number of ways to make Bootstrap samples. Like ${X^*}_1 = (x_1, x_2)$, ${X^*}_2 = (x_1, x_1)$, ${X^*}_3 = (x_2, x_2)$ and ${X^*}_4 = (x_2, x_1)$. Then, the standard deviation of the Bootstrap replications gives the error of the observables.

$$\hat{s}_{err} = \sqrt{\frac{\sum_{b=1}^{B}[s(X_b^*) - s(.)]^2}{B-1}}. \tag{A.3.1}$$

Here $s(.) = \sum_{b=1}^{B} \frac{s({X^*}_b)}{B}$, B represents the number of Bootstrap samples. The typical value of B should be $\geq$200. This method needs huge computational tasks and for large statistics, as in heavy ion collisions experimental events, its processing time is very slow.

List of Publication

1. Beam energy dependence of higher moments of the net-charge multiplicity distributions in Au+Au collisions at RHIC
   Target Journal: Physical Review Letters (Collaboration Review)

2. Baseline study for higher moments of net-charge multiplicity distributions at RHIC energies
   Nihar R. Sahoo, Sudipan De, Tapan K. Nayak
   Phys. Rev. C **87** , 044906 (2013)

3. Higher moments of the net-charge multiplicity distributions at RHIC energies in STAR
   Nihar R. Sahoo (for the STAR Collaboration)
   Acta Phys.Polon. Supp. 6 (2013) 437-444; arXiv:1212.3892 [nucl-ex]

4. Probing the QCD Critical Point by Higher Moments of Net-Charge distribution
   Nihar R. Sahoo (for the STAR Collaboration), Nucl. Phys. A 862-863 (2011) 421-423; arXiv: 1101.5125 [nucl-ex]

5. Charged hadron production in proton-proton collisions at LHC energy
   Santosh K Das, Nihar R. Sahoo, Sudipan De and Tapan Nayak
   Proceedings of the DAE Symp. on Nucl. Phys. 56 (2011)

6. Search for the QCD critical point by the higher moments of the net-charge and net-proton multiplicity distribution in STAR experiment at RHIC
   Nihar R. Sahoo (for the STAR Collaboration)

Proceedings of the DAE Symp. on Nucl. Phys. 56 (2011)

7. Probing the QCD critical point by higher moments of the net-charge and net-proton multiplicity distribution in STAR Experiment
   Nihar R. Sahoo (for the STAR Collaboration), Proceedings of the DAE Symp. on Nucl. Phys. 57 (2012)

8. Energy Dependence of Moments of Net-proton Multiplicity Distributions at RHIC
   STAR Collaboration (L. Adamczyk *et al.*), arXiv:1309.5681v1 [nucl-ex].

9. System Size Dependence of Transverse Momentum Correlation at RHIC
   L. Adamczyk *et. al* (STAR Collaboration), Phys.Rev. C **87** (2013) 064902;

10. Elliptic flow of identified hadrons in Au+Au collisions at $\sqrt{s_{NN}} = 7.7$ to 62.4 GeV
    STAR Collaboration (L. Adamczyk *et al.*), arXiv: 1301.2348 [nucl-ex]

11. Third Harmonic Flow of Charged Particles in Au+Au Collisions at $\sqrt{s_{NN}} =$ 200 GeV
    STAR Collaboration (L. Adamczyk *et al.*), Phys. Rev. C **88** (2013) 014904;

12. Measurement of J/ψ Azimuthal Anisotropy in Au+Au Collisions at $\sqrt{s_{NN}} =$ 200 GeV
    STAR Collaboration (L. Adamczyk *et al.*)

13. J/ψ production at high transverse momenta in p+p and Au+Au collisions at $sqrt(s_{NN}) = 200$ GeV
    STAR Collaboration (L. Adamczyk *et al.*), Phys.Lett. B **722** (2013) 55-62

14. nclusive charged hadron elliptic flow in Au + Au collisions at $\sqrt{s_{NN}} = 7.7 - 39$ GeV

    STAR Collaboration (L. Adamczyk *et al.*), Phys.Rev. C **86** (2012) 054908

15. Energy and system-size dependence of two- and four-particle v_2 measurements in heavy-ion collisions at $\sqrt{s_{NN}} = 62.4$ and 200 GeV and their implications on flow fluctuations and nonflow

    STAR Collaboration (G. Agakishiev *et al.*), Phys.Rev. C **86** (2012) 014904

16. Directed Flow of Identified Particles in Au+Au Collisions at $\sqrt{s_{NN}} = 200$ GeV at RHIC

    STAR Collaboration (L. Adamczyk *et al.*), Phys. Rev. Lett. **108**, (2012) 202301

17. Identified Hadrons Compositions in p+p and Au+Au Collision at High Transverse Momenta at $\sqrt{s_{NN}} = 200$ GeV

    STAR Collaboration (G. Agakishiev *et al.*), Phys. Rev. Lett. **108** (2012) 072302

18. System size and energy dependence of near-side dihadron Correlations

    STAR Collaboration (G. Agakishiev *et al.*), Phys.Rev. C **85**, (2012) 014903

19. Directed and elliptic flow of charged particles in Cu+Cu collisions at $\sqrt{s_{NN}} =$ 22.4 GeV

    STAR Collaboration (G. Agakishiev *et al.*), Phys.Rev. C **85** (2012) 014901

20. ρ^0 Photoproduction in Au+Au collisions at $\sqrt{s_{NN}}$ =62.4 GeV measured with the STAR detector

STAR Collaboration (G. Agakishiev *et al.*), Phys. Rev. C **85** (2012) 014910

21. Strangeness Enhancement in Cu+Cu and Au+Au Collisions at $\sqrt{s_{NN}} = 200$ GeV

    STAR Collaboration (G. Agakishiev *et al.*), Phys. Rev. Lett. **108** (2012) 072301

22. Observation of the antimatter helium-4 nucleus

    Nature bf 473 (2011) 353-356

23. Evolution of the differential transverse momentum correlation function with centrality in Au+Au collisions at $\sqrt{s_{NN}} = 200$ GeV

    STAR Collaboration (H. Agakishiev *et al.*), Phys. Lett. B **704** (2011) 467-473

24. High p_T nonphotonic electron production in p+p collisions at $\sqrt{s_{NN}}$ =200 GeV

    STAR Collaboration (H. Agakishiev *et al.*), Phys. Rev. D **83** (2011) 052006

25. Measurements of Dihadron Correlations Relative to the Event Plane in Au+Au Collisions at $\sqrt{s_{NN}} = 200$ GeV

    STAR Collaboration (H. Agakishiev *et al.*), arXiv: 1010.0690 [nucl-ex]